INFORMATION TO USERS

This manuscript has been reproduced from the microfilm master. UMI films the text directly from the original or copy submitted. Thus, some thesis and dissertation copies are in typewriter face, while others may be from any type of computer printer.

The quality of this reproduction is dependent upon the quality of the copy submitted. Broken or indistinct print, colored or poor quality illustrations and photographs, print bleedthrough, substandard margins, and improper alignment can adversely affect reproduction.

In the unlikely event that the author did not send UMI a complete manuscript and there are missing pages, these will be noted. Also, if unauthorized copyright material had to be removed, a note will indicate the deletion.

Oversize materials (e.g., maps, drawings, charts) are reproduced by sectioning the original, beginning at the upper left-hand corner and continuing from left to right in equal sections with small overlaps. Each original is also photographed in one exposure and is included in reduced form at the back of the book.

Photographs included in the original manuscript have been reproduced xerographically in this copy. Higher quality 6" x 9" black and white photographic prints are available for any photographs or illustrations appearing in this copy for an additional charge. Contact UMI directly to order.

UMI

A Bell & Howell Information Company
300 North Zeeb Road, Ann Arbor MI 48106-1346 USA
313/761-4700 800/521-0600

FIELD SIMULATION AND CALIBRATION IN EXTERNAL ELECTRO-OPTIC SAMPLING

By

XIAOHUA WU, B.Eng., and M.Eng.

(Tsinghua University)

A Thesis

Submitted to the School of Graduate Studies

in Partial Fulfilment of the Requirements

for the Degree

Doctor of Philosophy

McMaster University

July 1996

FIELD SIMULATION AND CALIBRATION IN EXTERNAL ELECTRO-OPTIC SAMPLING

DOCTOR OF PHILOSOPHY (1996) MCMASTER UNIVERSITY
(Electrical and Computer Engineering) Hamilton, Ontario

TITLE: **Field Simulation and Calibration in External Electro-Optic Sampling**

AUTHOR: Xiaohua Wu
B.Eng., and M.Eng.
(Tsinghua University)

SUPERVISOR(S): Dr. David R. Conn
Professor, Chairman of Department of Electrical and Computer Engineering
B.Sc., M.Sc., and Ph.D. (Queen's University)

NUMBER OF PAGES: xvii, 205

Field Simulation and Calibration in External Electro-Optic Sampling

Xiaohua Wu

Abstract

Electro-optic (E-O) sampling is capable of measuring internal node response of microwave and high speed devices and circuits with minimal invasiveness up to terahertz frequency range or in the picosecond domain. Unfortunately, the accuracy of E-O sampling is still not comparable to a conventional network analyzer due to lack of a general calibration technique. Therefore, a general and systematic calibration technique is demanded for quantitative measurement using E-O sampling. In this thesis, a full wave time domain field analysis technique, called the Finite-Difference Time-Domain (FD-TD) method, has been applied to the external E-O sampling problem. Using this theoretical simulation model, field disturbances in external E-O sampling have been investigated, calibration method of external E-O sampling developed and the optimum probing design techniques suggested.

Field disturbances, (*i.e.* invasiveness and distortion) in external E-O sampling have been examined quantitatively, for the first time, by means of field and wave simulation. The results suggest that probes introduce little invasiveness if they are removed from contact by a finite distance which depends on dimensions of the device being tested. The sampled signal distortion introduces considerable error at high frequencies or when sub-picosecond pulses are involved.

The FD-TD method has been successfully applied, for the first time, to external E-O sampling problem and combined with electro-optic tensor to yield

electro-optic response in E-O sampling . The probe transfer function has been then derived to characterize probe specifications. It provides a practical means to quantitatively investigate the operational frequency limit of any given probe.

A field based calibration technique has been developed to de-embed both invasiveness and distortion using the full wave field modeling and the probe transfer function which can be found by field simulation or measurement results. It has been found that each specific probe has an intrinsic transfer function primarily determined by probe dimensions and space between the probe face and the device being tested.

The impact of different probe materials, different sampling beam positions, and different probe dimensions with respect to the device being tested (*i.e.* the electric field orientation) has been systematically evaluated for the first time. The results provide necessary information for engineers to properly design probes and system set-up in order to achieve optimum E-O sampling results.

It has been shown that $LiTaO_3$ probes are favored over GaAs when the sensitivity is the major concern. In contrast, GaAs probes are preferred when the accuracy in high frequencies up to several hundred gigahertz is of primary interest. In addition, sampling near the leading edge of probes is preferred in external E-O sampling to minimize the distortion induced in the measured results.

The research conducted in this thesis can be straightforwardly extended to direct and hybrid E-O sampling problems. Further research and development will lead this field based calibration technique in E-O sampling to more general devices such as microwave monolithic integrated circuits (MMICs).

Acknowledgments

Upon completion of this thesis, I owe my first gratitude to Dr.D.R. Conn, my research and thesis advisor, for the years of valuable research supervision and constant encouragement. With his unique experience in both industry and research, he has given me a unique chance to enhance my professional knowledge and engineering skill. With his insightful teaching methodology, he has given me a beneficial guidance on academic and social matters.

I also wish to thank Dr. Bandler who initially accepted me as Ph.D. candidate in McMaster University and offered me one of the best graduate courses I ever had. I sincerely appreciate Dr.Max Wong's support of my continuing Ph.D. program after ten-month absence due to family tragedy.

I owe special thanks to all my friends in Dr.Conn's research group, whose great help has very much lightened this otherwise tough research in the basement of CRL building. I will remember Mr.Kent Nickerson for his wisdom, Dr.Jian Song for his "optimized" professional support, Mr.Robert Szlavic for his comprehensiveness, Ms.Minya Zhang for her assistance on tele-team work, and Ms.Junmei Zhang for her encouragement.

Thanks to Dr.John Simmons for his insightful suggestions as supervisory committee member and instructive questions as my comprehensive examiner. Thanks to Dr.Chisholm, Dr.Peter Smith and Dr.Carter for their important role in my supervisory and comprehensive committee.

I also wish to thank Dr.John Litva for his cooperative research group and his inspiring course which eventually led me into the field analysis. I owe thanks to

Dr.Z. Bi, Mr.Chen Wu, Dr.Keli Wu, Dr.Yuan Zhuang, Mr.Ji Chen, Dr.Qi YiHong, and Dr.Ying Shen for their enlightening discussions.

Thanks to Dr. John Kuta, Dr. David Walker, Dr. H.M. van Driel at University of Toronto for their creative support. They have contributed their expertise in my research work.

I would also like to thank Mr.Li ZheZhi, the director of the Post-Telecom Industrial Corporation, China and Ms.Yang Lianshi the chief engineer, and all the colleagues I had worked with for three years in the company. My experience there has enabled me to pursue the career in telecommunication industry.

I am especially appreciative of Ms.Juan Li's assistance in her thoughtful editing, thorough and useful proof reading of my thesis over the past year.

Thanks to my son for his understanding and acceptance of the little time I could have enjoyed with him for years due to this Ph.D. program.

Finally but first in time, I would like to express my great appreciation to my parents, and my brother Dr.Xiaolin Wu and his wife for their love, confidence and support of my academic achievements.

Contents

List of Tables xii

List of Figures xvii

1 Introduction 1

1.1 Electro-optic sampling 1

1.2 Field disturbances in external E-O sampling 2

1.3 Field simulation 3

1.4 Electro-optic response 5

1.5 Calibration of external electro-optic sampling 5

1.6 Organization of the thesis 7

2 Electro-Optic Sampling System 9

2.1 Principles of electro-optic sampling 9

2.1.1 Qualitative theory of E-O sampling 9

2.1.2 Quantitative relationships of E-O sampling 12

2.2 Electro-Optic Sampling Systems 25

2.2.1 Sampling geometries 25

2.2.2 System arrangements 27

2.2.3 External E-O sampling 31

2.3 Invasiveness, Distortion and Calibration 35

2.4 Conclusions 36

3 Field and E-O Response Simulation in External E-O Sampling 37

3.1 Introduction 37

3.2 The FD-TD method 41

3.2.1 Discretization 41

3.2.2 The FD-TD algorithm 42

3.2.3 Discontinuities 47

3.2.4 Absorbing boundary conditions 48

3.2.5 Stability and errors 50

3.3 A faster FD-TD algorithm 51

3.3.1 Technique 52

3.3.2 Results 55

3.4 Optical signal calculation 56

3.5 Conclusions 62

4 The invasiveness of external electro-optic sampling 65

4.1 Introduction 65

4.2 Field simulation and optical signal calculation 68

4.2.1 Field simulation parameters 68

4.2.2 Optical signal calculation 74

4.3 Invasiveness 77

4.4 Invasiveness of $LiTaO_3$ and GaAs probes 88

4.5 Equivalent circuit model of the probe 99

4.5.1 Equivalent circuit model 100

4.5.2 Modeling procedure and results 109

4.6 Measurements 117

4.7 Conclusions 118

5 Distortion of external electro-optic sampling 120

5.1 Introduction 120

5.2 Distortion in the external electro-optic sampling 122

5.2.1 Distortion in the time domain 123

5.2.2 Distortion in the frequency domain 125

5.3 Characterization of the probe distortion 136

5.3.1 Dependency on probe thickness 136

5.3.2 Dependency on probe materials 144

5.3.3 Dependency on sampling positions 146

5.4 Conclusions 151

6 Calibration of the External Electro-Optic Sampling 152

6.1 Introduction 152

6.1.1 Optical excitation system 153

6.1.2 Synchronous sampling system 155

6.1.3 Field modeling 156

6.1.4 Recent experimental work 158

6.1.5 Proposed calibration techniques 158

6.2 [S] measurements in the time domain 159

6.2.1 [S] derived from measurements in the time domain 160

6.2.2 Time window method 163

6.3 [S] measurements in the frequency domain 165

6.3.1 Voltage standing wave ratio measurement 166

6.4 Waveform calibration of external E-O sampling 176

6.4.1 Discussion of the probe transfer function 176

6.4.2 Waveform calibration 177

6.5 Calibration of S-parameter measurements 182

6.5.1 Calibration of the reflection coefficient 183

6.5.2 Calibration of the transmission coefficient 187

6.6 Conclusions 191

7 Conclusions **192**

List of Tables

4.1 Parameters in FD-TD analysis 75

4.2 Peak values of the electric field components 81

4.3 Parameters of the electro-optic sampling structure and the equivalent circuit model 114

List of Figures

2.1 Principle of electro-optic sampling 12

2.2 Three sampling geometries for E-O sampling 26

2.3 Schematic of electro-optic sampling system using optical excitation 28

2.4 Schematic for electro-optic sampling system using electrical excitation 30

2.5 Optics schematic of the external E-O sampling 32

3.6 Field-components placement in the FD-TD unit cell, Yee's mesh . . 43

3.7 Fields at a interface between two media 47

3.8 One-dimensional wave at the mesh wall 49

3.9 Moving boundaries in computational domain 54

3.10 Computation time reduction using moving boundaries 57

3.11 Comparison of the transmission coefficients S_{21} 58

3.12 Schematic of the external electro-optic sampling configuration . . . 60

3.13 Cross-sectional view of external electro-optic probe and coplanar waveguide . . . 61

3.14 Magnitudes of the three electric-field components in $LiTaO_3$ probe when a Gaussian pulse launched on the CPW . . . 63

4.15 Schematic of the external electro-optic sampling configuration . . . 70

4.16 Reflected and transmitted signals by field disturbances during probing 72

4.17 Longitudinal component E_x of the electric field on the CPW at the input reference plane . . . 73

4.18 Cross-sectional view of external electro-optic probe and coplanar waveguide . . . 76

4.19 The spatial waveform of E_y 10 μm above the CPW at 9 ps . . . 78

4.20 Conceptual illustration of the field distortion due to the probing . . 82

4.21 Comparison of the electric fields with and without the probe at the position of the probe tip center . . . 83

4.22 Comparison of the field with and without the probe at the position of the probe edge . . . 84

4.23 Comparison of the field on the CPW with and without the probe right under the center of the probe . . . 85

4.24 Comparison of the field on the CPW with and without the probe right under the leading edge of the probe . . . 86

4.25 Magnitude of reflection coefficient S_{11} (dB) of the CPW for different probe distances 90

4.26 Magnitudes of S_{11} (at 55.6 GHz) of the CPW with $LiTaO_3$ and GaAs probes *vs.* probe distance 91

4.27 Transmission coefficient S_{21} of the CPW without probe and with probes in contact 92

4.28 E_z waveforms on the CPW at the output reference plane 94

4.29 Peak value of the normalized optical signal generated in $LiTaO_3$ and GaAs probes *vs.* probe distance 96

4.30 Normalized optical signal *vs.* the magnitude of S_{11} at 55.6 GHz . . 98

4.31 Side view and cross-section of the coplanar waveguide with and without probe. 102

4.32 Equivalent circuit model for the electro-optic sampling structure. . . 103

4.33 Flowchart of the equivalent circuit approach to modeling of the electro-optic probing structure. 111

4.34 S-parameters calculated by the equivalent circuit model and by FD-TD simulation 115

4.35 Calculated magnitude of S11 for different probe to CPW distances . 116

5.36 Waveform comparison of the fields at the position of the probe center with and without the probe 126

5.37 Waveform comparison of the fields at the probe center with and without the fused Silica support 127

5.38 Definition of the system input and output 129

5.39 System transfer function of the probe tip 132

5.40 System transfer function of the CPW 133

5.41 The transfer function of the $LiTaO_3$ probe 135

5.42 Normalized optical signal waveforms for different $LiTaO_3$ probe tip thickness 137

5.43 Magnitude of the system transfer function of the probe tip 139

5.44 Phase of the system transfer functions of the probe tip 141

5.45 Group delay of the system transfer functions of the probe tip 142

5.46 Normalized optical signal intensity *v.s.* the $LiTaO_3$ probe tip thickness 143

5.47 Distortion dependency on probe material at the probe center 145

5.48 Distortion comparison in terms of transfer functions between $LiTaO_3$ and GaAs probes at the probe center 147

5.49 Distortion dependency on sampling positions 149

5.50 Distortion comparison in terms of transfer functions between $LiTaO_3$ and GaAs probes at the probe leading edge 150

6.51 Position of the sampling spots, reference planes and device being tested 160

6.52 A transmission line terminated in a load impedance Z_L 167

6.53 Comparison of a square wave signal propagating on the CPW . . . 179

6.54 Comparison between the electric input obtained by the proposed calibration technique and the actual electric input 181

6.55 Reflected waves combinations 183

6.56 Reference planes defined for Γ or Γ_m and Γ_{prb} 186

6.57 Transmission coefficient combination 189

Chapter 1

Introduction

1.1 Electro-optic sampling

The electro-optic (E-O) sampling measurement technique, based on linear electro-optic effects, was first studied by F. Pockels more than 100 years ago in 1893 [1]. In certain types of crystals, application of an electric field results in a change in polarization of an optical beam which goes through this crystal. This is referred to as the electro-optic effect. E-O sampling employs the E-O effect to measure high speed devices and circuits.

The electric field, that is proportional to the signal measured, induces birefringence in the crystal. Birefringence of a crystal refers to different refractive indices for separate polarization components of the electric field. Polarization of the probing beam is changed when the beam emerges from the crystal due to its birefringence. This change can be detected by a polarization analyzer and photo-detectors. The magnitude of the optical signal produced for a given electric field and probe configuration defines the probe's E-O response. This is the basic

principle of E-O sampling for the measurement of high-speed signals.

In regard to the method of E-O sampling, the measurement system configuration can be cataloged to direct and external sampling. The direct sampling is made from the birefringence of a substrate on which the device being tested is fabricated. The external sampling is conducted from the birefringence of an external probe which is suspended near the device being tested.

External E-O sampling, which is the method considered in this thesis, is attractive for its ability to measure internal node fields of planar circuits, such as MMICs and other ICs, without electro-optic (*e.g.* GaAs) circuit substrates. In addition, sub-picosecond time resolution can be achieved through use of short optical sampling pulses. Therefore, it may be the only measurement technique currently available which possesses the bandwidth of measuring terahertz electrical signal and capability of characterizing internal node response with an extremely low invasiveness.

E-O probes made of $LiTaO_3$ are currently used for external sampling whereas GaAs and AlGaAs probes have just been receiving attention [2, 3, 4]. These materials, however, are usually high dielectrics. Consequently, the field inside the probe and the device being tested as well as the field in their vicinity are disturbed.

1.2 Field disturbances in external E-O sampling

The problem of field disturbances in external E-O sampling was raised several years ago [5, 6]. However little work has been devoted to it because there are no comprehensive modeling and systematic analysis of the problem, which requires

detailed field modeling and analysis of the interaction between the electric field and sampling optical beam in the electro-optic probe.

There are two types of field disturbances in external E-O sampling. One is the probing **invasiveness** to operation of the device being tested, which is caused by the high dielectric material of the external probe. The other is the measured signal **distortion** in the electro-optic probe, which is determined primarily by the probe materials and dimensions.

Frankel *et al* experimentally investigated field disturbances in sub-picosecond signal measurement and created a circuit model to approximately describe the disturbance problems [7, 8]. To further their research, this thesis has successfully applied a full wave time domain field analysis technique to the external E-O sampling problem [9], whereby both probing invasiveness [10] and signal distortion [11, 12] have been quantitatively studied for the first time in a theoretical way.

1.3 Field simulation

In order to comprehensively understand the insight of field disturbances in external E-O sampling, a full wave field simulation is desirable. The full wave time domain field analysis technique, called the Finite-Difference Time-Domain (FD-TD) method [13], is chosen according to following reasons.

1. The FD-TD method, as a **time domain** field modeling technique, is most suitable for E-O sampling system analysis since high-speed pulse propagation and its response are measured in time domain using E-O sampling system as opposed to analysis and measurement using narrow band high Q system.

2. E-O sampling measures high-speed signals, and hence its modeling requires transient responses which can be systematically studied by full wave analysis. The FD-TD method makes it possible to conduct this analysis efficiently.

3. A complex three dimensional structure is involved in E-O sampling. The FD-TD method is particularly efficient for handling three dimensional discontinuities.

4. To investigate the E-O response as the sampled output signal in E-O sampling, a temporal field information along the probing beam path is required for calculation of optical signals. The FD-TD method automatically offers this information.

5. Frequency domain information over the entire range of interest, such as S-parameters, may be obtained by a Fourier transform of the response to a board-band pulse.

Hence, the FD-TD method is well suited to the external E-O sampling problem. It is used to simulate the full wave time domain field around a coplanar waveguide on a GaAs substrate in an external E-O sampling configuration. The results make it possible for the first time to theoretically characterize the external probe specifications and to quantitatively evaluate the probing invasiveness in external E-O sampling measured by scattering parameters and the signal distortion described by a probe transfer function.

1.4 Electro-optic response

The electro-optic response was previously calculated by assuming a uniform field or voltage distribution in the electro-optic medium which is the probe tip in external E-O sampling. However, the full wave analysis shows that the actual signal field in the probe tip is significantly different from the uniform distribution, especially in the picosecond range or at high frequencies. Hence, the E-O response calculation has been made by incorporating results of the full wave time domain field simulation with the electro-optic tensor of the probe material. Furthermore, the effects attributed to the time period taken by the probing beam to go through the probe have been considered in the calculation.

The E-O response calculation technique introduced in this thesis also provides an efficient way to analyze the effects of probe misalignment in relation to the measured device or the tested field. This technique coupling with Jones matrices of the external E-O sampling optics may suggest a practical method of probe misalignment calibration, which may otherwise require a prohibitively expensive super precise probe positioner [1, 14].

1.5 Calibration of external electro-optic sampling

Research on a calibration technique for external E-O sampling has received little attention until the recent work of this thesis in the field modeling of the probing configuration [9, 10, 11, 12, 15]. Consequently, most E-O sampling measurements

have been done only in relative terms [5, 16, 17].

A reference calibration technique has been previously used to find the absolute magnitude of sampled signals [18], where a known signal is applied to the device being tested through a transmission line to define a standard measurement [16]. This technique implicitly assumes a perfect probe alignment in many different measurements and a frequency independent response of the probe regardless of the device being tested. The actual situations, however, are different from these assumptions. The difference will be illustrated by the analysis presented in this thesis.

A field based calibration technique to relate the field in the device being tested to the resultant sampling output signal is developed for the first time in this thesis. It makes it possible to de-embed both the probing invasiveness and the signal distortion. When the probe is not in contact with the device being tested, a simple treatment may be accurate enough while the associated error can be estimated using the principle in this calibration technique.

As a summary, the field based calibration technique can perform:

1. **Waveform measurement calibration.** It is specially designed for the subpicosecond waveform measurement where the probe exhibits severe distortion to the measured signal.

2. **Vector measurement calibration.** It is particularly useful for quantitative characterization of devices or circuits, for example, S-parameter measurements.

1.6 Organization of the thesis

As a brief introduction, Chapter 1 presents outline of this thesis which is devoted to the research on field modeling and calibration of external electro-optic sampling. At the beginning of each following chapter, a review is given on a specific topic including its previous research, current status and the problems to be studied in the chapter. The review is followed by a description of the techniques used in each chapter and the results as well as discussions.

Chapter 2 explains the principle of E-O sampling. An overview is given on the systems distinguished into direct, external and hybrid sampling configurations by their respective sampling geometries. Two different modes in E-O sampling are also described where the device being tested is driven by an electrical sinusoidal signal in one mode and by a short pulse signal in the other. Formulas are also derived in this chapter to relate the sampled field to resultant sampling retardance.

Chapter 3 is devoted to the field simulation technique and results. A faster FD-TD algorithm is proposed by using moving boundary conditions and presented with a computation example [19, 20]. The technique and typical results of the E-O response calculation using electro-optic tensor and the field simulation results are provided in this chapter as well.

Chapter 4 discusses the probing invasiveness whereas Chapter 5 deals with the distortion. Yet both apply the field simulation technique and E-O response calculation results to the derivation of a transfer function, which is then used for the waveform calibration.

Chapter 6 presents calibration techniques to de-embed the probing invasiveness and the signal distortion. One technique is for temporal waveform measurement and the other for vector measurement such as S-parameters. A detailed procedure is proposed for S-parameters measurements. In addition, the error analysis is also reported.

Finally Chapter 7 completes the thesis with conclusions and recommendations for further research on the calibration of the E-O sampling.

Chapter 2

Electro-Optic Sampling System

2.1 Principles of electro-optic sampling

In certain types of crystals, application of an electric field results in a change in polarization of an optical beam which goes through this crystal. This is referred to as the electro-optic (E-O) effect. E-O sampling employs the E-O effect to measure high speed devices and circuits. It demonstrates three major advantages: high speed, low invasiveness and capability of measuring internal node response of integrated circuits [21, 22].

2.1.1 Qualitative theory of E-O sampling

To establish the basic principle of E-O sampling, the definition of electric field polarization and the crystal birefringence are reviewed as follows.

Polarization of a plane wave refers to the orientation of electric field vector, which may be in a fixed direction, or may change with time [23]. In a transverse wave, the electric field is perpendicular to the direction of the wave propagation. For example, if the wave is traveling in the z-direction, the electric field may be in the x-direction, in the y-direction, or in any other direction within the x-y plane. If the electric field of the light wave is parallel to the x-axis, the light is linearly polarized in the x-direction.

Suppose the wave is linearly polarized in one direction within the x-y plane. It can be considered as summation of two in-phase waves. One is linearly polarized in the x-direction and the other in the y-direction.

The circularly polarized wave or any other polarized wave within x-y plane can be thought as the superposition of two linearly polarized waves in x-direction and in y-direction with a specific relative difference in phase.

Unpolarized light is polarized in different directions (but perpendicular to the direction of propagation) randomly and rapidly. In other words, the direction of the electric field varies rapidly and randomly, which has no preferred direction.

Refraction is referred to as the bending of a transmitted beam at the interface between two media. The key idea in the refraction is that light travels more slowly in a dense medium than in a less dense medium. Hence, different wave velocities in different media account for the refraction. The medium's **refractive index** n is defined by

$$n = \frac{c}{v} \tag{2.1}$$

where v and c are respectively the speed of light in some material and that in vacuum.

Birefringence (or double refracting) of a crystal refers to the different refractive indices for different polarization components of the electric field, one for polarization along and one for polarization perpendicular to the optic axis of the crystal.

Many crystals, *e.g.* $LiTaO_3$ and GaAs, can affect the polarization of incident light without absorbing or reflecting one of the components. This is because their structures are sufficiently asymmetric that the speed of light in these crystals is different for one polarization component than it is for the perpendicular component. Such substances are called birefringent or double refracting. Referring to (2.1), v is a direction dependent parameter in birefringent crystals.

Figure 2.1 shows the basic principle of electro-optic sampling. A circular polarized optical probing beam is directed through a piece of birefringent crystal where an electric field is imposed. The electric field, that is proportional to the signal measured, induces birefringence in the crystal. Polarization of the probing beam is changed to an ellipsoidal polarized beam typically when the beam comes out of the crystal due to birefringence. This change can be detected by an optical polarization analyzer to produce an *optical signal*, which is converted to an electrical measurement by photo-detectors. The magnitude of the optical signal produced for a given electric field and probing configuration defines E-O *response* of the probe. This is the basic principle of E-O sampling in the measurement of the electric field, voltage or signal response.

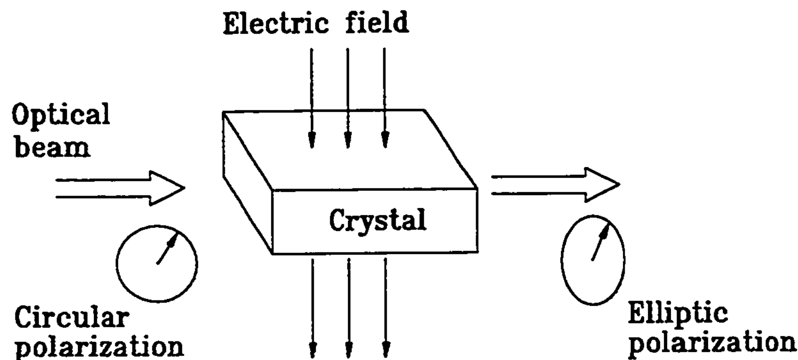

Figure 2.1: Principle of electro-optic sampling. Polarization of the probing beam is changed after its passing through the crystal due to the crystal birefringence which is related to the applied electric field.

There are always two ordinary axes and one extraordinary axis in uniaxial crystals (*i.e.*, a crystal with a single axis of threefold, fourfold, or sixfold symmetry). The c axis is defined as the direction of this single axis in relation to which the crystal symmetry is established. By a strict convention this single axis is taken as z axis. The extraordinary axis is thus the z axis or the c axis.

The birefringent crystals may be either uniaxial ($n_x = n_y \neq n_z$) or biaxial ($n_x \neq n_y \neq n_z$). $LiTaO_3$, GaAs and other commonly used electro-optic crystals are uniaxial.

2.1.2 Quantitative relationships of E-O sampling

In homogeneous materials

$$v_g = \frac{c}{\sqrt{\epsilon_r}} \tag{2.2}$$

where v_g is the speed of light in the material, ϵ_r is the relative dielectric constant of the material and ϵ is the dielectric constant of the material. Since the index of refraction n and the relative dielectric constant are defined as

$$n = \frac{c}{v_g} \tag{2.3}$$

$$\epsilon_r = \frac{\epsilon}{\epsilon_0} \tag{2.4}$$

from (2.2)-(2.4),

$$\frac{\epsilon_0}{\epsilon} = \frac{1}{n^2} \tag{2.5}$$

In an anisotropic crystal, polarization induced by an electric field and the field itself are not necessarily parallel. The electric displacement vector **D** and the electric field **E** are consequently related by means of the dielectric tensor ϵ_{ij} defined by [1]

$$D_k = \epsilon_{ij} E_l \tag{2.6}$$

where $i, j, l, k = x, y, z$.

In matrix form, (2.6) can be expressed as

$$\begin{bmatrix} D_1 \\ D_2 \\ D_3 \end{bmatrix} = \begin{bmatrix} \epsilon_{11} & \epsilon_{12} & \epsilon_{13} \\ \epsilon_{21} & \epsilon_{22} & \epsilon_{33} \\ \epsilon_{31} & \epsilon_{32} & \epsilon_{33} \end{bmatrix} \begin{bmatrix} E_1 \\ E_2 \\ E_3 \end{bmatrix} \tag{2.7}$$

The 3×3 matrix with elements ϵ_{ij} in (2.7) is called the dielectric tensor.

Similar to (2.5), in asymmetric material

$$\frac{\epsilon_0}{\epsilon_{ij}} = \frac{1}{n_{ij}^2} \tag{2.8}$$

where ϵ_{ij} is an element of the dielectric tensor for the crystal, ϵ_0 is the permittivity of vacuum and n_{ij} is an element of the refraction index tensor of the crystal.

In matrix form, (2.8) can be expressed as

$$\begin{bmatrix} \frac{\epsilon_0}{\epsilon_{11}} & \frac{\epsilon_0}{\epsilon_{12}} & \frac{\epsilon_0}{\epsilon_{13}} \\ \frac{\epsilon_0}{\epsilon_{21}} & \frac{\epsilon_0}{\epsilon_{22}} & \frac{\epsilon_0}{\epsilon_{23}} \\ \frac{\epsilon_0}{\epsilon_{31}} & \frac{\epsilon_0}{\epsilon_{32}} & \frac{\epsilon_0}{\epsilon_{33}} \end{bmatrix} = \begin{bmatrix} \frac{1}{n_{11}^2} & \frac{1}{n_{12}^2} & \frac{1}{n_{13}^2} \\ \frac{1}{n_{21}^2} & \frac{1}{n_{22}^2} & \frac{1}{n_{23}^2} \\ \frac{1}{n_{31}^2} & \frac{1}{n_{32}^2} & \frac{1}{n_{33}^2} \end{bmatrix} \tag{2.9}$$

The 3×3 matrix with elements n_{ij} is called the refraction index tensor of the crystal.

It is shown from symmetry considerations that the refraction index tensor of the crystal is a symmetrical matrix. Therefore a new set of notation is introduced to the elements in (2.9) as follows

$$\left(\frac{1}{n^2}\right)_1 = \frac{1}{n_{11}^2} \tag{2.10}$$

$$\left(\frac{1}{n^2}\right)_2 = \frac{1}{n_{22}^2} \tag{2.11}$$

$$\left(\frac{1}{n^2}\right)_3 = \frac{1}{n_{33}^2} \tag{2.12}$$

$$\left(\frac{1}{n^2}\right)_4 = \frac{1}{n_{23}^2} = \frac{1}{n_{32}^2} \tag{2.13}$$

$$\left(\frac{1}{n^2}\right)_5 = \frac{1}{n_{13}^2} = \frac{1}{n_{31}^2} \tag{2.14}$$

$$\left(\frac{1}{n^2}\right)_6 = \frac{1}{n_{12}^2} = \frac{1}{n_{21}^2} \tag{2.15}$$

A comparison between (2.8) and (2.5) indicates an analogy between them. In homogeneous material, ϵ and n are constants in any direction. However, in crystal material, both ϵ and n are direction dependent as shown in (2.8).

As it is known, given a propagation direction of a light beam in a crystal, there exist two possible linearly polarized modes which are called rays of propagation. Each mode possesses a unique direction of polarization (*i.e.*, direction of **D**) and a corresponding index of refraction (*i.e.*, a velocity of propagation). The mutually orthogonal polarization directions and the indices of the two rays are found most easily by using the index ellipsoid

$$\frac{x^2}{n_x^2} + \frac{y^2}{n_y^2} + \frac{z^2}{n_z^2} = 1 \tag{2.16}$$

where the directions x, y and z are the principal dielectric axes. **D** and **E** are parallel along directions of the principal axes of the index ellipsoid.

The propagation characteristics of a light beam in birefringent crystals are fully described by means of the index ellipsoid (2.16). Hence, the effect of an electric field on the light wave propagation is expressed most conveniently by giving the change in the index ellipsoid constants in (2.16).

In the presence of an electric field, the equation of the index ellipsoid (2.16) is changed to

$$\left(\frac{1}{n^2}\right)_1 x^2 + \left(\frac{1}{n^2}\right)_2 y^2 + \left(\frac{1}{n^2}\right)_3 z^2 + 2\left(\frac{1}{n^2}\right)_4 yz + 2\left(\frac{1}{n^2}\right)_5 xz + 2\left(\frac{1}{n^2}\right)_6 xy = 1 \quad (2.17)$$

or simplified as

$$\left(\frac{1}{n^2}\right)_i x_k x_l = 1 \quad (2.18)$$

where $i = 1 \sim 6, k, l = 1 \sim 3$. k and l are one of x, y and z. Note that the new principal axes of the ellipsoid associated with the applied electric field in (2.17) or (2.18) are not necessarily the x,y and z axes.

In matrix form, (2.17) or (2.18) can also be expressed as

$$\begin{bmatrix} x \\ y \\ z \end{bmatrix}' \begin{bmatrix} \frac{1}{n_{11}^2} & \frac{1}{n_{12}^2} & \frac{1}{n_{13}^2} \\ \frac{1}{n_{21}^2} & \frac{1}{n_{22}^2} & \frac{1}{n_{23}^2} \\ \frac{1}{n_{31}^2} & \frac{1}{n_{32}^2} & \frac{1}{n_{33}^2} \end{bmatrix} \begin{bmatrix} x \\ y \\ z \end{bmatrix} = 1 \quad (2.19)$$

or using the symmetry relations (2.10)-(2.15),

$$\begin{bmatrix} x \\ y \\ z \end{bmatrix}' \begin{bmatrix} \left(\frac{1}{n^2}\right)_1 & \left(\frac{1}{n^2}\right)_6 & \left(\frac{1}{n^2}\right)_5 \\ \left(\frac{1}{n^2}\right)_6 & \left(\frac{1}{n^2}\right)_2 & \left(\frac{1}{n^2}\right)_4 \\ \left(\frac{1}{n^2}\right)_5 & \left(\frac{1}{n^2}\right)_4 & \left(\frac{1}{n^2}\right)_3 \end{bmatrix} \begin{bmatrix} x \\ y \\ z \end{bmatrix} = 1 \tag{2.20}$$

If x, y and z are chosen to be parallel to the principal dielectric axes of the crystal, then with zero applied field, (2.17) must reduce to (2.16). Therefore,

$$\begin{aligned} \left.\left(\frac{1}{n^2}\right)_1\right|_{E=0} &= \frac{1}{n_x^2} \\ \left.\left(\frac{1}{n^2}\right)_2\right|_{E=0} &= \frac{1}{n_y^2} \\ \left.\left(\frac{1}{n^2}\right)_3\right|_{E=0} &= \frac{1}{n_z^2} \\ \left.\left(\frac{1}{n^2}\right)_4\right|_{E=0} &= \left.\left(\frac{1}{n^2}\right)_5\right|_{E=0} = \left.\left(\frac{1}{n^2}\right)_6\right|_{E=0} = 0 \end{aligned}$$

A linear change in the coefficients $\left(\frac{1}{n^2}\right)_i$ $(i = 1, 2, ..., 6)$ due to an electric field $\mathbf{E}$ is defined by

$$\Delta\left(\frac{1}{n^2}\right)_i = \sum_{j=1}^{3} \mathbf{r}_{ij} E_j \tag{2.21}$$

where in the summation over j, the convention rule of $1 = x$, $2 = y$ and $3 = z$ is used.

$\mathbf{r}_{ij}$ linearly relates E_j applied on a crystal to the resultant change in the

coefficients $\left(\frac{1}{n^2}\right)_i$ in (2.17). This relation is called E-O effect or Pockels effect after his first studies in 1893 [1].

Equation (2.21) can be expressed in a matrix form as

$$\begin{bmatrix} \Delta\left(\frac{1}{n^2}\right)_1 \\ \Delta\left(\frac{1}{n^2}\right)_2 \\ \Delta\left(\frac{1}{n^2}\right)_3 \\ \Delta\left(\frac{1}{n^2}\right)_4 \\ \Delta\left(\frac{1}{n^2}\right)_5 \\ \Delta\left(\frac{1}{n^2}\right)_6 \end{bmatrix} = \begin{bmatrix} \mathbf{r}_{11} & \mathbf{r}_{12} & \mathbf{r}_{13} \\ \mathbf{r}_{21} & \mathbf{r}_{22} & \mathbf{r}_{23} \\ \mathbf{r}_{31} & \mathbf{r}_{32} & \mathbf{r}_{33} \\ \mathbf{r}_{41} & \mathbf{r}_{42} & \mathbf{r}_{43} \\ \mathbf{r}_{51} & \mathbf{r}_{52} & \mathbf{r}_{53} \\ \mathbf{r}_{61} & \mathbf{r}_{62} & \mathbf{r}_{63} \end{bmatrix} \begin{bmatrix} E_1 \\ E_2 \\ E_3 \end{bmatrix} \tag{2.22}$$

The 6×3 matrix with elements $\mathbf{r}_{ij}$ in (2.21) is called electro-optic tensor. It relates the applied field $\mathbf{E}$ to the change in

$$\left(\frac{1}{n^2}\right)_i \qquad \text{i=1,2,...6} \tag{2.23}$$

Therefore,

$$\begin{aligned} \left(\frac{1}{n^2}\right)_i &= \left(\frac{1}{n^2}\right)_i\bigg|_{E=0} + \Delta\left(\frac{1}{n^2}\right)_i \\ &= \left(\frac{1}{n^2}\right)_i\bigg|_{E=0} + \sum_{j=1}^{3} \mathbf{r}_{ij} E_j \end{aligned} \tag{2.24}$$

Applying (2.24) to (2.17) gives

$$\left[\frac{1}{n_1^2} + r_{1k}E_k\right] x^2 + \left[\frac{1}{n_2^2} + r_{2k}E_k\right] y^2 + \left[\frac{1}{n_3^2} + r_{3k}E_k\right] z^2 + 2r_{4k}yzE_k + 2r_{5k}xzE_k + 2r_{6k}xyE_k = 1 \tag{2.25}$$

where k=1,2,3 corresponding to x, y and z respectively in rectangular coordinate system.

It is seen from (2.25) that the index ellipsoid can be fully determined by the coefficients $\left(\frac{1}{n^2}\right)_i$. In the presence of an electric field, the new direction and magnitude of new principal axes can be found by finding three eigenvalues of the following matrix

$$\begin{bmatrix} \frac{1}{n_{11}^2} & \frac{1}{n_{12}^2} & \frac{1}{n_{13}^2} \\ \frac{1}{n_{21}^2} & \frac{1}{n_{22}^2} & \frac{1}{n_{23}^2} \\ \frac{1}{n_{31}^2} & \frac{1}{n_{32}^2} & \frac{1}{n_{33}^2} \end{bmatrix} \tag{2.26}$$

or

$$\begin{bmatrix} \left(\frac{1}{n^2}\right)_1 & \left(\frac{1}{n^2}\right)_6 & \left(\frac{1}{n^2}\right)_5 \\ \left(\frac{1}{n^2}\right)_6 & \left(\frac{1}{n^2}\right)_2 & \left(\frac{1}{n^2}\right)_4 \\ \left(\frac{1}{n^2}\right)_5 & \left(\frac{1}{n^2}\right)_4 & \left(\frac{1}{n^2}\right)_3 \end{bmatrix} \tag{2.27}$$

where the symmetry relations expressed by (2.10)-(2.15) are used in the derivation.

The three eigenvalues correspond to the new values of

$$\left(\frac{1}{n^2}\right)_{x'}$$
$$\left(\frac{1}{n^2}\right)_{y'}$$
$$\left(\frac{1}{n^2}\right)_{z'}$$

which determine the new directions of principal axes of the index ellipsoid. Propagation velocities of the linearly polarized wave along the new principal axes are also expressed by

$$v_x = \frac{c}{n_{x'}} \tag{2.28}$$
$$v_y = \frac{c}{n_{y'}} \tag{2.29}$$
$$v_z = \frac{c}{n_{z'}} \tag{2.30}$$

These results can be derived using (2.3) in anisotropic crystals.

Refraction at a crystal face depends on the direction of incidence, the polarization, and the orientation of the optic axis of the crystal. Light traveling through a birefringent crystal in a direction neither parallel nor perpendicular to the optic axis is broken into two rays of perpendicular polarization components: the **ordinary ray** and the **extraordinary ray**.

In uniaxial crystals, *i.e.,* crystals in which the highest degree of rotational

symmetry is applied to no more than a single axis, the index ellipsoid (2.16) simplifies to

$$\frac{x^2}{n_o^2} + \frac{y^2}{n_o^2} + \frac{z^2}{n_e^2} = 1 \tag{2.31}$$

where the axis of symmetry, referred to be the optic axis, is chosen as the z axis following the convention. n_o is called the ordinary index of refraction, whereas n_e is the extraordinary one. Both indices are functions of the electric field applied or corresponding to the eigenvalues of (2.27).

Two forms of the electro-optic tensors for the most often used crystal symmetries are given as follows: (2.32) for cubic $\bar{4}3m$ (*e.g.* GaAs and InP) and (2.33) for trigonal $3m$ (*e.g.* $LiNbO_3$ and $LiTaO_3$).

$$[r] = \begin{bmatrix} 0 & 0 & 0 \\ 0 & 0 & 0 \\ 0 & 0 & 0 \\ r_{41} & 0 & 0 \\ 0 & r_{41} & 0 \\ 0 & 0 & r_{41} \end{bmatrix} \tag{2.32}$$

and

$$[r] = \begin{bmatrix} 0 & -r_{22} & r_{13} \\ 0 & r_{22} & r_{13} \\ 0 & 0 & r_{33} \\ 0 & r_{51} & 0 \\ r_{51} & 0 & 0 \\ -r_{22} & 0 & 0 \end{bmatrix} \tag{2.33}$$

the electro-optic tensor for other materials is also a 6×3 matrix, but with different element values.

If the electric field component E_z is imposed on a GaAs crystal while E_x and E_y are negligible, then

$$\frac{x^2}{n_1^2} + \frac{y^2}{n_2^2} + \frac{z^2}{n_3^2} + 2r_{41}xyE_z = 1 \tag{2.34}$$

The last term on the left-hand side of (2.34) mixes the x and y axes. The new principal axes for the index ellipsoid are x' and y', and z, where

$$\hat{\mathbf{x}}' = \frac{1}{\sqrt{2}}(\hat{\mathbf{x}} + \hat{\mathbf{y}}) \tag{2.35}$$

$$\hat{\mathbf{y}}' = \frac{1}{\sqrt{2}}(-\hat{\mathbf{x}} + \hat{\mathbf{y}}) \tag{2.36}$$

the index ellipsoid defined by (2.34) becomes

$$\left[\frac{1}{n^2} + r_{41}E_z\right] x'^2 + \left[\frac{1}{n^2} - r_{41}E_z\right] y'^2 + \frac{1}{n^2}z'^2 = 1 \tag{2.37}$$

Assuming $r_{41}E_z \ll n_2$ and using the relation

$$(1 \pm x)^{-n} = 1 \mp nx \qquad \text{if x} \ll 1 \tag{2.38}$$

Hence, the indices of refraction along the new principal axes are

$$n_{x'} = n - \frac{1}{2}n^3 r_{41} E_z \tag{2.39}$$

$$n_{y'} = n + \frac{1}{2}n^3 r_{41} E_z \tag{2.40}$$

$$n_z = n \tag{2.41}$$

Thus, the crystal becomes birefringent due to the electric field along $\hat{\mathbf{z}}$ which creates new principal axes x' and y' in the $x - y$ plane. (2.34) is then modified as

$$\frac{x'}{n_{x'}^2} + \frac{y'}{n_{y'}^2} + \frac{z'}{n_{z'}^2} = 1 \tag{2.42}$$

For a distance of L, the electric or optical length $\Delta\varphi$ is

$$\begin{aligned} \Delta\varphi &= \beta L \\ &= \frac{2\pi}{\lambda_g} L \end{aligned}$$

$$= \frac{2\pi}{\lambda_0}\sqrt{\epsilon_r}L$$
$$= \frac{2\pi}{\lambda_0}nL \qquad (2.43)$$

The refraction index is usually used to calculate the optical length.

It is implied from (2.43) that GaAs crystal becomes birefringent when an electric field is applied. It functions as a modulator based on the electro-optic effect in which the electric field is the signal that modulates the optical beam passing through it. The relative change in phase, not the absolute change, accumulated by the y' and x' components of the input optical probing beam is the *retardance* $\mathbf{\Gamma}$, given by

$$\Gamma = \frac{2\pi(n_{y'} - n_{x'})L}{\lambda} \qquad (2.44)$$

The retardance Γ is caused by different velocities or different indices of refraction along y' and x' directions. Then, polarization of the probing beam is changed due to the retardance, typically from circular polarization to ellipsoid polarization in E-O sampling. Applying (2.39) and (2.40) to (2.44), a relation between the signal field and the retardance of the optical beam can be found. This is the basic E-O sampling principle.

Conceptual understanding of the retardance used in E-O sampling has been explained in a simple case of GaAs crystal where only one component of the electric field is considered. On the contrary, in a general case where E_x and E_y are not

negligible, the retardance Γ should be determined by indices of refraction along the new principal axes. However the explicit formula in closed form may not be available mainly because the field information in three dimensions is required. Full wave field modeling is desired in order to quantitatively determine the retardance Γ caused by a given electric field.

2.2 Electro-Optic Sampling Systems

2.2.1 Sampling geometries

Three basic variations of E-O sampling may be defined as direct, external and hybrid sampling respectively. Referring to Figure 2.2, they are associated with the individual placement of the device being tested relative to the E-O medium in which the E-O effect is observed. In direct E-O sampling, the device is fabricated on a substrate that is itself electro-optic, and the probe beam senses the fields or voltages in the device via the E-O effects in the substrate. The probe beam in the direct probing can approach the substrate either from front-side or back-side of the device. For external and hybrid sampling, the device may not be fabricated on an E-O substrate, so measurements can be performed on devices fabricated on silicon, as well as GaAs and InP substrates. In external sampling, a crystal of an electro-optic material, such as $LiTaO_3$ or GaAs, is placed above the device, so that the electric fields from the device penetrate into the sampling crystal. In hybrid sampling, a discrete sampler, which is usually composed of a microwave

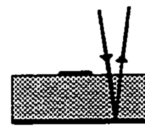

(a) Direct probing

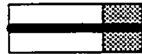

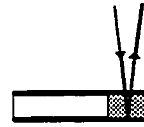

(b) Hybrid probing

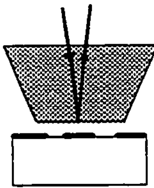

(c) External probing

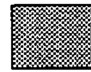

Figure 2.2: Three sampling geometries for E-O sampling. The electro-optic crystal respectively refers to the substrate of the device being tested for direct probing, a crystal on a separate test structure for hybrid probing, and a separate crystal probe placed above the device for external probing.

transmission line deposited on an E-O material, is electrically connected to the device being tested, so that voltage waveforms produced in the device are coupled into the sampler [24, 25, 26, 27]. In both external and hybrid sampling systems, the probe beam does not propagate through the device, but rather through the sampling crystal.

2.2.2 System arrangements

Electro-optic sampling can also be grouped into two arrangements in terms of the driving signal of the device being tested. One is electrical excitation and the other is optical excitation. Electrical excitation is also called synchronous sampling, corresponding to frequency domain measurement since only the response at one frequency is detected in one measurement. Optical excitation is made fully in time domain because a short pulse response rather than a single sinusoidal wave response is measured. In one measurement, optical excitation covers a wide range of the frequency band which is determined by pulse width of the excitation signal. However, the temporal waveform is detected directly in the measurement for arrangements of both electrical and optical excitations.

E-O sampling using optical pulse excitation

In E-O sampling systems using optical excitation as shown in Figure 2.3, pulses from a mode-locked laser are divided into two beams. One beam illuminates the

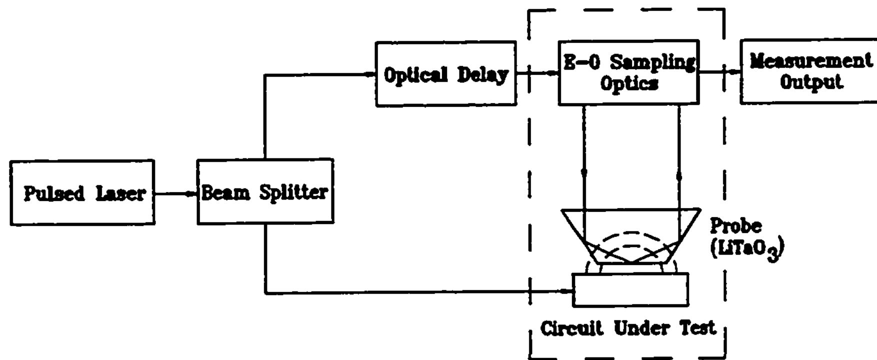

Figure 2.3: Schematic of electro-optic sampling system using optical excitation to generate an electric driving signal for the device being tested.

photo detector connected with the device being tested to generate an electrical signal pulse. The other is the probing beam which is circularly polarized by a quarter-wave plate. The probing beam is directed through an electro-optic crystal, whose refraction indices are changed due to birefringence. The change is linearly related to an electric field penetrating through the crystal, which is generated and proportional to the signal on the device. Thus, polarization of the beam passing through the crystal depends on the electric field in the crystal. This crystal respectively refers to the substrate of the device being tested for the direct probing, a separate probe placed above the device for the external probing and a separate test structure or circuit for the hybrid probing. A polarizing beam-splitter is used to set apart orthogonal and horizontal polarizations for differential detection of the change in polarization by photo diodes. The excitation beam is modulated to improve the signal to noise ratio [28]. The temporal waveform is reconstructed by changing the optical delay between the signal pulse traveling on the device and

the probing beam passing through the probe. A mechanical delay line may serve for this purpose.

E-O sampling using electrical sinusoidal excitation

The E-O sampling system using electrical sinusoidal excitation is shown in Figure 2.4 [29]. An optical probing pulse with a repetition rate f_0 (set by the laser) samples a repetitive voltage waveform. If the waveform repeats at exactly $\mathbf{N}f_0$ which is an integer multiple of the probe repetition rate, the probing pulse will interact with the waveform every **N**th period at a fixed point within its cycle. Over many repetitions, the pulses sample the waveform at the same time within the cycle, undergoing an equal modulation of the intensity of each pulse in the sampling crystal. The resultant change in the average intensity of the probing beam, proportional to the signal, is detected by a photo diode receiver whose bandwidth is much less than the optical pulse repetition frequency.

For tracing the entire time waveform, probing beam pulses must be timed in a continuously varying fashion to cover the relevant time frame. In order to do so, the frequency of the signal applied to the device being tested is increased by a small amount Δf. The probing beam pulses are then slowly delayed with respect to the waveform, sampling successively delayed points. As a result, the average intensity at the photo diode changes in proportion to the waveform. The process of slowly delaying the probing beam pulses repeats at a rate Δf. Δf can be very low,

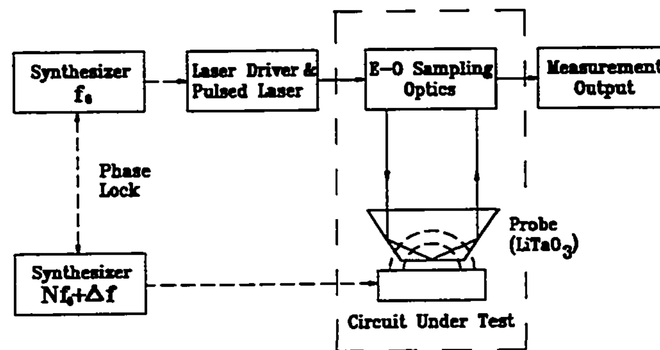

Figure 2.4: Schematic for electro-optic sampling using using electrical excitation to drive the device being tested.

leading to an application of the low cost and low speed instruments for detection of the sampled signal. If the signal to the device being tested is periodic, the sampling process can be made over an arbitrarily large number of cycles, reducing the random noise effects. To accurately acquire the entire waveform, the time window in sampling should be precisely controlled to be exactly an integer multiple of the period of optical probing beam pulse train.

An E-O sampling system using electrical sinusoidal excitation is also called *synchronous sampling*. It measures the device response at the frequency of driving signal $Nf_0 + \Delta f$. The frequency domain description of this system is known as harmonic mixing. In this system, differences in frequency are produced between the driving signal frequency $Nf_0 + \Delta f$ and the harmonic frequency components of the probing pulse repetition rate f_0. The lowest frequency component produced Δf is isolated from other components at higher frequencies by the frequency-domain data acquisition system (*e.g.* low-pass filter, which is a low speed electronic circuit).

Measurement of the power and phase at Δf, as the drive frequency is varied in a frequency band, gives the frequency response of the device in this frequency band.

2.2.3 External E-O sampling

External E-O sampling has shown promising results in characterizing monolithic microwave integrated circuits (MMICs) as well as other high speed electronics devices. This is due to its high frequency capability and noninvasive property of measuring internal node signals in MMICs and any planar circuits without electro-optic (*e.g.* GaAs) circuit substrates [22, 30]. In addition, external E-O sampling, which incorporates a birefringent dielectric probe immersed in the electric field to be measured, affords great versatility of measurement.

System set-up

Figure 2.5 is an optics schematic of an external E-O sampling system, which is same as the set up in the lab at McMaster University where the primary work of this thesis has been conducted. The probe is a truncated square pyramid of silica with a thin layer of birefringent material ($LiTaO_3$ or GaAs) at its tip. The tip face is typically a fraction of a millimeter in size. The probe beam is depicted as reflecting off the probe face, so that it travels twice through the probe tip.

The external E-O sampling system utilizes a $LiTaO_3$ or GaAs probe above the circuit being tested. Laser beam pulses at the sampling repetition rate probe

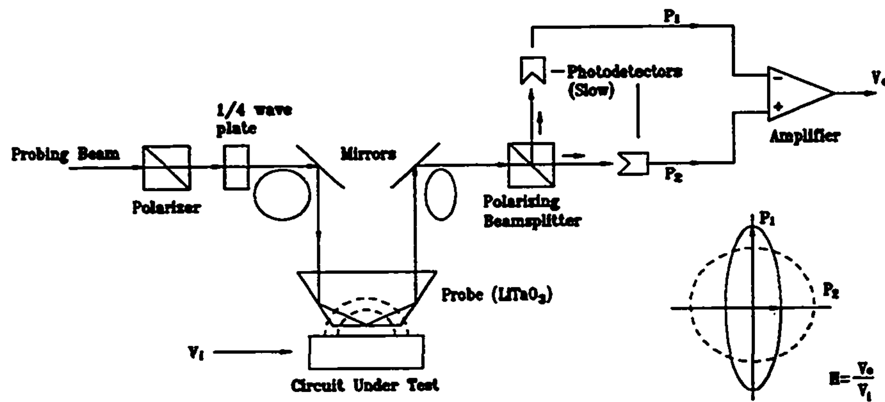

Figure 2.5: Optics schematic of the external E-O sampling. Change in polarization ellipticity of the probing beam can be detected by two slow photo detectors.

the electric field induced by the unknown voltage as the pulses propagate across the crystal. Two detectors are employed to measure intensities of the modulated laser beam at the polarization beam-splitter. These signals are then processed by a differential amplifier, a lock-in amplifier, and a signal averager. The differential system provides a means for making the detection system less susceptible to laser fluctuations while increasing the voltage sensitivity twofold. By means of a compensator, the modulator is optically biased at its quarter wave point in order to achieve linear E-O response and maximum sensitivity. The output may have its horizontal axis driven by the frequency offset Δf and its vertical axis by the signal averager output. The lock-in amplifier is tuned to the repetition rate of laser pulses f_0 to eliminate the high frequency harmonics and the noise outside the test band. Typically f_0 is about $82MHz$, N varies from 1 to 500 when driving frequencies are up to $40GHz$, and Δf is 10 to $100Hz$.

The sampling system can be grouped into three sections: the laser system for optical pulse generation, the microwave instrumentation for driving the circuit being tested, and the receiver system for signal processing and data acquisition. The laser system consists of a GaAs laser diode, a laser driving circuit, a pulse generator and a synchronizing system to ensure that the frequency of the microwave circuit driving signal is an integer multiple of repetition rate of laser pulses. The beam passes through a linear polarizer and a wave-plate to get a circularly polarized wave. Then it is focused through the fused Silica probe support down to the electro-optic probe tip with a microscope objective to a small spot ($< 10\mu m$) on the probe facet. Polarization of the probing beam is deformed to an ellipsoidly polarized wave due to birefringence caused by the electric field in the probe tip. The reflected light, *i.e.* the probing beam output, is separated to horizontally and vertically polarized components by a polarizing beam-splitter and respectively detected by two photo diodes connected to a differential amplifier. Since polarization of the wave can be described in terms of the amplitudes and the phase angles of the x and y components of the electric field vector, ellipticity of the reflected light polarization at the beam-splitter can be measured according to the output of the amplifier.

To drive the circuit being tested, a microwave synthesizer generates either sinusoidal excitation for microwave circuits or the clock/data signals for digital circuits. For wafer level testing of ICs, the drive signal is delivered with a microwave probe station.

It is critical for signal processing to achieve accurate and shot noise limited

measurements. Harmonic mixing is used for vector voltage measurements. The synthesizer is set to an exact multiple of the laser repetition rate plus a 1-10 MHz frequency offset, and the receiver is configured as a synchronous detector (i.e., an RF lock-in amplifier) to measure magnitude and phase of the received signal at the offset frequency. Equivalent time sampling is used to view time waveforms. The synthesizer is set to an exact multiple of the laser repetition rate f_0, plus a small frequency offset Δf. Pulse modulation, or fast offset/averaging signal processing is required to suppress laser intensity noise. The resulting signal varies at the slow offset rate Δf in proportion to the detected signal [17].

Both optical and electrical excitation configurations as shown in Figure 2.3 and Figure 2.4 can be applied to external E-O sampling. A sinusoidal electrical signal is used to drive the device being tested in our system. In this system, two frequency synthesizers, both locked to the same reference, generate respectively a high frequency electrical sinusoidal signal to excite a circuit being tested and pulses to drive a solid state diode laser. The high frequency synthesizer emits a frequency which is N times the frequency of the laser pulse repetition rate f_0 plus a small offset Δf. Thus this system enables the sampling pulse to trace temporal waveform of the electric field in the probe tip, which is proportional to the signal in the device being tested.

2.3 Invasiveness, Distortion and Calibration

While GaAs probes have just been receiving attention [2] [3], E-O probes made of $LiTaO_3$ are widely used for external sampling. However, both $LiTaO_3$ and GaAs are dielectrics which disturb the operation of the device being tested. This undesirable effect is called invasiveness as previously defined in Chapter 1.2. Although some preliminary experiments on the invasiveness of $LiTaO_3$ and GaAs probes have been touched upon [2, 3, 7], there is no report on quantitative comparison in systematic ways. On the other hand, the E-O response obtained from the probe may be distorted in relation to the electrical response of the device being tested. To evaluate and de-embed distortion from the measured E-O response, the external probes need to be characterized. Specifically, estimating the E-O response of the probe requires a detailed calculation of the field intercepted by the probing beam as it travels through the birefringent probe tip. Field distribution in the optical probe tip can be significantly different from the uniform field which is assumed in previous research [5] to simplify their analysis. A full wave analysis and a field transient response of the probe tip are desirable for quantitative investigation of both invasiveness and distortion in external E-O sampling.

Furthermore, research on invasiveness to device operation and distortion of measured signal is highly demanded by the application of external E-O sampling in quantitative measurement, especially in the sub-picosecond domain. In fact, most E-O sampling measurements have been done only in relative terms [5, 16, 17].

Investigation of the problem shows that field disturbances due to probing discontinuities and field response of the probe tip are sources of the invasiveness and the distortion in external E-O sampling [7, 16, 31, 32]. To evaluate the invasiveness and characterize the distortion, a full wave field analysis of the external E-O sampling is required. It is believed that a field-based calibration technique is the reliable and feasible way to extend E-O sampling to quantitative measurement in picosecond and sub-picosecond domain.

2.4 Conclusions

This chapter has briefly reviewed the physics of electro-optic sampling, three kinds of sampling geometries (*i.e.* direct, hybrid and external samplings) and two types of system implementation (*i.e.* optical and electrical excitations).

It is necessary to systematically analyze and investigate the probing invasiveness and the signal distortion in electro-optic sampling system in order to develop a calibration technique for quantitative measurement especially in picosecond and sub-picosecond domain.

Chapter 3

Field and E-O Response Simulation in External E-O Sampling

This chapter provides a brief review of the finite-difference time-domain (FD-TD) field simulation technique, which is used in this thesis due to its full wave time domain nature. Moreover, it proposes a new and faster FD-TD algorithm, which demonstrates 10%-50% improvement in computational efficiency of the FD-TD method. Finally the method for E-O response calculation is presented for the first time based on the field distribution in time domain in the probe tip.

3.1 Introduction

External E-O sampling measures the electric field produced by the signal voltage on the device being tested. The electric field produces birefringence in an externally

introduced electro-optic crystal *probe* suspended near the device being measured. This birefringence changes the polarization of the probing beam through the crystal. This change is converted to an electrical measurement by photo detectors following the polarization analyzer. External E-O sampling is attractive for its ability to measure internal node fields of planar circuits without electro-optic circuit substrates. E-O probes made of $LiTaO_3$ or GaAs are currently widely used for external sampling. These probe materials, however, generate probing invasiveness due to large dielectric discontinuities. Although some preliminary experiments on the invasiveness of $LiTaO_3$ and GaAs probes have been touched upon [2, 3, 7, 33], a quantitative comparison has not been conducted systematically. In addition to probing invasiveness to the device operation, the field response in the probe tip can be very different from the field in the device being tested due to the probing discontinuities. The E-O effects, thus, may produce distinctive results in E-O sampling measurement. This possible difference is defined as *distortion*.

It is desirable to develop a calibration technique to *de-embed* the distortion and invasiveness from the sampled measurement results. In order to do so, the probing invasiveness and distortion in external electro-optic sampling need to be addressed thoroughly. Some investigations have already been carried out on these topics [7, 8, 31, 32, 34, 35]. However, the following technical problems still remain unsolved.

1. Quantitative characterization of the probe invasiveness and distortion as function of the probe material, dimension and placement.

2. Field transient response in the probe tip and its effects on E-O sampling results.

3. Quantitative relation between E-O sampling results and the field response in the device under test.

4. Evaluation of the probe misalignment effects and correction method.

A full-wave field modeling and E-O effect calculation are required in order to address these problems. A two-dimensional static field model of an E-O probe has been used to analyze invasiveness of the measurement system [35], where a uniform field is assumed in the CPW transmission direction. The invasiveness of E-O probing was investigated using the Bergeron method in [35], where TEM mode propagation was assumed. As far as the high frequencies are concerned, this assumption may not hold. Since the external probe birefringent material has a large dielectric constant, this assumption is questionable at least for ultrashort pulses. Such a problem warrants full-wave three-dimensional field simulation and transient analysis, which cannot be easily conducted by using other analytical techniques based on the TEM-mode assumption and the quasi-static field approximation. The Finite-Difference Time-Domain (FD-TD) method is well suited to the problem and chosen as analytical simulation technique in this thesis based on following reasons.

1. The FD-TD method is a well developed and widely used full wave time domain analytical technique. It differs from any other full wave analysis in the sense that the field is simulated in the time domain first, which is

perfectly matched to E-O sampling problems since E-O sampling systems by nature make temporal waveform measurements.

2. For E-O sampling system modeling, it is important to measure the transient response, to model discontinuities and to simulate field distribution inside the probe. Then the E-O response can be properly characterized. The FD-TD method makes it possible to include high speed signals and dispersive effects in the modeling, which could not be easily considered using other techniques. In addition, the FD-TD method can simultaneously simulate the transient response, discontinuities effects, and the field distribution in E-O sampling system.

3. The boundary conditions at complex discontinuity geometries can be easily localized in the FD-TD algorithm. No special attention has to be paid to the boundary conditions since they are automatically satisfied in the modeling.

4. To investigate the E-O response which is the sampled output signal in E-O sampling, detailed temporal field information along the probing beam path is required. The FD-TD method automatically offers these results.

5. Frequency domain information over the entire range of interest, such as S-parameters, may be obtained by the Fourier transform of the response to a broad-band pulse. This allows analysis of the system transient response, the wide band system characterization as well as the quasi-static fields analysis through a single simulation in time domain using the FD-TD method.

In this chapter, the FD-TD method is reviewed briefly and its several technical aspects are discussed so as to provide a basis for the field simulation in electro-optic sampling. Moreover, a faster FD-TD method for transmission-line-like problems is proposed. It demonstrates a significant improvement in computational efficiency.

3.2 The FD-TD method

The frequency domain finite-difference, finite-element, and moment methods are often used to solve electro-magnetics problems [36, 37, 38]. With these methods, the spatial domain is discretized and the corresponding discretized field values are treated as unknowns which can be found by solving a large system of linear equations. However, with the finite-difference time-domain (FD-TD) method, both time domain and spatial domain of interest are discretized using finite-difference approach. Moreover, the FD-TD method solves the unknown fields in time domain with an explicit equation using time marching technique in physics term or recursive functions in mathematics term [39]. The electro-magnetic wave propagation in the region of interest is then treated as an initial value problem.

3.2.1 Discretization

The FD-TD method is formulated by discretization of Maxwell's curl equations over a finite volume and approximating the derivatives with centered difference

approximations. A description of the discretization method of Maxwell's curl equations was originally reported by Yee [40]. Figure 3.6 shows Yee's mesh, in which the electric and magnetic fields are spatially interlaced. In addition, the three electric and magnetic field components are also spatially interlaced. Within each cell, the electric fields are placed along the edges, and the magnetic fields are placed at the face centers. The spatial and temporal derivatives are approximated in a finite difference manner which provides accuracy to the second order (*i.e.*, errors are proportional to the square of the grid separations or time steps). Notice that the discretization errors are the only fundamental error source in the FD-TD algorithm. This field-component arrangement provides the basis to formulate the discretized Maxwell's curl equations.

3.2.2 The FD-TD algorithm

Maxwell's curl equations are

$$\frac{\partial \vec{E}}{\partial t} = \frac{1}{\epsilon} \nabla \times \vec{H} \tag{3.45}$$

$$\frac{\partial \vec{H}}{\partial t} = -\frac{1}{\mu} \nabla \times \vec{E} \tag{3.46}$$

Equations (3.45) and (3.46) are equivalent to the following set of scalar equations defined in Cartesian coordinates.

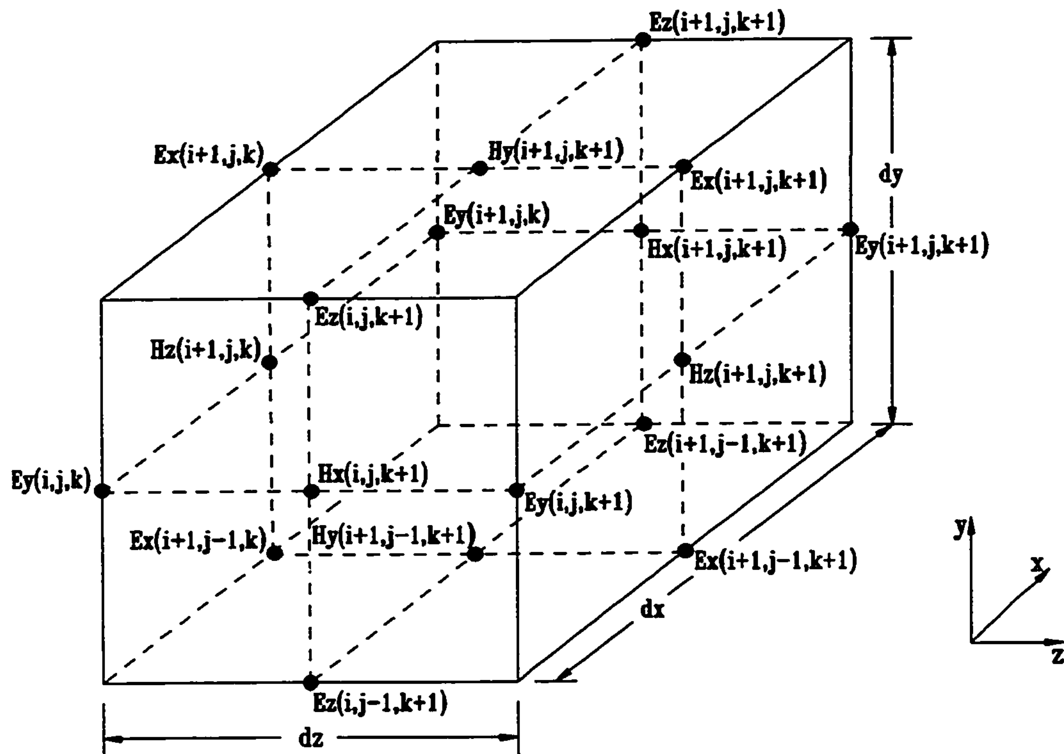

Figure 3.6: Field-components placement in the FD-TD unit cell, Yee's mesh. The electric and magnetic fields are spatially interlaced while their components are interleaved in space as well.

$$\frac{\partial H_x}{\partial t} = \frac{1}{\mu}(\frac{\partial E_y}{\partial z} - \frac{\partial E_z}{\partial y}) \tag{3.47}$$

$$\frac{\partial H_y}{\partial t} = \frac{1}{\mu}(\frac{\partial E_z}{\partial x} - \frac{\partial E_x}{\partial z}) \tag{3.48}$$

$$\frac{\partial H_z}{\partial t} = \frac{1}{\mu}(\frac{\partial E_x}{\partial y} - \frac{\partial E_y}{\partial z}) \tag{3.49}$$

$$\frac{\partial E_x}{\partial t} = \frac{1}{\epsilon}(\frac{\partial H_z}{\partial y} - \frac{\partial H_y}{\partial z}) \tag{3.50}$$

$$\frac{\partial E_y}{\partial t} = \frac{1}{\epsilon}(\frac{\partial H_x}{\partial z} - \frac{\partial H_z}{\partial x}) \tag{3.51}$$

$$\frac{\partial E_z}{\partial t} = \frac{1}{\epsilon}(\frac{\partial H_y}{\partial x} - \frac{\partial H_x}{\partial y}) \tag{3.52}$$

The FD-TD algorithm is developed from these six partial differential equations of (3.47)-(3.52).

Using the field-component arrangement defined in Figure 3.6, these equations (3.47)-(3.52) are discretized with the first-order centered difference approximations on both time and spatial domains. This is the foundation of the FD-TD method with which field components can be solved in a more efficient way. Advantages of the FD-TD method can be seen from the fact that centered differences are realized in the calculation of each field component and that continuity of tangential field components is automatically satisfied. Appropriate boundary conditions are enforced on the source, conductors, and mesh walls wherever they should be applied. The entire computational domain is obtained by stacking these rectangular cubes into a larger rectangular volume. By applying this field-component arrangement and the centered difference approximations to (3.47)-(3.52), explicit

formulations of the FD-TD method may be derived as:

$$H^{n+1/2}_{x_i,j,k} = H^{n-1/2}_{x_i,j,k} + \frac{\Delta t}{\mu\Delta z}(E^n_{y_i,j,k} - E^n_{y_i,j,k-1}) - \frac{\Delta t}{\mu\Delta y}(E^n_{z_i,j,k} - E^n_{z_i,j-1,k}) \tag{3.53}$$

$$H^{n+1/2}_{y_i,j,k} = H^{n-1/2}_{y_i,j,k} + \frac{\Delta t}{\mu\Delta x}(E^n_{z_i,j,k} - E^n_{z_i-1,j,k}) - \frac{\Delta t}{\mu\Delta z}(E^n_{x_i,j,k} - E^n_{x_i,j,k-1}) \tag{3.54}$$

$$H^{n+1/2}_{z_i,j,k} = H^{n-1/2}_{z_i,j,k} + \frac{\Delta t}{\mu\Delta y}(E^n_{x_i,j,k} - E^n_{x_i,j-1,k}) - \frac{\Delta t}{\mu\Delta x}(E^n_{y_i,j,k} - E^n_{y_i-1,j,k}) \tag{3.55}$$

$$E^{n+1}_{x_i,j,k} = E^n_{x_i,j,k} + \frac{\Delta t}{\epsilon\Delta y}(H^{n+1/2}_{z_i,j+1,k} - H^{n+1/2}_{z_i,j,k}) - \frac{\Delta t}{\epsilon\Delta z}(H^{n+1/2}_{y_i,j,k+1} - H^{n+1/2}_{y_i,j,k}) \tag{3.56}$$

$$E^{n+1}_{y_i,j,k} = E^n_{y_i,j,k} + \frac{\Delta t}{\epsilon\Delta z}(H^{n+1/2}_{x_i,j,k+1} - H^{n+1/2}_{x_i,j,k}) - \frac{\Delta t}{\epsilon\Delta x}(H^{n+1/2}_{z_i+1,j,k} - H^{n+1/2}_{z_i,j,k}) \tag{3.57}$$

$$E^{n+1}_{z_i,j,k} = E^n_{z_i,j,k} + \frac{\Delta t}{\epsilon\Delta x}(H^{n+1/2}_{y_i+1,j,k} - H^{n+1/2}_{y_i,j,k}) - \frac{\Delta t}{\epsilon\Delta y}(H^{n+1/2}_{x_i,j+1,k} - H^{n+1/2}_{x_i,j,k}) \tag{3.58}$$

where Δx,Δy, and Δz are respectively discretization distances in each direction of space whereas Δt is the time increment. Any function value at the spatial point (x, y, z) and time instant t is denoted as:

$$F^n(i, j, k) = F(i\Delta x, j\Delta y, k\Delta z, n\Delta t) \tag{3.59}$$

where i, j, k and n are integers. Equations (3.53)-(3.58) indicate that electric and magnetic fields are also temporally interlaced with each other in the FD-TD algorithm to achieve centered differences for the time derivatives. In other words, recursive functions (3.53)-(3.58) are established so that both E-field and H-field variables at any given time are defined in terms of themselves at previous instants.

In order to solve three-dimensional fields in time domain using the FD-TD method, the algorithm is suggested as follows:

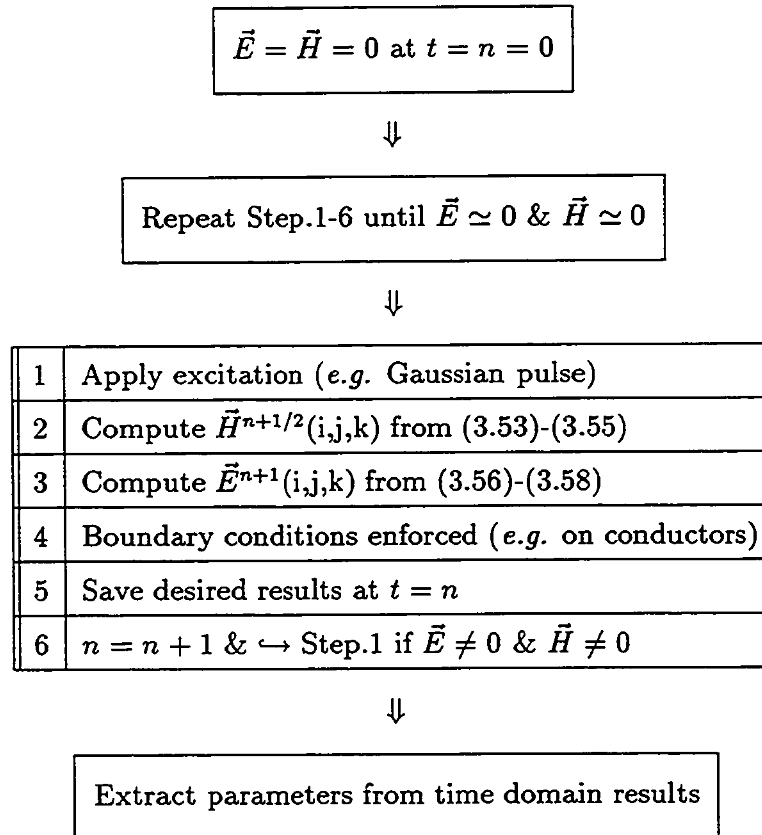

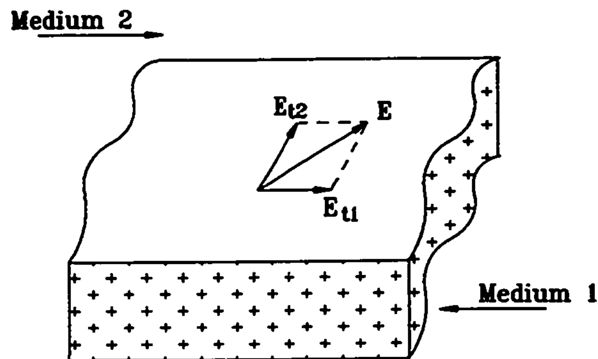

Figure 3.7: Fields at a interface between two media. The field at the interface can be calculated by Maxwell's equations given the value $\epsilon_{interface}=\frac{\epsilon_1+\epsilon_2}{2}$.

3.2.3 Discontinuities

For tangential components of the electric field at two different dielectric material interfaces as shown in Figure 3.7, the average of the two permittivities

$$\epsilon_{interface} = \frac{\epsilon_1 + \epsilon_1}{2} \tag{3.60}$$

is used for field computation. This can be confirmed given the fact that tangential components at the dielectric interface are continuous [41]. The situation where the field components are normal to the dielectric interface between two media would not happen if attention is paid when a spatial grid is defined using Yee's mesh.

In Yee's mesh, the arbitrary geometries are approximated by staircases, which gives an advantage that any discontinuity and boundary conditions can

be easily described or enforced locally. On the conductor surface, for example, tangential components of the electric field can be conveniently set to zero. Thus the discontinuity and boundary conditions are automatically satisfied in the calculated field results.

3.2.4 Absorbing boundary conditions

One of the major problems in the implementation of the FD-TD algorithm is that it is computationally intensive. For any practical problem, a finite computational domain has to be carefully defined for computation efficiency and feasibility of the analysis. The difference equations (3.53)-(3.58) cannot be used to evaluate field components tangential to the outer boundaries since they require the values of field components outside of the defined domain. In this case, the absorbing boundary condition is used to specify tangential electric field components on the outer mesh walls in such a way that outgoing waves are not reflected back to the computational domain. As it is known, the outgoing waves are determined by tangential electric fields on the outer boundaries. Therefore, it is reasonable to assume that tangential electric fields on the outer boundaries obey the one-dimensional wave equation in the direction normal to the mesh wall. If $\hat{n}$ is the direction normal to the mesh wall as shown in Figure 3.8, the wave equation for the wave propagating in $\hat{n}$ is [23]

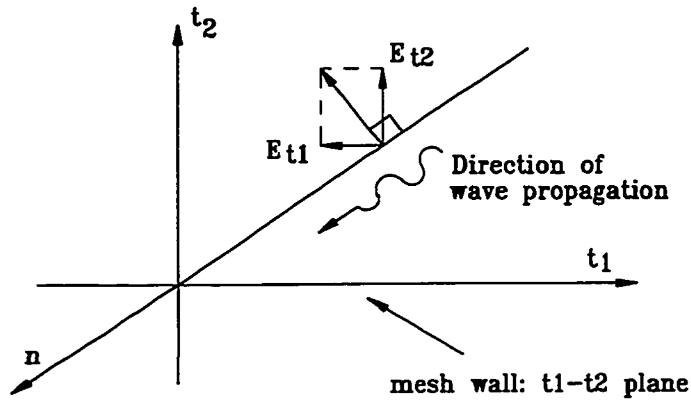

Figure 3.8: One-dimensional wave at the mesh wall, defined by t_1-t_2 plane, in the direction $\vec{n}$ normal to the mesh wall. This wave is determined by the tangential electric fields E_{t1} and E_{t2} on the mesh wall.

$$\left(\frac{\partial}{\partial n} - \frac{1}{v}\frac{\partial}{\partial t}\right) E_{tan} = 0 \tag{3.61}$$

where $\hat{n}$ can be either x, y or z in Cartesian coordinates and E_{tan} refers to tangential electric field components with respect to the mesh wall or transversal components to the wave propagation direction.

This equation is Mur's first-order absorbing-boundary condition [42]. It can be discretized only by the field components on or just inside the mesh wall, yielding an explicit finite difference equation (3.62) which is used in the FD-TD algorithm as absorbing boundary condition.

$$E_0^{n+1} = E_1^n + \frac{v\Delta t - \Delta n}{v\Delta t + \Delta n}(E_1^{n+1} - E_0^n) \tag{3.62}$$

where E_0 refers to the tangential electric field components on the mesh wall and

E_1 represents the tangential electric field components one node inside of the mesh wall.

In this thesis, the absorbing boundary condition (3.62) is used [42, 43]. It is sufficiently accurate since the outgoing wave is normal to the mesh wall on the boundaries of computational domain defined for the field simulation in the external E-O sampling problem.

3.2.5 Stability and errors

As mentioned previously, the centered finite-difference approximations are used for discretization of the space and time derivatives in (3.53)-(3.58). This technique produces second order error in both space and time steps, yielding any function $F(i, j, k)$

$$\frac{\partial F(i,j,k)}{\partial n} = \frac{\Delta F(i,j,k)}{\Delta n} + O(\Delta n^2) \tag{3.63}$$

$$\frac{\partial F(i,j,k)}{\partial t} = \frac{\Delta F(i,j,k)}{\Delta t} + O(\Delta t^2) \tag{3.64}$$

The maximum time step that may be used is limited by the stability restriction of the finite difference equations,

$$\Delta t \leq \frac{1}{v_{max}} \left(\frac{1}{\Delta x^2} + \frac{1}{\Delta y^2} + \frac{1}{\Delta z^2} \right)^{-1/2} \tag{3.65}$$

where v_{max} is the maximum velocity of light in the defined computational domain.

Furthermore, the maximum mesh increment is limited by the frequency range of interest. If f_{max} is the upper limit of the frequency concerned, the maximum mesh increment $\Delta\ell$ is chosen to meet following requirements:

$$\begin{aligned}\Delta\ell &\leq \frac{1}{N}\lambda_{min} \\ &\leq \frac{1}{N}\frac{v_{min}}{f_{max}} \end{aligned} \tag{3.66}$$

$$N = 15 \sim 20 \tag{3.67}$$

where λ_{min} is the wavelength corresponding to f_{max}, and v_{min} is the minimum speed of propagating wave in the computational domain, which may be described as a function of the effective dielectric constant.

Based on the brief review on the FD-TD method, the field in external E-O sampling is to be solved in following chapters.

3.3 A faster FD-TD algorithm

Though extensively used for electro-magnetic field analysis, The FD-TD method is very expensive because a large amount of computation time and memory space are required. This is due to the fact that the space steps must be a fraction of both

the minimum wavelength concerned and that of the structural component encountered. In addition, the simulated spatial structures and components usually span many wavelengths. Furthermore, the time steps used are limited by the stability restriction of the finite difference equations and frequency resolution required in the analysis. Major efforts to improve the efficiency of the FD-TD method have yielded techniques using variable meshes [44, 45]. Recently, the static-field solutions have been incorporated into the FD-TD algorithm for the same purpose [46, 47]. In this section, a faster FD-TD algorithm[19, 20] is developed to improve its computational efficiency. This technique is particularly suitable for transmission-like problems, which include E-O sampling field analysis and other majority of the practical field simulation problems. A significant improvement will be demonstrated in the following sections.

3.3.1 Technique

In field analyzes using FD-TD method, what needs to be concerned are the impulse response, the characteristic impedance and the effective dielectric constant. This requires only the transmission response of the system and at most one time reflection response. It is obvious that the initial electro-magnetic excitation has no effect beyond any point which it can reach, given the knowledge of its maximum speed of propagation. As well known, this speed is considerably lower than the speed of light in typical MMIC devices which often use GaAs ($\epsilon_r = 13.2$) as a substrate. This allows significant savings on computations by defining moving boundaries in the spatial domain at the excitation's maximum possible range during its beginning

period. With the proposed faster FD-TD algorithm, the boundaries are initially defined to enclose the initial excitation area plus a mesh buffer region. During computation, the boundaries are expanded at the maximum propagation speed. Figure 3.9 shows how the boundaries are expanded as time goes on.

Formulations of the moving boundary are as follows

$$N_i(n) = \frac{V_{max,i} n \Delta t}{\Delta h_i} + n_0 \quad (3.68)$$

$$V_{max,i} = \frac{c}{\sqrt{\epsilon_{eff,i}}} \quad (3.69)$$

where $i = 1, 2$, and 3 correspond to the three orthogonal axes, and $V_{max,i}$ is the maximum speed of the wave for the specific direction of propagation. $N_i(n)$ is the mesh number which is increased with time. n_0 is an integer constant defining the mesh buffer region. Other notations follow previous FD-TD conventions.

$V_{max,i}$ in (3.69) can be chosen as the speed of light c for all directions in general. Once the spatial computation domain is adjusted in time, a reduction in computation requirement can be achieved without causing extra errors to the results.

For microstrip and coplanar waveguide problems, most of the energy is transmitted in their substrate, and the propagating wave can be assumed to have the speed

$$v_g = \frac{c}{\sqrt{\epsilon_{eff}}} \quad (3.70)$$

where typically $\epsilon_{eff} = 7.7$ for the CPW on GaAs substrates [9].

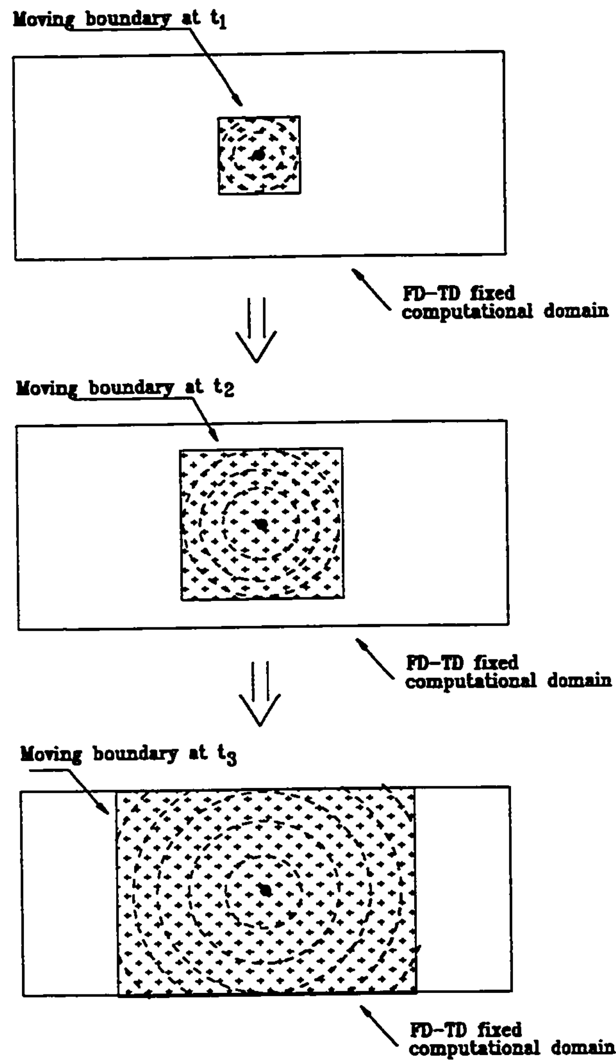

Figure 3.9: Computational domain boundaries are expanded as time goes on after excitation.

It is noted that v_g is usually significantly lower than the speed of light. Therefore, in waveguide problems, the moving boundaries can be defined by $V_{max,i} = v_g$ rather than by the speed of light for a greater saving in computation.

A small component of the field will indeed propagate at the speed of light in the air above the substrate, but it will be shown that discrepancies due to this "fast wave" [48] with respect to a conventional simulation are negligibly small.

The technique presented in this thesis can be applied to any problem where the simulated field is completely localized with respect to the mesh region for at least part of the history of the simulation.

As an example, the impulse response of a 50Ω coplanar waveguide on a GaAs substrate is calculated using both unmodified and moving boundary FD-TD methods. The computational domain is defined by the volume $86\Delta h_x * 28\Delta h_y * 425\Delta h_z$, where $\Delta t = 0.01ps$, $\Delta h_x = 8\mu m$, $\Delta h_y = 5\mu m$ and $\Delta h_z = 10\mu m$.

3.3.2 Results

Figure 3.10 shows the reduction in computation time compared to the conventional FD-TD method when transmission and reflection in the waveguide are considered. It is observed that using $V_{max,i} = c$ realizes respective savings of 20% and 10% whereas using $V_{max} = v_g$, the speed of propagation in the substrate for the coplanar waveguide problem, allows respective savings as high as 50% and 25%. Figure 3.11 compares the results of conventional FD-TD and those of moving boundary

FD-TD for the coplanar waveguide analysis when the moving boundary in wave propagation direction is defined by v_g. It can be seen that even up to 200GHz the discrepancies are negligibly small.

As shown in the presented example, savings in computation time of 20% for transmission and 10% for both transmission and reflection analyzes have been achieved. With the moving boundary defined by v_g or the effective dielectric constant in propagation direction, savings reach more than 50% for transmission, and 25% for transmission and reflection analyzes. The concept of this technique can also be applied to other time domain field analysis methods such as the TLM method (Transmission line method). For problems involving multiple reflection analysis, however, the savings become less significant with this modification.

3.4 Optical signal calculation

Birefringence in the E-O probe is a function of the electric field which penetrates the crystal and is fully described by electric-optic tensor of the material. Having obtained the field distribution in the probe using full wave analysis, birefringence along the path of the probing beam (*i.e.* a double vertical pass) can be integrated to give a predicted change in the beam polarization. This change, as the optical signal desired, yields an electrically measurable voltage when analyzed and detected by photo-detectors.

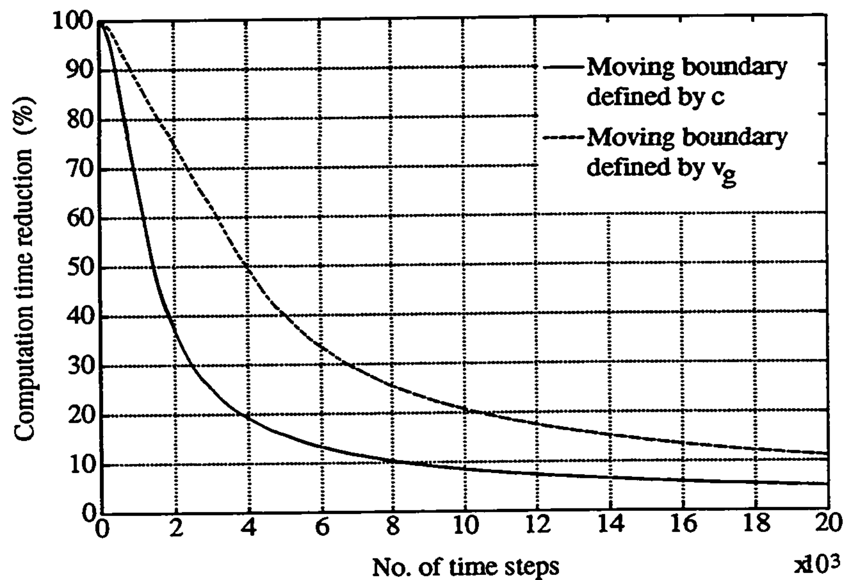

Figure 3.10: Computation time reduction using moving boundaries with FD-TD method in a coplanar waveguide analysis. The computation domain is defined by $86\Delta h_x * 28\Delta h_y * 425\Delta h_z$. 4000 time steps represents the wave transit time for the region. 20% saving in computation time for transmission, corresponding to 4000 time steps, and 10% saving for both transmission and reflection analyzes can be achieved without introducing error. With the moving boundaries defined by the wave velocity in the substrate, 50% and 25% savings in computation time can be observed for corresponding situations.

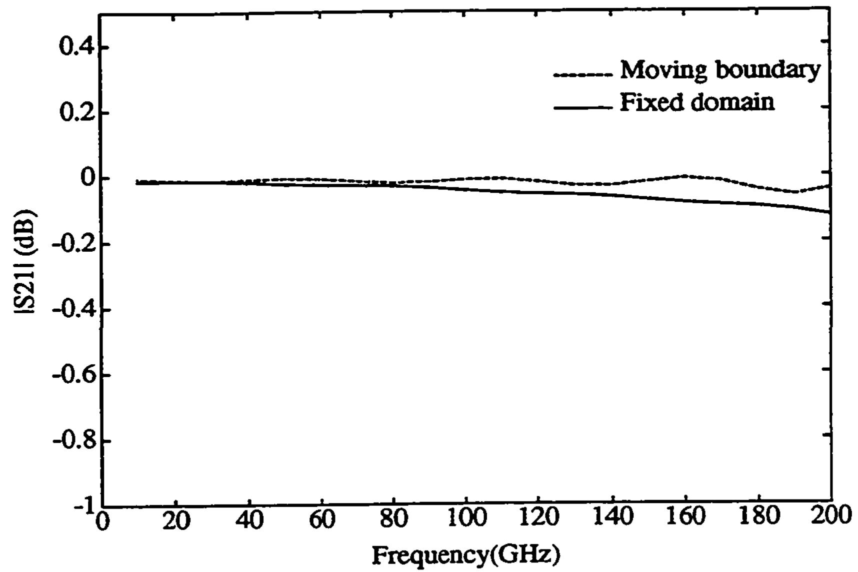

(a)

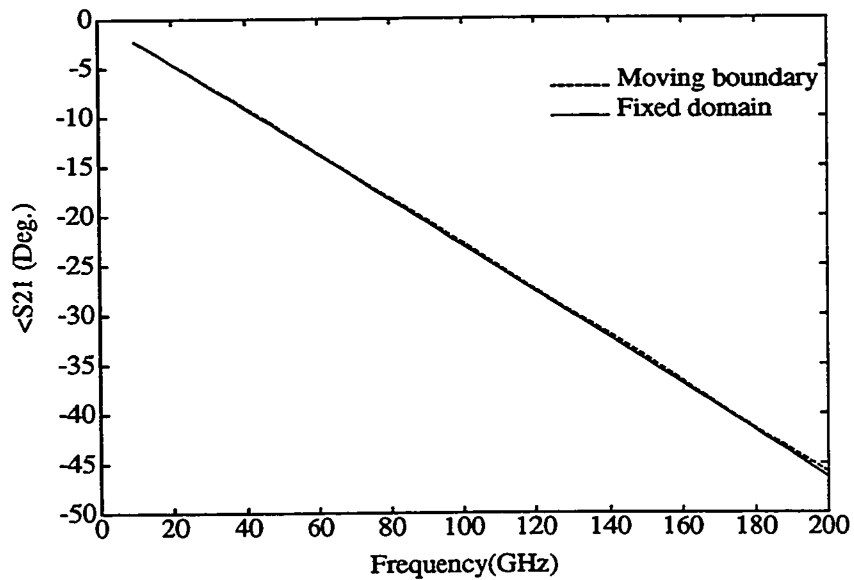

(b)

Figure 3.11: Comparison of the transmission coefficient S_{21} of the coplanar waveguide obtained in FD-TD method with fixed domain and moving boundaries defined by v_g or effective dielectric constant. Discrepancies are less than 0.1dB up to 200 GHz.

There are two arrangements for external probing, transverse and longitudinal. Transverse probing reacts to field components that are parallel to the surface of the circuit. Longitudinal probing interacts with field components that emanate normal to the metalization lines. In the simulation presented in this thesis, the optical probing beam is in the y-direction as shown in Figure 3.12 for both $LiTaO_3$ and GaAs probes. Since $LiTaO_3$ and GaAs are used respectively for transverse and longitudinal probing, the sampling-beam position within the crystal is just above the center of the CPW slot spacing for $LiTaO_3$ probes and above the center of the CPW conductor strip for GaAs probes, as shown in Figure 3.13. The optical axis (*i.e.* c-axis) of $LiTaO_3$ probes are chosen to be parallel to the z-axis (Figure 3.12). Therefore, the electro-optic tensor in which z-axis is defined as optic axis, can be directly used without any modification for axes orientation. The orientation of GaAs probes requires no special attention because of its $\bar{4}3m$ crystal symmetrical structure.

The propagation of light through the probe is described by the index ellipsoid (2.17) or (2.20) in matrix form [49]. The electric field changes the coefficients in the index ellipsoid in (2.17) due to the birefringence. This change may be described using (2.21) or (2.24). From these equations, a field dependent index ellipsoid is obtained. The principal axes and their corresponding refraction indices of the resultant index ellipsoid can be found by diagonalization of the ellipsoid matrix in (2.20). Considering the spatially distributed electric field obtained from the FD-TD simulation, the retardation Γ of a probing beam along the y-direction

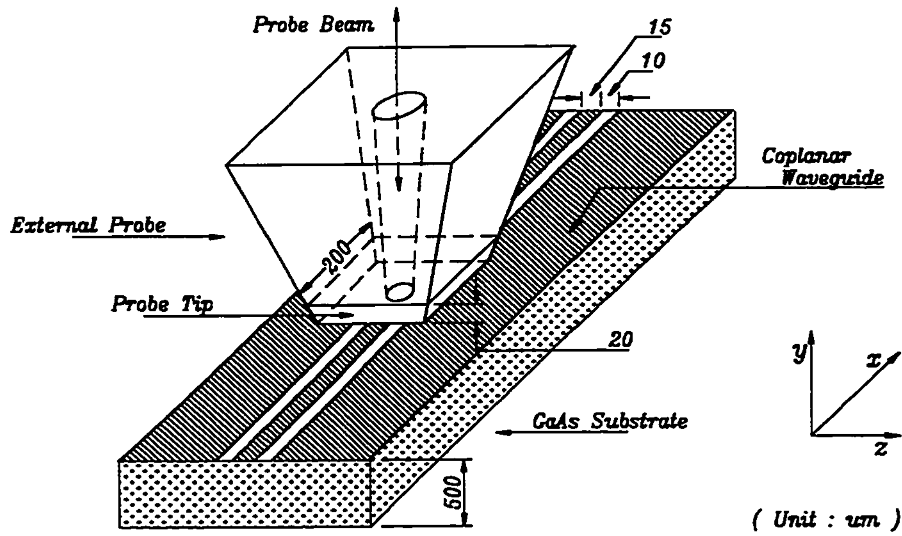

Figure 3.12: Schematic of the external electro-optic sampling configuration. The coplanar waveguide is the device being tested. The probe beam is ideally a few microns in diameter. The optical axis of the $LiTaO_3$ probe is parallel to the z-axis. The orientation of a GaAs probe does not require special attention.

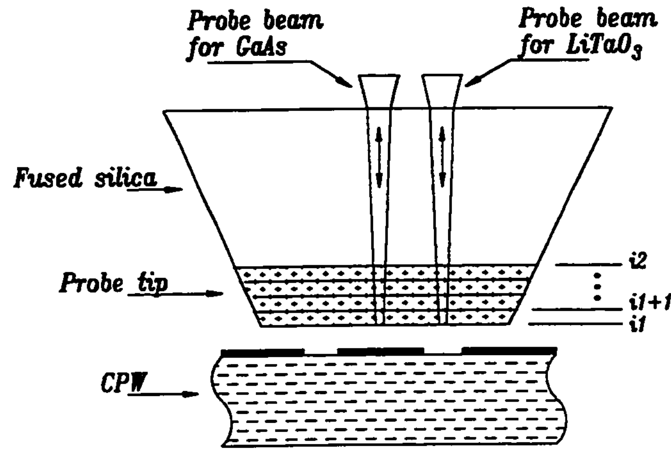

Figure 3.13: Cross-sectional view of external electro-optic probe and coplanar waveguide. Different sampling-beam positions within the probe tip are shown for $LiTaO_3$ and GaAs probes, respectively. The sampling-beams intercept the electric field at mesh nodes $i1, i1+1, \cdots, i2$.

is given by the following discretized form in radians

$$\Gamma(E_x, E_y, E_z) = d\varphi_c + \sum_{i=i1}^{i2} \frac{4\pi}{\lambda} \left[n_{z'_i}(E_x, E_y, E_z) - n_{x'_i}(E_x, E_y, E_z) \right] \Delta y_i \qquad (3.71)$$

where Δy_i is the y-axis mesh size at ith node, and $i1$ and $i2$ are mesh indices used in the FD-TD analysis to define the probing light path in the probe tip as shown in Figure 3.13. Note that the refraction indices $n_{z'_i}$ and $n_{x'_i}$ are functions of the electric field at ith node. Combined with a static birefringence in the crystal, if applicable, $d\varphi_c$ is introduced by an optical compensator which is used to supply an optical bias of $\frac{\pi}{2}$ for a maximal and linear measurement response [50]. The coordinate systems denoted by x, y, z in (2.20) and x', y', z' in (3.71) are respectively principal axes of the index ellipsoid without and with the applied electric field. It is noted

that x, y, z and x', y', z' are not necessarily parallel to their own counter parts.

Practically, an optical polarization analyzer is used to measure the degree of birefringence induced in the probe. The retardation Γ due to birefringence yields a normalized optical analyzer output as [49]

$$\frac{I_0}{I_i} = \sin^2\left(\frac{\Gamma(E_x, E_y, E_z)}{2}\right) \tag{3.72}$$

where $\frac{I_0}{I_i}$ has been explicitly written as the function of the electric field. The optical signal power is detected by a photo-detector to yield an electrical measurement voltage.

In previous studies, the condition of E_x=E_y=0 is used with the assumption that disturbances to the field in the probe are negligible. Field simulations in this thes, however, show that the magnitudes of the three electric field components can be comparable in the probe because of dielectric discontinuities (See Figure 3.14). Therefore, all three field components are taken into account in the optical signal calculations.

3.5 Conclusions

A full-wave time domain field analysis technique is the best suitable candidate to serve for the simulation of E-O sampling systems. The FD-TD method is chosen in this thesis. To improve computational efficiency of the FD-TD method, the moving boundary technique can be applied if the simulated field is limited in range at

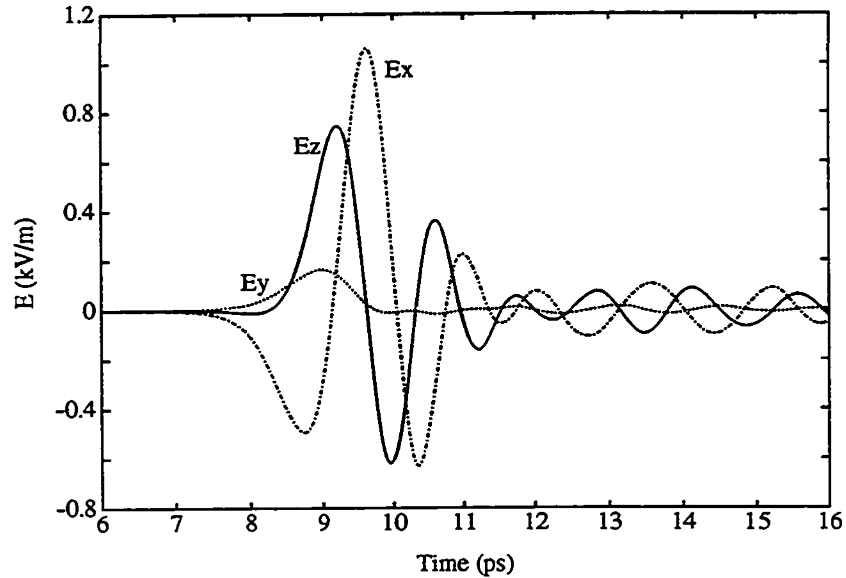

Figure 3.14: Magnitudes of the three electric-field components in $LiTaO_3$ probe when a Gaussian pulse is launched on the CPW. The probe distance is $5\mu m$. These three components are comparable with each other in magnitude due to dielectric discontinuities.

the beginning of the field excitation. Given the full wave three dimensional field distribution using the FD-TD method and the electro-optic tensor of the probe material, the E-O response of the sampling system can be calculated. This technique provides comprehensive knowledge and reliable results of the E-O response because no fundamental assumptions and approximations are involved throughout the simulation process.

Chapter 4

The invasiveness of external electro-optic sampling

This chapter presents the analytical results of probing invasiveness, which enable a quantitative comparison between $LiTaO_3$ and GaAs probes.

4.1 Introduction

The probing invasiveness of external E-O sampling is defined as the undesirable effect to the operation of the device being tested. It is caused by close placement of the high dielectric E-O probe. As mentioned previously, external E-O sampling measures the electric field produced by the signal voltage on a device being tested. The electric field, which is proportional to the signal, induces birefringence in an externally introduced electro-optic crystal probe. This birefringence may be detected by measuring the change in polarization ellipticity of the probing beam.

The magnitude of the sampled output signal produced for a given electric field and probe configuration defines E-O response of the probe. While sampling system sensitivity increases with the degree of field immersion, so does invasiveness induced by the probe. Given a tolerance of the invasiveness, therefore, it is useful to address the problem of an optimal placement of the probe and optical sampling point in the probe. The electrical effects, *i.e.* invasiveness, of the probe placement, material and dimensions are subjects of this chapter.

Problems of the invasiveness of E-O sampling system were raised several years ago [5]. Recently, when the external E-O sampling find more and more applications in measurement of microwave monolithic integrated circuits (MMICs) and other high speed ICs, the needs to comprehensively investigate the invasiveness become more urgent and crucial in extending this technique to quantitative measurement[7].

Previously, some investigations have already been carried out on the invasiveness [7, 17, 31, 32, 33]. The work reported can be divided into modeling studies and experimental analysis. In the modeling approach, either the TEM-mode analysis or the two-dimensional static-field calculations are conducted [32, 35]. A uniform field distribution is assumed in the direction of the CPW wave propagation. In experimental analysis [7, 17, 31, 33, 34], the loading effects of high dielectric probe are measured in terms of delay, or mismatching by either conventional electrical measurement techniques or placing a second probe on a transmission line between the signal source and sampling point. Generally, proximity of a strong

dielectric material to the transmission line causes a capacitive loading effect. It leads to a decrease in the characteristic impedance of a section of the transmission line over which the probe is placed. Thus, an equivalent characteristic impedance of this section of the transmission line is used to determine the probe invasiveness. It can be computed from either the modeling data or measured temporal delay.

The analysis of the probing invasiveness in external E-O sampling is a time domain field problem determined by the system configuration and three dimensional discontinuities. It requires a full wave three dimensional field simulation as well as transient response to picosecond and sub-picosecond pulses. For low speed or low frequencies, the TEM-mode assumption and the quasi-static field approximation in previous studies are likely to be valid. However, they are questionable in high frequency range or picosecond and sub-picosecond domain, which is highly demanded as operation frequency of devices and circuits goes higher and higher. The major problem, *i.e.* quantitative characterization of the probing invasiveness in sub-picosecond speed or terahertz frequencies, still remains unsolved. Consequently, most E-O sampling measurements have been done in relative terms or arbitrary units [5, 16, 17]. Calibration of the E-O sampling requires quantitative understanding of the probing invasiveness.

As mentioned in Chapter 3, the Finite-Difference Time-Domain (FD-TD) method [13] is well suited to the external E-O sampling problem. It is used to simulate the full wave time domain field around a coplanar waveguide on a GaAs

substrate in an external E-O sampling configuration. The results make it possible to evaluate, in terms of scattering parameters and delay in transmission, the invasiveness of external E-O sampling systems caused by probing discontinuities. It is followed by a comparison, for the first time, of the invasiveness and response of $LiTaO_3$ and GaAs probes. An equivalent circuit is proposed based on the field simulation results including the special treatment of probing discontinuities.

4.2 Field simulation and optical signal calculation

4.2.1 Field simulation parameters

For reasons mentioned previously, the FD-TD method is an ideal field analytical tool for external E-O sampling problem. It is apparent that field disturbances of the CPW quasi-TEM mode can only be observed and analyzed using three dimensional full wave field simulation. In addition, the information on field temporal history at any spatial position is provided by the result of field simulation in the FD-TD method. This information can be directly used for E-O effect calculation by means of electro-optic tensor as discussed in Chapter 2 and 3. Thus, the transient electric field in and around the probe is analyzed. Then scattering parameters of a measured coplanar waveguide (CPW) can be calculated and the temporal sampled signal as E-O sampling output may be derived as well.

For convenience of the discussion, Figure 3.12 is re-plotted as Figure 4.15.

It shows a schematic of the external E-O sampling set up for measurement of a CPW electric field. The probe, modeled after the commercially available Terametrics Model 200-TIR in this study, is a truncated square pyramid of silica with a thin layer of birefringent material ($LiTaO_3$ or GaAs) at its tip. The tip face, typically a fraction of a millimeter in size, is centered on and parallel to the CPW traces. A laser beam which travels down the axis of the probe and reflects off the tip at the *optical sampling point* suffers a change in polarization ellipticity from induced birefringence of the tip. This change yields an E-O measurement of the electric field at the optical sampling point. Since the probing beam, as depicted in Figure 4.15, reflects off the probe face, it travels twice through the probe tip. The FD-TD technique [13] is used to model the three dimensional field and Mur's first order absorbing boundary condition (3.62)[51] is applied to the computational domain boundary. Frequency domain information, such as S-parameters, is obtained through Fourier transformation. This allows analysis of the system transient response as well as the quasi-static fields.

In the following discussion, the electric field vector is defined as:

$$\vec{\mathbf{E}} = E_x\hat{\mathbf{x}} + E_y\hat{\mathbf{y}} + E_z\hat{\mathbf{z}} \tag{4.73}$$

$$\vec{\mathbf{H}} = H_x\hat{\mathbf{x}} + H_y\hat{\mathbf{y}} + H_z\hat{\mathbf{z}} \tag{4.74}$$

The simulation deals with a 0.6 ps full-width at half-maximum (FWHM) Gaussian pulse launched in the x-direction towards the probe with an applied

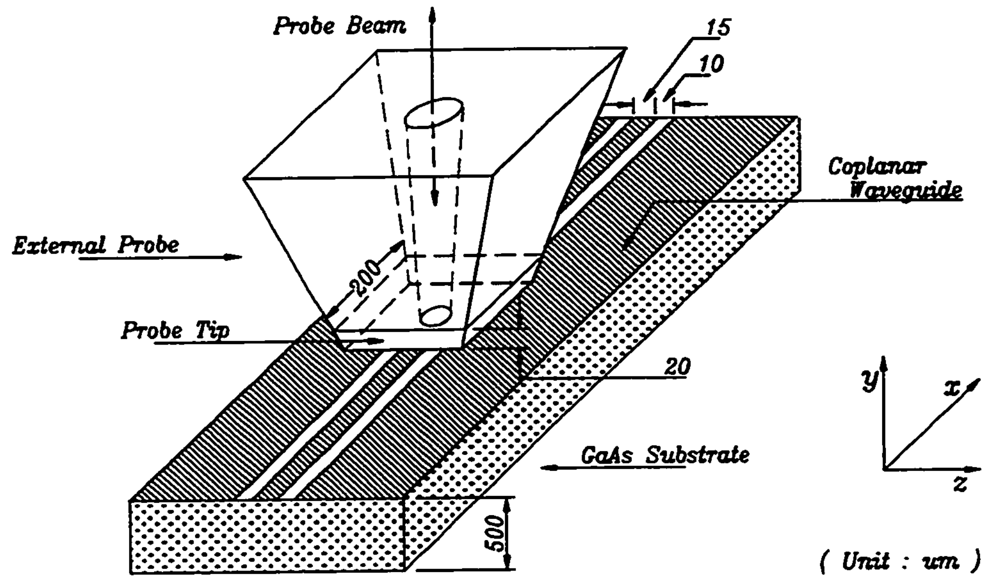

Figure 4.15: Schematic of the external electro-optic sampling configuration. The coplanar waveguide is the device being tested. The probe beam is ideally a few microns in diameter. The optical axis of the $LiTaO_3$ probe is parallel to the z-axis. The orientation of a GaAs probe does not require special attention.

voltage of $1V$. It may be expressed as:

$$E_{z_cpw} = \frac{1}{w} e^{-\left(\frac{n-350}{40}\right)^2} \tag{4.75}$$

where n stands for the number of time steps, *i.e.* 0.01 ps/step, and w is a slot spacing width of the CPW.

All the other parameters used in the FD-TD field simulation are listed in Table 4.1. Referring to Figure 4.15 again, the CPW considered has a center-metal strip width of $s = 15\mu$m, a slot spacing width of $w = 10\mu$m, and is deposited on a 500 μm GaAs substrate. S-parameters are defined at reference planes, as shown in Figure 4.16, which are 257.5 μm, *i.e.* 51.5 meshes, respectively before and after the leading and rear edges of the probe. Note that if the field disturbance which produces a reflection on a perfect CPW is localized, the field propagation mode returns to quasi-TEM mode at the reference planes far from the disturbed region after experiencing disturbances. Therefore, if reference planes are established far away from the disturbance, S-parameters of the network can be defined. Figure 4.17 shows numerical experiment results at input reference plane when the $LiTaO_3$ probe distance is 5 μm. It is confirmed that field disturbances from the probe are negligible outside of these two reference planes. In other words, the quasi-TEM mode is recovered, *i.e.* E_x=0, at reference planes. Consequently, S-parameters can be defined for the network within the reference planes. The effect of a probe placed near the CPW is considered for a number of different distances from the probe face to the CPW surface, defined as the ***probe distances***, starting from 0 μm

(contact) to 20 μm in 5 μm steps. The probe invasiveness can then be inferred from the departure of the CPW S-parameters from the case in which there is no probe. Note that the effects of the transmission line sections separating the E-O probe and the reference planes are included in the S-parameters. Comparisons of $LiTaO_3$ and GaAs probes are made under the same conditions. In addition, these effects, mainly dispersive, are not significant for the frequency range of interest because of the dimensions of the transmission lines.

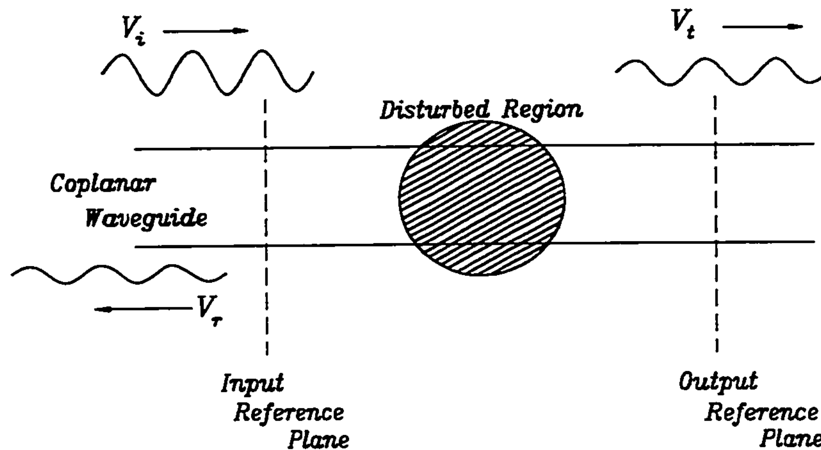

Figure 4.16: Reflected and transmitted signals by field disturbances during probing. The input and output reference planes are chosen far enough from the invaded region so that the field propagation mode returns to quasi-TEM on the CPW at these planes.

For the analysis, the incident voltage wave is defined at input reference plane, yet its propagation is simulated and the associated temporal waveform is

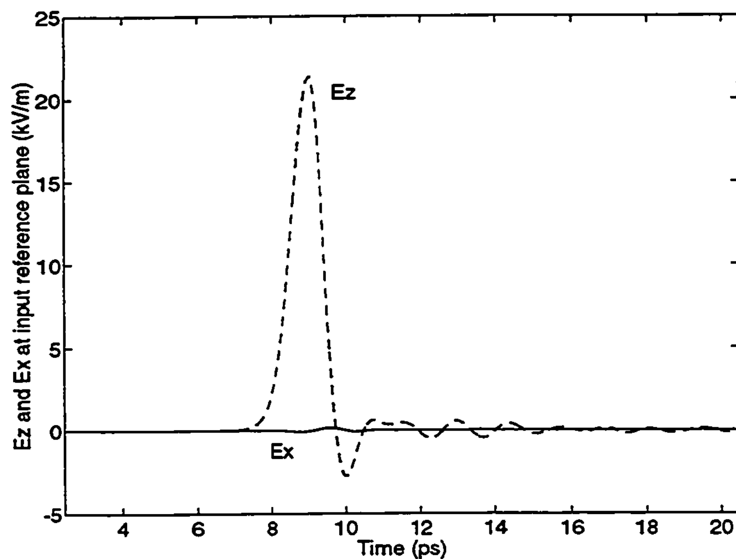

Figure 4.17: Longitudinal component E_x of the electric field on the CPW at the input reference plane. For an ideal TEM-mode, E_x=0. Compared to the magnitude of the dominant component E_z, E_x at the reference plane is 150 times lower, which is negligibly small. The same phenomenon can be observed at the output reference plane. The reference planes are valid.

calculated at both input and output reference planes (see Figure 4.16). Simulation continues until a reflected wave returns to the input reference plane and a transmitted wave passes through the output reference plane. Specifically, a TEM mode (*i.e.* no E_x component) Gaussian impulse with a 0.6 ps full width at half maximum is initialized well back from the input reference plane and allowed to develop into a steady state impulse to define the incident voltage wave $V_i(t)$ (See Figure 4.16). When a probe is introduced, the simulated voltage at the reference plane is the sum of the incident voltage wave and a reflected voltage wave $V_r(t)$ component (See Figure 4.16) which is produced according to the degree of the probing invasiveness.

The simulation parameters are listed in Table 4.1. The dielectric constants for $LiTaO_3$ and GaAs are taken from [1]. Basically, a volume approximately 1000 by 1000 by 100 microns in respective x, y, and z directions, centered on the CPW center conductor directly below the center point of the probe face, is divided into cubes by a 6×5×5 micron *mesh*. Maxwell's equations are solved at all the cube faces for 10 femtosecond increments of time. The probe and other CPW dimensions within this volume are approximated by a stacked staircase of square layers.

4.2.2 Optical signal calculation

As discussed in Chapter 2 and 3, the optical signal of the sampling system is fully determined by the change in birefringence, which is retardance Γ, generated in the E-O probe. By means of electric-optic tensor of the probe material, therefore, Γ is

Center strip width s (μm)	15.0
Slot spacing width w (μm)	10.0
Optical tip width w_1 (μm)	200.0
Optical tip thickness h_2 (μm)	20.0
Substrate thickness h (μm)	500.0
Substrate dielectric constant ϵ_{r1}	13.2
$LiTaO_3$ probe tip dielectric constant ϵ_{r2}	43.0
GaAs probe tip dielectric constant ϵ_{r2}	13.2
Probe supporter dielectric constant ϵ_{r3}	4.5
Space step dx (μm)	6.0
Space step dy (μm)	5.0
Space step dz (μm)	5.0
Time step dt (ps)	0.01
Mesh number in x-direction n_1	188
Mesh number in y-direction n_2	184
Mesh number in z-direction n_3	20

Table 4.1: Parameters in FD-TD analysis

a function of the three dimensional electric field which penetrates the probe crystal as shown in (3.71). For the sake of convenience, both Figure 3.13 and equation (3.71) are copied to here as follows.

$$\Gamma(E_x, E_y, E_z) = d\varphi_c + \sum_{i=i1}^{i2} \frac{4\pi}{\lambda} \left[n_{z_i'}(E_x, E_y, E_z) - n_{x_i'}(E_x, E_y, E_z) \right] \Delta y_i \tag{4.76}$$

where Γ is in radians, Δy_i is the y-axis mesh size at ith node, and $i1$ and $i2$ are mesh indices used in the FD-TD analysis to define the probing light path in the probe tip as shown in Figure 4.18.

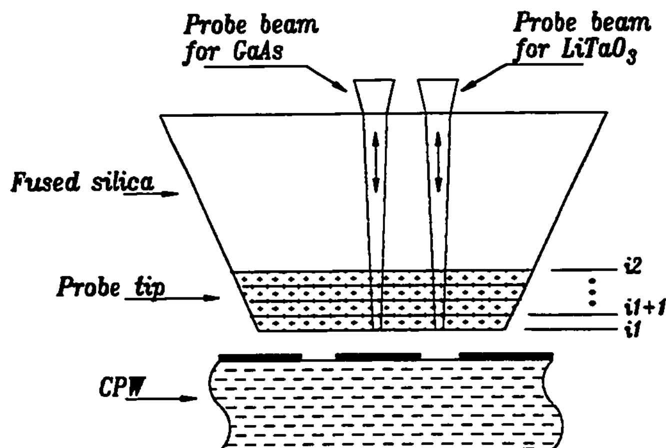

Figure 4.18: Cross-sectional view of external electro-optic probe and coplanar waveguide. Different sampling-beam positions within the probe tip are shown respectively for $LiTaO_3$ and GaAs probes. The sampling-beams intercept the electric field at mesh nodes $i1, i1+1, \cdots, i2$.

Given the parameters listed in Table 4.1, there would be four meshes in

y-direction within the probe tip. In other words, $i2 - i1 = 4$. Therefore, in the simulation of the given example, the sampling beam intercept the electric field twice at these 4 meshes when it travels down to the probe tip and reflects back from the tip facet.

As mentioned previously, all the field components in three dimensions are taken into account in the E-O response calculation. Hence, the impact of the field discontinuities is fully reflected in the simulation as the normalized optical signal is calculated according to equation 3.72.

4.3 Invasiveness

Figure 4.19 shows the field distribution of E_z, which is the dominant component of the electric field on the CPW, $10\mu m$ above the CPW without (a) and with (b) probe at 9 ps after the pulse is launched. This is the time when the pulse peak reaches the probe center. The probe distance is 10 μm. The pulse propagates in x-direction. The field disturbances, as seen in Figure 4.19, are attributed to the probing discontinuity, dispersive effects and surface waves on the CPW and just above its ground plane. Two peaks in Figure 4.19(b) occur exactly at the probe edges The surface waves observed in Figure 4.19 imply that the close placement of probes may produce significant crosstalk between adjacent devices or elements on the circuit board, but the E-O sensitivity increases.

Because of the high dielectric material of the probe and its close placement

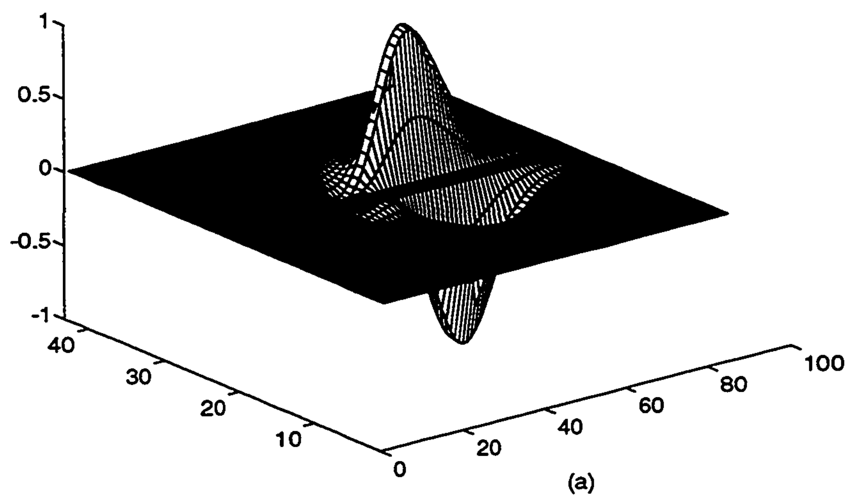

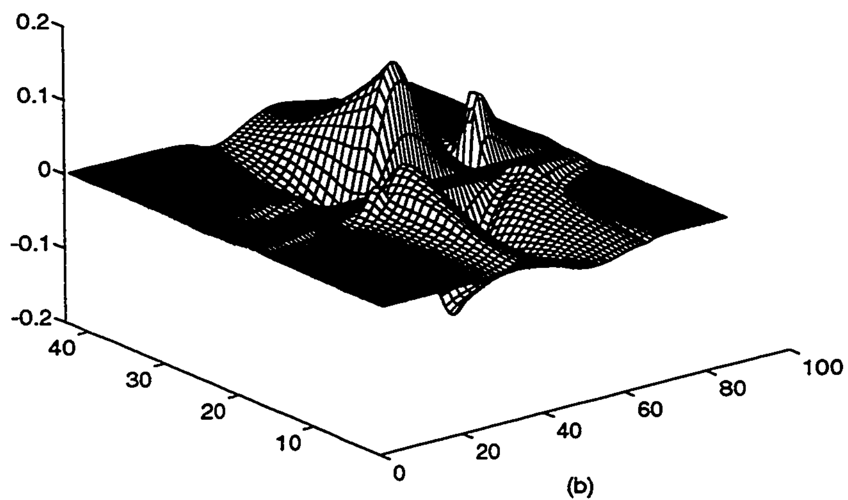

Figure 4.19: The spatial waveform of E_y 10 μm above the CPW at 9 ps. The pulse propagates in z-direction. (a). Without probe. (b). With probe, probe distance=10 μm. The field values are normalized to maximum value without probe.

above the CPW, disturbances of the quasi-TEM mode on CPW are expected. Conceptually, the quasi-TEM wave is confined in the CPW substrate and its wavefront exhibits no noticeable bending in an ideal case as shown in Figure 4.20. When the wavefront goes through the probe, some field energy is extracted towards the high dielectric material, *i.e.* the optical probe tip. As is well known, the speed of the electro-magnetic wave is lower in a higher dielectric material. This difference in speed results in refraction in wave propagation. Figure 4.20 conceptually illustrates this phenomenon that the wavefront is bending due to the slower speed in the probe tip. Thus, E_x in the probe tip becomes significant while the original dominant component E_z decreases as a consequence. The quasi-TEM mode is, therefore, disturbed in the probe where the field is sampled.

Figure 4.21 shows the fields in the center of the optical probe tip when the probe distance is 5 μm. It confirms the above conceptual analysis that the longitudinal component E_x becomes even larger than previous dominant one E_z in the probe when the probe is placed above the CPW. This can be clearly seen by comparing E_x in Figure 4.21(a) and (b). It is also expected from Figure 4.20 that E_y is smaller in magnitude in the probe than the original E_y without probe. This is attributed to the wave front bending caused by refraction of the probe tip. Referring to Table 4.2 and Figure 4.21, while distorted in the presence of the probe, the quasi-TEM mode is obviously valid when there is no probe.

Figure 4.22 gives field results at the position of the probe leading edge with and without the probe. On the one hand, the quasi-TEM mode is well valid

without the probe (See Figure 4.22(b) and also refer to the ratio of E_z and E_x in Table 4.2). On the other hand, the longitudinal component E_x becomes larger as expected, but still smaller than E_z. This can be explained from Figure 4.20 as well. At the probe leading edge, E_x is smaller than its value at the probe center due to the less bending. Consequently, E_z is still the dominant component in three components of the electric field.

Notice that there are significant waveform differences in the field waveforms at both the probe leading edge and its center. Distortion phenomena will be discussed in detail in Chapter 5. In both conceptual analysis and numerical simulation, it has been confirmed that the field in the probe tip is distorted. In other words, the quasi-TEM mode is no longer held at the placement position of the probe when it is suspended over the CPW. This should be accounted for in the E-O response calculation.

Figure 4.23 and Figure 4.24 show three components of the electric field on the CPW right under the probe center and its leading edge when the probe distance is 5 μm. First, the quasi-TEM mode is still valid on the CPW for the 5 μm and larger probe distance although the longitudinal component E_x increases by 2~3.4 times (See Table 4.2). However, the field distribution is changed significantly. Comparing the cases with and without the probe, the vertical transverse component E_y increases by factor of ~15.5 in the presence of the probe. It indicates that part of the field energy confined in the CPW is extracted out towards the probe facet due to the high dielectric probe tip. More importantly, long trail

ringings occur for both E_y, and E_z which is the dominant component on the CPW. Referring to Figure 4.21 and Figure 4.22 again, it is obvious that they are primarily attributed to the ringing in the probe caused by the multiple reflection between the probe leading and rear edges. The ringing in the probe has been observed experimentally [7]. The impact on the device operation is evaluated and observed for the first time in the full wave time domain modeling.

E-Field	in_tip center	in_tip center no_prb	in_tip edg	in_tip edg no_prb	on_cpw center	on_cpw center no_prb	on_cpw edg	on_cpw edg no_prb
E_x	1.0610	0.0047	0.4296	0.0050	0.1469	0.0438	0.0913	0.0497
E_y	0.1648	1.6136	0.2014	1.6480	4.3314	0.2837	4.4825	0.2874
E_z	0.7458	3.2749	0.6829	3.3691	21.3472	22.5086	22.7484	23.2248
E_z/E_x	0.703	696.8	1.590	673.8	145.3	513.9	249.2	467.3

Table 4.2: Peak values of the electric field components

The invasiveness of the external E-O sampling can also viewed as a capacitive loading effect [5]. It produces a propagation delay for a pulse transmission proved by both published experiment results and the simulation results as shown in Figure 4.79. It shows a delay of as much as 1.8 ps in an extreme case when the $LiTaO_3$ probe is in contact with the CPW. This suggests that the delay, noted as δt, suffered due to the capacitive effect cannot be longer than 1.8 ps in any case, which may be associated with a frequency f_{limit}

$$f_{limit} = \frac{1}{\delta t}$$

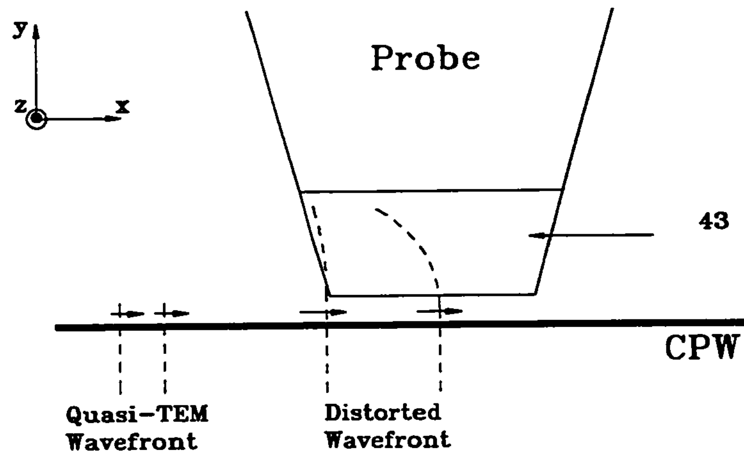

Figure 4.20: Conceptual illustration of the field distortion due to the probing. A refraction phenomenon is observed in the optical probe tip due to the slower wave speed in the higher dielectric material.

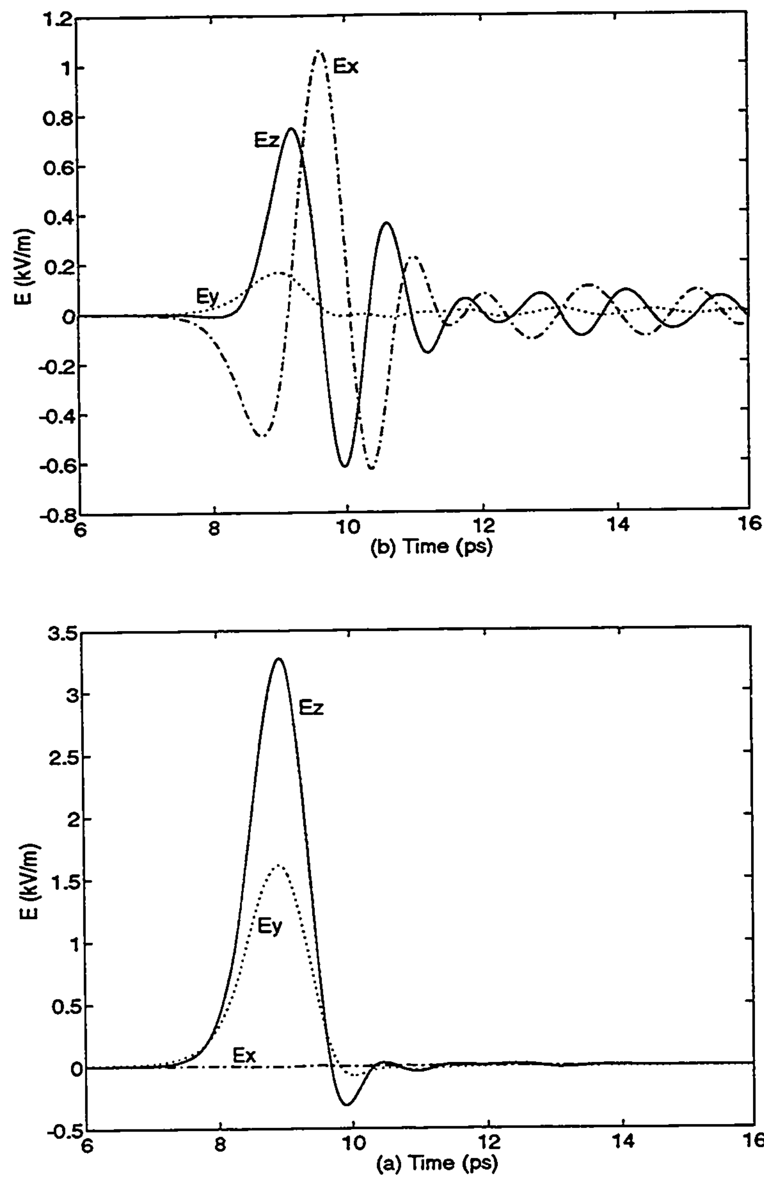

Figure 4.21: Comparison of the electric fields with and without the probe at the position of the probe tip center. The longitudinal component E_x is larger than the original dominant one E_z in the presence of the probe. The quasi-TEM mode is distorted in the probe tip where the electric field is sampled.

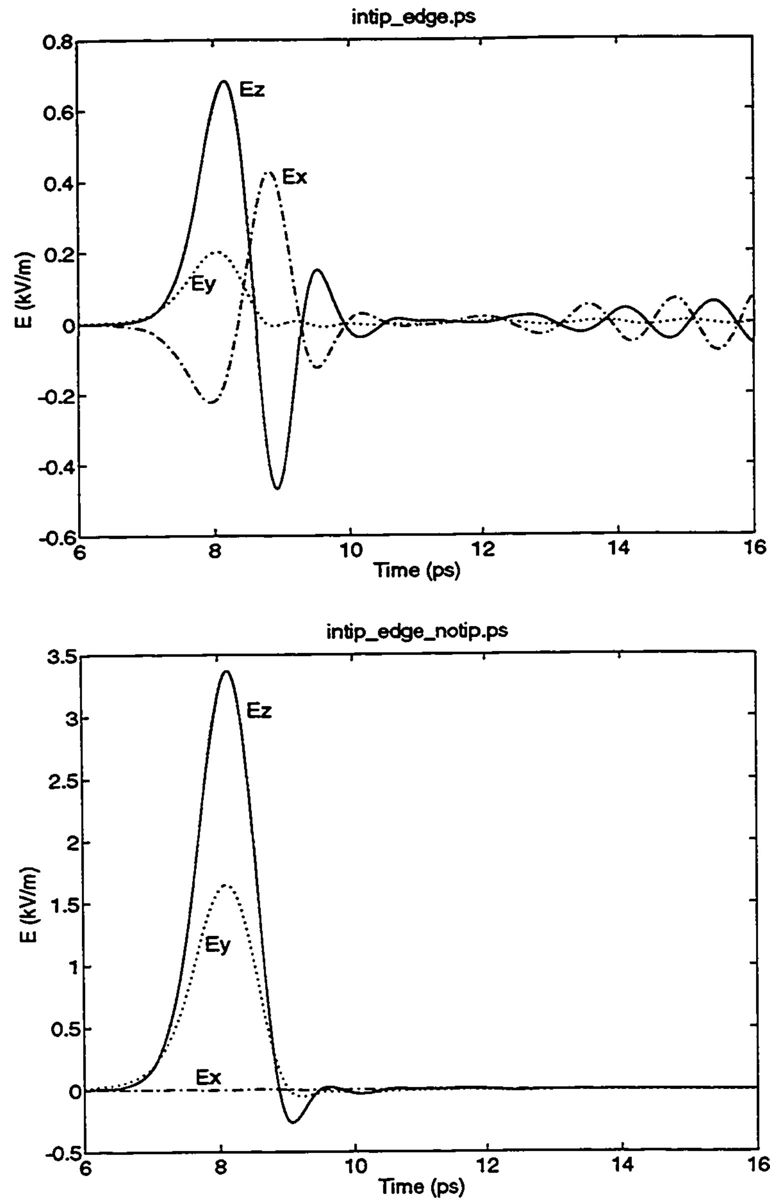

Figure 4.22: Comparison of the field with and without the probe at the position of the probe edge. The longitudinal component E_x is getting larger, but still smaller than E_z. The long trail ringings are observed.

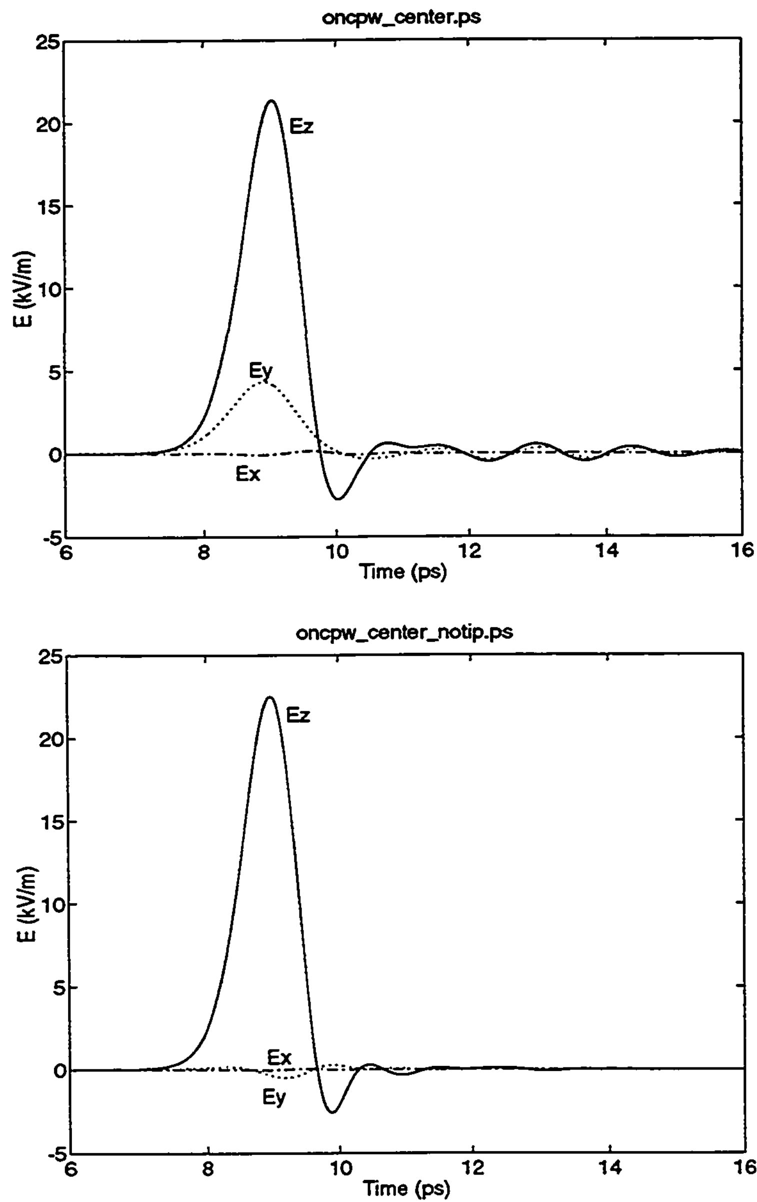

Figure 4.23: Comparison of the field on the CPW with and without the probe right under the center of the probe. The quasi-TEM mode is still valid while the field distribution is distorted significantly. The long trailing ringings are observed.

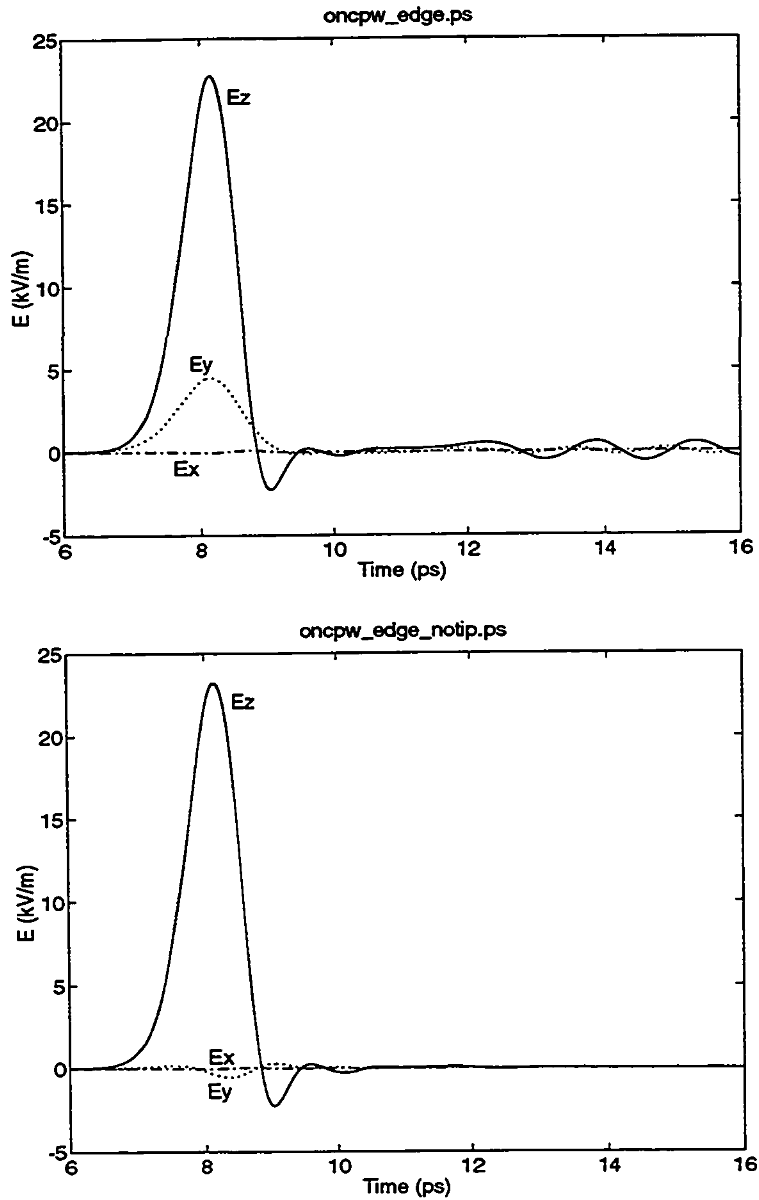

Figure 4.24: Comparison of the field on the CPW with and without the probe right under the leading edge of the probe. The quasi-TEM mode is still held. However, the field distribution is changed in terms of the vertical transverse component E_y and the long trailing ringings.

$$\approx \; 550 \; (GHz) \tag{4.77}$$

It may imply that frequency components higher than this f_{limit} could get serious delay in transmission.

Another way to look at this problem is to find an equivalent capacitor which can approximately introduce 1.8 ps delay in the same situation. As well known, the wave impedance in free space η_0 [23] is

$$\begin{aligned} \eta_0 &= \sqrt{\frac{\mu_0}{\epsilon_0}} \\ &= 377 \; \Omega \end{aligned} \tag{4.78}$$

If a simple RC equivalent circuit is used for a delay $\delta t = 1.8ps$, then,

$$\delta t = \eta_0 C_{load} \tag{4.79}$$

Thus,

$$\begin{aligned} C_{load} &= \frac{\delta t}{\eta_0} \\ &\approx 4.7 \; (femtofarad) \end{aligned} \tag{4.80}$$

This result is in a good agreement with previous experiment observation [17] from which the capacitive loading was reported to be on the order of 10 femtofarads.

In conclusion, the invasiveness is found to be obvious and CPW quasi-TEM mode disturbed by the close placement of the external probe. The invasiveness comparison of the $LiTaO_3$ and GaAs probes in external electro-optic sampling will be reported in the following sections.

4.4 Invasiveness of $LiTaO_3$ and GaAs probes

E-O probe invasiveness to the operation of the device being tested can be evaluated in terms of the device scattering parameters. In this thesis, a CPW is taken as an example of the device being tested as shown in Figure 4.15, which is treated as perfectly matched when no probe is placed above it. S-parameters of the CPW extracted from the field simulation serve to quantitatively describe invasiveness induced by external probing. The comparisons are made referring to the departure of the CPW S-parameters from the case in which there is no probe.

Figure 4.25 shows the magnitude of S_{11} of the CPW with $LiTaO_3$ and GaAs probes, respectively. The $LiTaO_3$ probe produces significant invasiveness, S_{11} being larger than -10 dB for frequencies above 30 GHz when the probe is in contact with the CPW. For identical conditions, the GaAs probe exhibits an S_{11} which is at least 8 dB smaller for frequencies up to 50 GHz and 5.5 dB smaller at 100 GHz. The small invasiveness of GaAs probes is due to its lower dielectric constant of 13, as compared to 43 for $LiTaO_3$. To lend credibility to these results, a simple Touchstone simulation of S_{11} is performed for the case of a 50 ohm transmission line

with a 200 μm discontinuity, the impedance of which is easily calculated as that of a CPW embedded between two dielectrics, *i.e.* $LiTaO_3$ and GaAs. Results of this simple simulation for GaAs and $LiTaO_3$ are consistently between 1 and 2 dB above that of the FD-TD simulation for the respective materials at zero probe distance. It is speculated that the FD-TD simulation anticipates smaller reflections due to a finite probe tip thickness (20 μm) and an impedance transition region near the probe edges. On the other hand, the simple treatment in Touchstone simulation considers probe tip thickness as infinitive. Furthermore, in this simple treatment, there is no transition region from the ideal CPWs to the disturbed field near the probe edges. Consequently, it produces errors to a certain degree.

For probe distances less than 5 μm, it is observed that invasiveness increases dramatically as the probe approaches the CPW. This can be seen in Figure 4.26, where the magnitude of S_{11} at 55.6 GHz versus the probe distance is plotted. The points are connected arbitrarily with a hyperbolic fit, but it is clear that a S_{11} of less than -20 dB can be ensured for probe distances of approximately 1.8 μm for $LiTaO_3$ and 1.0 μm for GaAs. This prediction is compatible with Nagatsuma *et al.* [35], though their study involved a different probe, different measured device structures, and use of a quasi-static field analysis based on a TEM-mode assumption [35]. When the probe spans the entire CPW, results presented may be generally stated that probe invasiveness becomes almost negligible, with a magnitude of S_{11} smaller than -40 dB, when suspended above a CPW by the distance of center conductor width of the CPW.

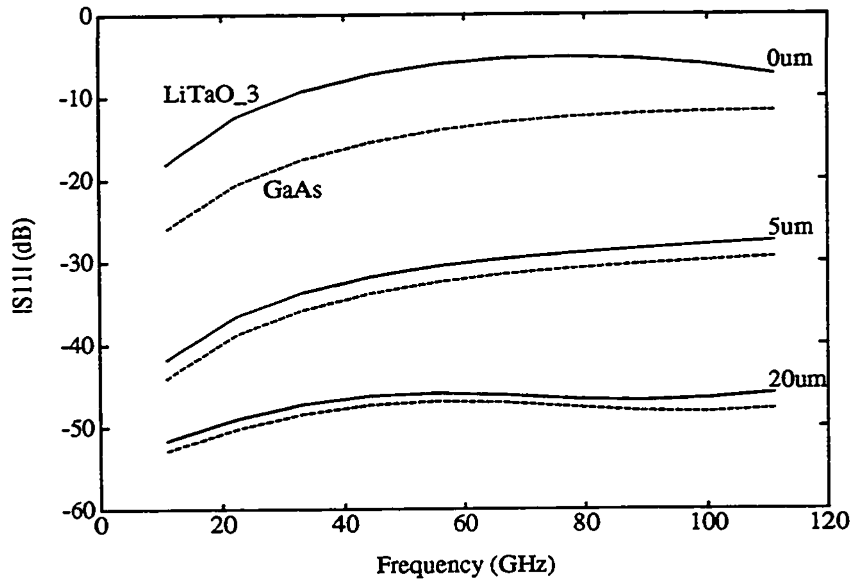

Figure 4.25: Magnitude of reflection coefficient S_{11} (dB) of the CPW for different probe distances: 0 μm, 5 μm and 20 μm.

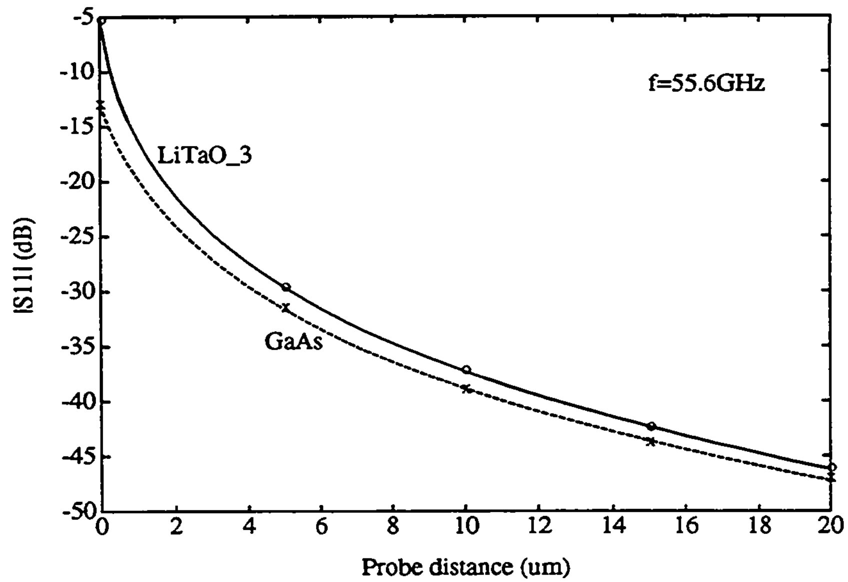

Figure 4.26: Magnitudes of S_{11} (at 55.6 GHz) of the CPW with $LiTaO_3$ and GaAs probes *vs.* probe distance. Hyperbolic curves are fitted.

Figure 4.27 compares S_{21} of the CPW for three cases: a $LiTaO_3$ probe in contact with the CPW; a GaAs probe in contact with the CPW; and no probe. The respective GaAs probe loss and phase shift of less than 0.2 dB and 13 degrees up to 55 GHz are small relative to the more than 1 dB loss and 30 degrees phase shift observed above 50 GHz for the $LiTaO_3$ probe. Extending analysis to cases where the probes are suspended above the CPW plane from 5 μm to 20 μm in 5 μm steps, almost negligible effects are found even for the case of 5 μm. This is a small distance compared even to the dimensions of the CPW.

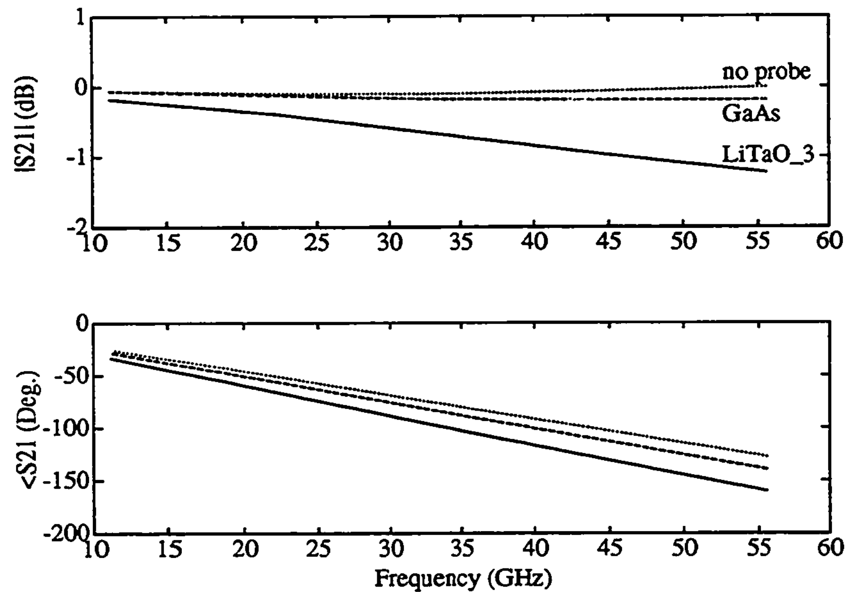

Figure 4.27: Transmission coefficient S_{21} of the CPW without probe and with probes in contact.

Figure 4.28(a) superposes the time domain pulse fields for the same three cases used in Figure 4.27. While the delay caused by GaAs probes, relative to the

unprobed case, is less than 0.6 ps, 1.8 ps of delay appears for the $LiTaO_3$ probe, which corresponds to the 30 degree phase shift at 55 GHz (see Figure 4.27). Figure 4.28(b) shows the same superposed fields for a probe distance of 5 μm, exhibiting temporal delays of less than 0.10 ps and 0.15 ps for GaAs and $LiTaO_3$ probes, respectively. This result qualitatively agrees with Shinagawa *et al.* [2], where no noticeable delay was observed when a GaAs probe was placed 3 μm above a CPW. The difference among the peak values of the three pulses, though very small, hints at different dispersion effects. In the case of contact with the CPW, GaAs probes, which have the same dielectric constant as the substrate, are expected to be less dispersive given a fixed geometry.

It is also necessary to examine the optical signal for invasiveness. When the probe is in contact with the CPW, the electric field associated with the signal threads almost completely into the crystal. When the probe is placed a finite distance from the CPW, most of the field is confined to the air gap due to the high dielectric constant of the crystal. As the probe approaches the CPW, a rapid increase in the optical signal is expected, as is confirmed in the numerical results shown in Figure 4.29. First, the waveform of the normalized optical signal is calculated by equation (3.72) for each probe distance. Then, the peak values of the waveforms are measured to show the trend of the optical signal strength against the probe distances. More data are necessary between 5 μm and 0 μm to accurately interpolate the trend in this region where the sharp change occurs, but this was precluded by computational limitations. Compared to Shinagawa's result for

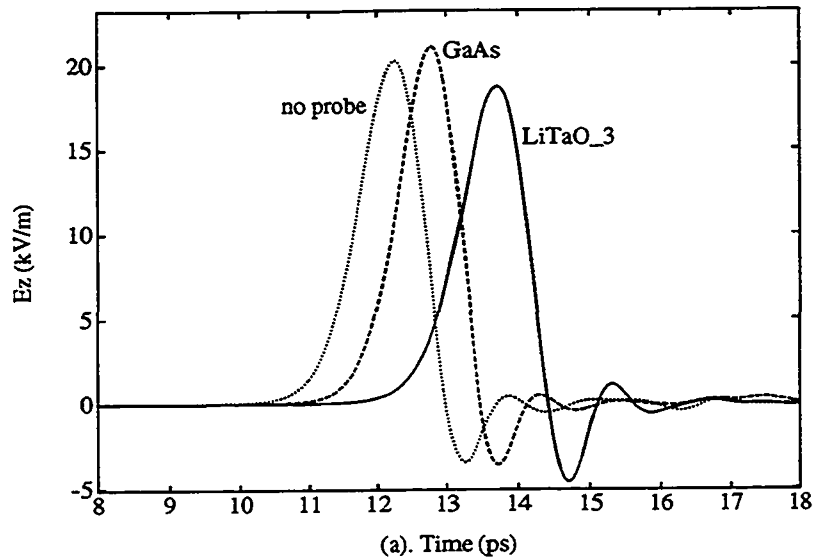

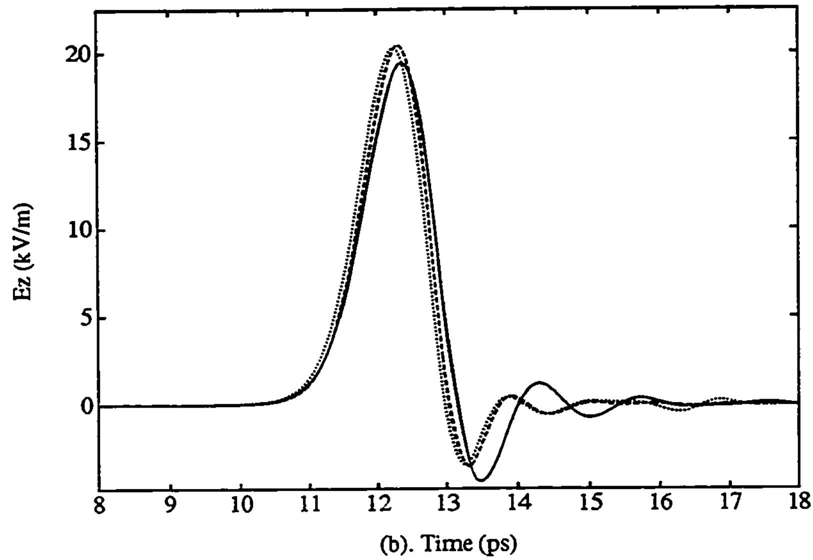

Figure 4.28: E_z waveforms on the CPW at the output reference plane, 258 μm after the trailing edge of the probe. (**a**). Probes in contact with the CPW. (**b**). Probe distance of 5 μm. $LiTaO_3$: solid line. GaAs: dashed line. No probe: dotted line.

a GaAs probe [2] and Valdmanis's for a $LiTaO_3$ probe [52], the results presented in this chapter basically agree with the experimental data, but a convincing comparison will necessitate a detailed simulation that corresponds to their configuration. It can be seen from Figure 4.29 that the optical signal generated in the $LiTaO_3$ probe is approximately 3 dB higher than that in the GaAs probe for probe distances greater than 3 μm. The optical signal shown in this figure is normalized to the signal intensity generated when the $LiTaO_3$ probe is in contact with the CPW, and same wavelength is assumed to be used for both probes. However, typical wavelengths of probing beams for $LiTaO_3$ and GaAs differ, being respectively in the long visible (*e.g.* 0.6 μm) and near infrared (*e.g.* 1.3 μm) regions [5]. In this case, the optical signal amplitude generated in $LiTaO_3$ is approximately 4 times larger, or 6 dB higher than that for GaAs since a fixed birefringence manifests an optical signal which is inversely proportional to wavelength, referring to equation (3.71). For probe distances smaller than 3 μm, the relative response of $LiTaO_3$ increases to about 5 times that of GaAs at a given wavelength. At distances larger than 3 μm, the optical signal does not decrease substantially when the probe is moved away from the CPW. This agrees qualitatively with Heutmaker's measured results (See Figure 1 in [3]).

As mentioned previously, E_x and E_y are comparable to E_z in magnitude. All three field components, therefore, have been considered in the optical signal calculations. The results, however, show that there is no noticeable difference when E_x and E_y are ignored. This confirms and justifies the conventional assumptions

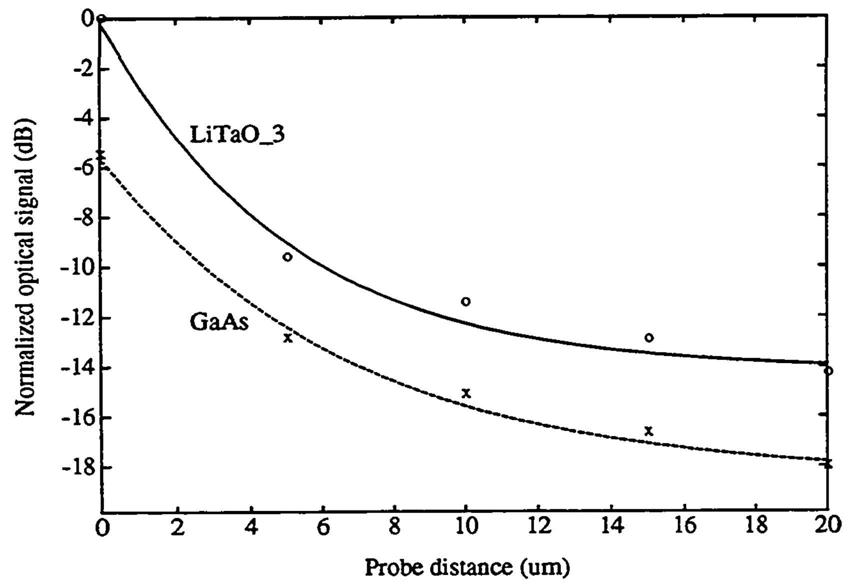

Figure 4.29: Peak value of the normalized optical signal generated in $LiTaO_3$ and GaAs probes *vs.* probe distance. Symbols denote the simulation points and an exponential curve is fitted. The same wavelength of sampling-beam is applied to both probes.

made in previous research, but with a better understanding. E_x and E_y are not small compared to E_z, but their contribution to the optical signal suffers directional selectivity of the probe in E-O response. Regarding the optical signal calculations, simultaneous interaction between the optical probing beam and the electric field in the crystal has been assumed. For larger probe and transmission line geometries, however, the interaction is related to sampling positions in the probe and time when the sampling-beam intercepts the field.

Figure 4.30 shows the normalized optical signal as a function of invasiveness in terms of the magnitude of S_{11} when the same wavelength is used for probing in both $LiTaO_3$ and GaAs probes. The linear fits to the simulated points are nearly parallel, suggesting that a figure of merit specification can be applied to different birefringent materials. In this case, $LiTaO_3$ produces 3 dB more E-O response for a given invasiveness. As mentioned previously, the optical signal generated in $LiTaO_3$ can even be larger when a shorter wavelength is used. However, GaAs probes must be used at a wavelength above its absorption band. Therefore, $LiTaO_3$ probes are preferred in external E-O sampling for a tolerable value of S_{11}. Crosstalk between devices on the measured integrated circuit is another significant issue in the comparison of these two probes due to the transverse E-O effect in $LiTaO_3$ and the longitudinal E-O effect in GaAs. For other devices which are not as highly symmetrical as a CPW, further investigations on crosstalk are desirable.

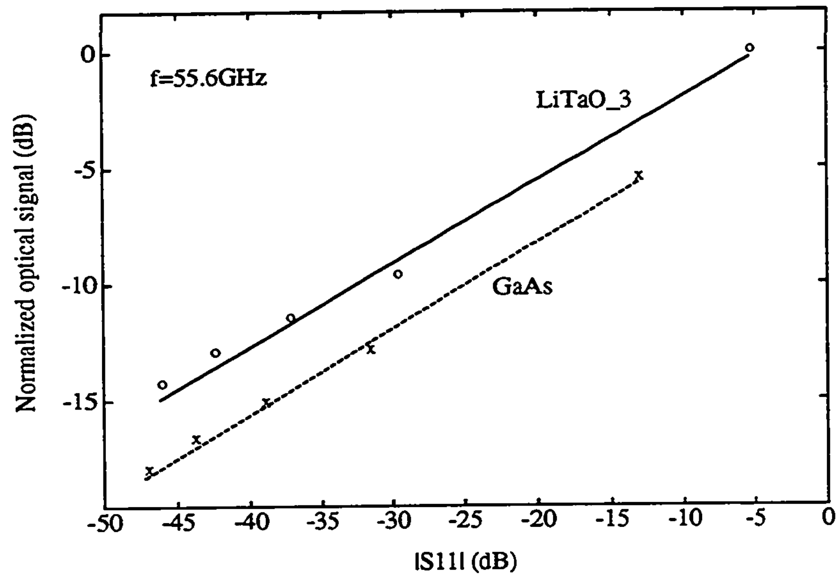

Figure 4.30: Normalized optical signal *vs.* the magnitude of S_{11} at 55.6 GHz. Symbols denote the simulation points. The same wavelength of sampling-beam is applied to both probes.

4.5 Equivalent circuit model of the probe

The invasiveness induced by the optical probe to a coplanar waveguide (CPW) has been investigated in terms of reflection and transmission coefficients [10]. The results of further research have been given in more detail in previous sections. A full-wave time domain field simulation scheme, namely, the finite-difference time-domain (FD-TD) method, is used to generate the time-domain field waveform, which in turn is converted to frequency-domain S-parameters. Quantitative effects of the probe are then reported [9, 10]. Although full-wave electro-magnetic simulation provides accurate results, it is very computationally intensive and prohibitively slow for design purposes. Therefore, there is an increasing need for an efficient, yet accurate model for the external EOS test structure. The equivalent circuit approach for modeling such a structure allows almost real-time computation.

This section reports a new scheme which provides, for the first time, an equivalent circuit model to the optical probe and the CPW. Transmission line models are the key elements in the equivalent circuit consisting of the analytic approximations and lumped circuit elements. Coplanar waveguide line models from [53, 54] are adopted and modified to some degree to suit needs of this research. The model takes into account geometry sizes and material properties of the probe and the CPW so that parameters of the circuit elements are dependent on the actual measurement configuration. Optimization techniques are used to determine parameters of the equivalent circuit model to fit the full-wave field simulation results. Therefore, the circuit model and full wave field simulation are self-consistent.

The model is dependent on the test structure geometry and material parameters. The over-all modeling process is outlined in the following. We demonstrate this new approach by considering the test structure in [9, 10]. The FD-TD simulation results are used to determine the parameter values in the equivalent circuit model. The comparison is given of S-parameters obtained by the FD-TD method and from the equivalent circuit model. Probe invasiveness to the CPW, which is strongly governed by the distance from the probe to the CPW, is predicted by simulating the equivalent circuit with different distances.

4.5.1 Equivalent circuit model

The structure of a CPW with an optical probe under consideration is depicted in Figure 4.31. The equivalent circuit model is based on a partition that divides the entire structure into three segments as shown in Figure 4.31. The first and third are ordinary CPW sections on GaAs substrate (ϵ_{sub}). The center section can be viewed as a multi-layer CPW with three possible layers on top of the ordinary CPW, an air gap, the high dielectric optical probe tip (ϵ_{tip}) and its fused silica supporter (ϵ_{spt}). Note that, along the wave propagation direction in Figure 4.31(a), a rectangular cross-section is used to approximate the truncated square pyramid shape of the actual optical probe. However, along another dimension shown in Figure 4.31(c), the width of the probe, parallel to the width of the CPW, can be assumed as infinite because of the large probe width relative to width of the CPW. The equivalent circuit is proposed in Figure 4.32, which includes the

above mentioned three transmission line sections and two T-type 2-ports. These 2-ports, consisting of lumped elements, are used to characterize the discontinuity at the interfaces, or transition sections, associated with the probe leading and rear edges. Generally speaking, the circuit model is superior to previous analytical transmission line like model for the following reasons:

1. The circuit model is developed fully based on the full wave FD-TD field simulation results;

2. The circuit model has taken into account the discontinuities associated with the probe edges.

Attenuation, dispersion and characteristic impedance of the CPW in E-O sampling.

In the following, the center section with the probe is regarded as the probe section. When the probe is suspended above the CPW, an air layer is inserted between the CPW and the optical tip, through which the field energy is coupled from the CPW to the probe. The degree of this coupling is a function of the distance from the probe to the CPW. This distance defines the thickness of an air layer, denoted by h_{air} thereafter, inserted between the probe and the CPW. As it has been shown in field analysis in previous sections, the high-dielectric probe tip changes the transverse CPW electro-magnetic field distribution by extracting a significant portion of the electric field energy if the probe is directly in contact

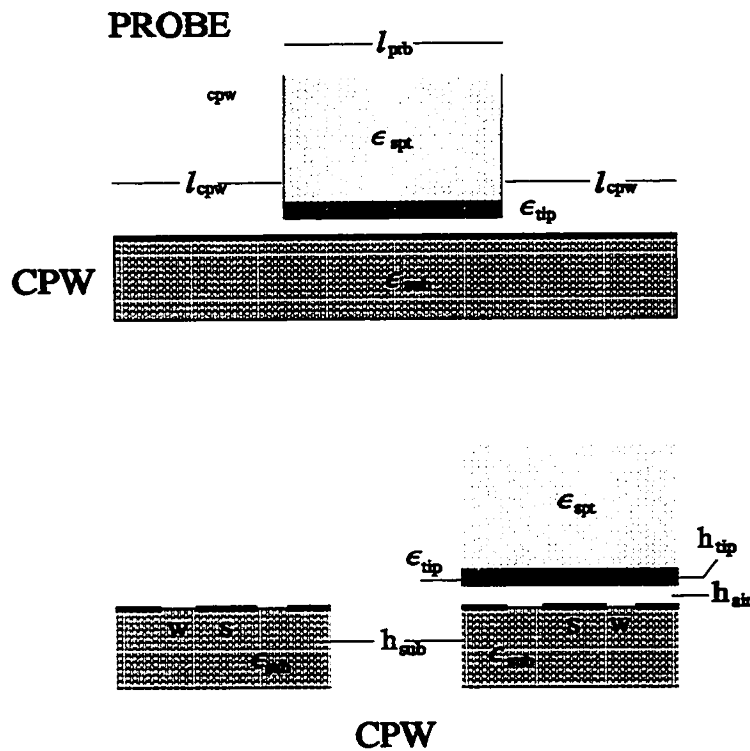

Figure 4.31: Side view and cross-section of the coplanar waveguide with and without probe. (a) Side view of the coplanar waveguide with the optic probe. Two coplanar waveguide sections are denoted by l_{cpw} and the probe section by l_{prb}. (b) Cross-section of the coplanar waveguide. (c) Cross-section of the coplanar waveguide with the probe.

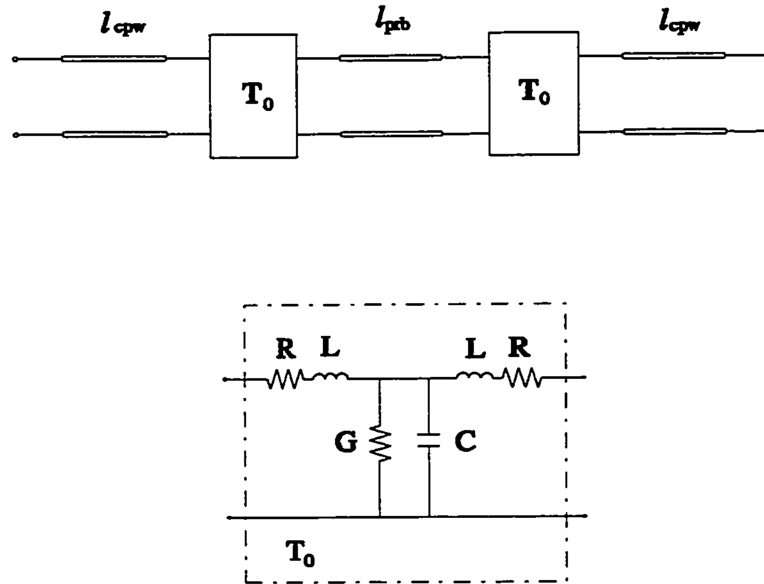

Figure 4.32: Equivalent circuit model for the electro-optic sampling structure. The transmission line models for the coplanar waveguide sections and probe section are labeled respectively by l_{cpw} and l_{prb}. The 2-port, denoted by T_0, is a T-type lumped element circuit detailed in lower block.

with the CPW. When the probe is far away from the CPW, the energy coupling is very weak, which results in less invasiveness, but lower E-O sampling sensitivity. The probe position is the most important parameter in determining the equivalent circuit model.

A CPW section can be fully described by its characteristic impedance, attenuation, and dispersion. The approaches devised in [53, 55] are used. The frequency dependent effective dielectric constant, as a measure of the dispersion of the CPW, is analytically approximated by [53, 55].

$$\sqrt{\epsilon_{eff}(f)} = \sqrt{\epsilon_q} + \frac{\sqrt{\epsilon_r} - \sqrt{\epsilon_q}}{1 + a\left(\frac{f}{f_{TE}}\right)^b} \tag{4.81}$$

The involved parameters are defined and evaluated in detail as follows.

Parameter b has been found to be independent of geometry as a constant ~1.8 [53, 55]. For the CPW section, the quasi-static effective permittivity ϵ_q may take:

$$\epsilon_q = \frac{\epsilon_r + 1}{2} \tag{4.82}$$

for the CPW section without the probe, and for the probe section

$$\epsilon_q = q_1 + q_2\epsilon_{sub} + q_3 + q_4\epsilon_{tip} + q_5\epsilon_{spt} \tag{4.83}$$

where the coefficients $q_1, q_2, ..., q_5$ are filling factors of individual dielectric layers. Each of them respectively associated with air below the CPW substrate, the CPW substrate, air-layer between the CPW substrate and the optical probe, the probe tip and probe supporter.

The probe section of the CPW can be considered as a multi-layer coplanar waveguide as shown in Figure 4.31(c). The coefficients in (4.83) are determined from the following five basic capacitances, which is based on the approach of the modeling of multi-layer CPWs proposed in [54].

$$C_1 = 2\epsilon_0 \frac{K(k_1)}{K'(k_1)} \qquad k_1 = \frac{s}{s+2w} \tag{4.84}$$

$$C_i = 2\epsilon_0 \frac{K(k_i)}{K'(k_i)} \qquad k_i = \frac{\sinh\left(\frac{\pi s}{4h_i}\right)}{\sinh\left(\frac{\pi(s+2w)}{4h_i}\right)} \tag{4.85}$$

$$C_5 = C_1 \tag{4.86}$$

where $i = 2, 3, 4$ and s is the center conductor strip width, w the CPW slot spacing, and

$$h_2 = h_{sub} \tag{4.87}$$

$$h_3 = h_{air} \tag{4.88}$$

$$h_4 = h_{tip} \tag{4.89}$$

The ratio $\frac{K(k)}{K'(k)}$ is given by

$$\frac{K(k)}{K'(k)} = \begin{bmatrix} \frac{1}{\pi}\log\left(2\frac{1+\sqrt{k}}{1-\sqrt{k}}\right) & 0.5 \le k^2 \le 1 \\ \left[\frac{1}{\pi}\log\left(2\frac{1+\sqrt{k}}{1-\sqrt{k}}\right)\right]^{-1} & 0.0 \le k^2 \le 0.5 \end{bmatrix} \tag{4.90}$$

Now, the filling factors are

$$q_1 = \frac{C_1 - C_2}{C_1 + C_5} \tag{4.91}$$

$$q_2 = \frac{C_2}{C_1 + C_5} \tag{4.92}$$

$$q_3 = \frac{C_3}{C_1 + C_5} \tag{4.93}$$

$$q_4 = \frac{C_4 - C_3}{C_1 + C_5} \tag{4.94}$$

$$q_5 = \frac{C_5 - C_4}{C_1 + C_5} \tag{4.95}$$

Thus, the equations (4.82) and (4.83) are fully determined using (4.91)-(4.95). As a special case of h_{air}=0, *i.e.*, the probe in contact with the CPW, q_3 and C_3 are both set zero. Since the electric field is mostly confined in the region of higher dielectric constant ϵ_r, $q_r = q_{sub}$ both for the CPW sections and for the probe section when the probe is suspended above the CPW, whereas $q_r = q_{tip}$ for the probe section when the probe is in contact with the CPW.

The coefficient a in (4.81), which is geometry dependent and determines the frequency dependency, is given by:

$$\log(a) = a_0 \left[u \log\left(\frac{s}{w}\right) + v \right] \tag{4.96}$$

where u and v are determined by

$$q = \log\left(\frac{s}{d}\right) \tag{4.97}$$

$$u = 0.54 - 0.64q + 0.015q^2 \tag{4.98}$$

$$v = 0.43 - 0.86q + 0.54q^2 \tag{4.99}$$

where d=h_{tip} for the probe section when the probe is in contact with the CPW or d=h_{sub} for other cases. A definite relation between a and the CPW geometry is

not given in [53, 55]. Therefore, a parameter a_0 has been introduced as a fitting coefficient in (4.96). The fitting coefficient is referred to as the parameters which are determined by optimization techniques.

The surface wave TE_1 mode cutoff frequency is defined as [53]

$$f_{TE} = \frac{c}{4d\sqrt{\epsilon_r - 1}} \tag{4.100}$$

where c is the speed of light in vacuum.

The frequency-dependent propagation constant β(f) is given in [55] as

$$\beta(f) = 2\pi \frac{f}{c}\sqrt{\epsilon_{eff}(f)} \tag{4.101}$$

and the frequency-dependent attenuation α(f) by [53] as

$$\alpha(f) = 2\left(\frac{\pi}{2}\right)^5 \frac{\left(1 - \frac{\epsilon_{eff}(f)}{\epsilon_r}\right)^2}{\sqrt{\epsilon_{eff}(f)}} \frac{\epsilon_r^2 (s+2w)^2}{c^3 K'(k) K(k)} \tag{4.102}$$

where K(k) is the complete elliptic integral of the first kind and

$$K'(k) = K(\sqrt{1-k^2}) \tag{4.103}$$

$$k = \frac{s}{s+2w} \tag{4.104}$$

The characteristic impedance is [53]

$$Z(f) = \frac{120\pi}{\sqrt{\epsilon_{eff}(f)}} \frac{K'(k)}{4K(k)} \tag{4.105}$$

Lumped elements for discontinuities

When the optical probe is placed at different distances from the CPW, characteristics of the probe section vary. Since different probe distances would also introduce different degrees of discontinuity into the structure, the parameters in the T-type 2-ports should be changed accordingly. To include this effect, values of the lumped elements are defined to be distance-dependent:

$$R = \frac{R_0}{1+\gamma_r h_{air}} \tag{4.106}$$

$$L = \frac{L_0}{1+\gamma_l h_{air}} \tag{4.107}$$

$$C = \frac{C_0}{1+\gamma_c h_{air}} \tag{4.108}$$

$$G = \frac{G_0}{1+\gamma_g h_{air}} \tag{4.109}$$

where γ's are fitting coefficients as function of the probe distance. The maximal value of each lumped element corresponds to the case where $h_{air}=0$, *i.e.*, when the strongest discontinuity is introduced. Discontinuities vanish when the probe is moved far away from the CPW.

Matrix description of equivalent circuit model

In order to derive the expression of the equivalent circuit model, the ABCD-matrix form is used because of the series structure of three transmission line 2-ports and two lumped element T-type 2-ports (Refer to Figure 4.32). The ABCD matrix for

transmission lines is

$$T_k = \begin{bmatrix} \cosh[(\alpha_k + j\beta_k)\ell_k] & Z_k \sinh[(\alpha_k + j\beta_k)\ell_k] \\ \frac{1}{Z_k} \sinh[(\alpha_k + j\beta_k)\ell_k] & \cosh[(\alpha_k + j\beta_k)\ell_k] \end{bmatrix} \tag{4.110}$$

where subscripts k=cpw or k=prb, standing for the CPW section and the probe section respectively; ℓ is the length of the section and the ABCD-matrix at frequency f for the T-type 2-port is

$$T_0 = \begin{bmatrix} 1 + ZY & Z(2 + ZY) \\ Y & 1 + ZY \end{bmatrix} \tag{4.111}$$

where Y=G+$j2\pi f$C is the shunt branch admittance and Z=R+$j2\pi f$L the series branch impedance. The over-all ABCD-matrix is, then, simply the multiplication of five 2-port ABCD-matrices as:

$$T = T_{cpw} T_0 T_{prb} T_0 T_{cpw} \tag{4.112}$$

Now the S-parameter matrix can be readily obtained by converting the above ABCD-matrix.

4.5.2 Modeling procedure and results

The complete modeling procedure is summarized in Figure 4.33. The FD-TD field simulation is carried out according to the given probe and sampling structure design as described in Chapter 3. The frequency-domain information, S-parameters, is obtained from time domain field response by Fourier transformation [9, 10]. In

this specific circuit modeling, four FD-TD simulations are required to compute S-parameters for the following four cases:

1. The CPW without the probe.

2. The CPW response when probe distance is 0 μm.

3. The CPW response when probe distance is 5 μm.

4. The CPW response when probe distance is 10 μm.

where the probe distance is defined in Chapter 3 as the distance between the probe tip facet to the CPW surface.

The actual procedure to determine equivalent circuit parameters contains four optimization processes corresponding to the four cases simulated by the FD-TD method. Optimization tools and parameter extraction features built in Touchstone/Libra of EEsof [56] are used in these processes. In the first optimization, the model of a CPW section without the probe is fitted to identify parameter a_0 in (4.96). The CPW section, denoted by ℓ_{cpw} in Figure 4.32(a), can be characterized by using formulas (4.101)-(4.105). It is found that formulas (4.101)-(4.105) are very accurate, leading to an excellent agreement between the FD-TD results and the results given by (4.101)-(4.105). Then, three optimizations are performed to consider the three different probe distances. For each of the three cases, the ABCD-matrix of the whole configuration is calculated according to (4.112). The values of a_0 and the lumped elements R, L, C and G in (4.106)-(4.109) are determined by

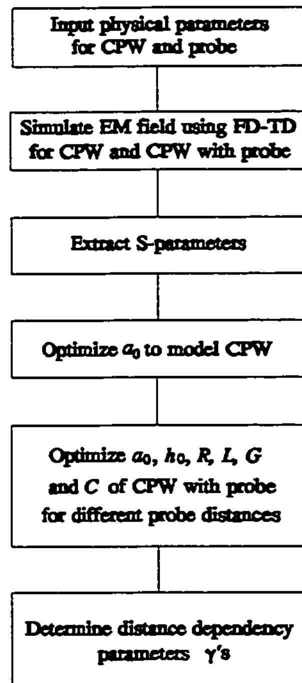

Figure 4.33: Flowchart of the equivalent circuit approach to modeling of the electro-optic probing structure.

matching the S-parameters from the equivalent circuit model to the FD-TD calculation results. The multi-layer dielectric CPW model determined by (4.84)-(4.95) works fairly well for the case when the probe distance is 0μm. In other two cases, however, large discrepancies are found when the formulas in (4.106)-(4.109) are directly used for probe distances of 5 and 10 μm. This is due to the very thin air layer whose thickness is equal to the probe distance, the small probe tip thickness, and the significant difference of dielectric constants of the CPW substrate, air, and the optical probe tip. None of these factors are taken into account when the multi-layer CPW model has been developed in [54]. A comparison between the calculated results presented in this thesis and the results of the CPW circuit model indicates a necessity to introduce a correction factor h_0 to the air layer thickness (*i.e.*, the probe distance) in (4.85) as

$$h'_{air} = h_0 h_{air} \tag{4.113}$$

The correction factors h_0 are respectively determined for these two cases.

From the three sets of obtained α_0 and the lumped elements R,L,C,G values associated with the three different probe distances, the distance dependency parameters, γ's in (4.106)-(4.109), can be found by using a simple curve fitting routine. In addition, the probe distance dependency of a_0 for the probe section can be also found in a similar manner by using a simple expression

$$a_0 = a_{00} + \frac{a_{01}}{1 + \gamma_{a_0} h_{air}} \tag{4.114}$$

and by fitting at three values, which are correspondent to the probe distances 0, 5, and 10 μm. The value of a_0 approaches to a_{00} when h_{air} is sufficiently large. The distance dependency of the correction factor h_0 defined in (4.113) is assumed to be of a very similar form to (4.114) as

$$h_0 = 1 + \frac{h_{01}}{1 + \gamma_{h_0} h_{air}} \tag{4.115}$$

Note that h_0 should approach to 1 when h_{air} is very large. Two available values of h_0 fitting the FD-TD field simulation results for probe distances 5 and 10 μm can be used to uniquely determine h_{01} and h_{air} in (4.115).

Comparisons of S-parameters calculated using the equivalent circuit model and by the FD-TD field simulation are given in Figure 4.34. It can be seen that the equivalent circuit model and the FD-TD calculation results are in a very good agreement. For instance, the maximal difference between two groups of S_{11} for the case of the zero probe distance is about 1dB. The obtained parameters from the optimization procedure, with the physical parameters of the structure, are listed in the Table 4.3. Each of the four optimizations involves a total of 24 error functions, resulted from the magnitude and phase of S_{11} and S_{12} at 6 frequencies ranging approximately from DC to 60 GHz. Touchstone/Libra of EEsof [56] is used and the CPW and probe models are implemented using the feature allowing user-defined elements. Figure 4.35 shows S11 of the CPW with the probe, which is calculated using the equivalent circuit model and seen as function of probe distances of 0.5, 7.5, 1~8 μm.

Center conductor width s	15 μm
Slot spacing width w	10 μm
Probe tip width l_{prb}	200 μm
CPW section length l_{cpw}	258 μm
Substrate thickness h_{sub}	600 μm
Optical tip thickness h_{tip}	10 μm
Air layer thickness h_{air}	0, 5, 10 μm
Substrate dielectric constant ϵ_{sub}	13.2
Probe tip dielectric constant ϵ_{tip}	43.0
Supporter dielectric constant ϵ_{spr}	4.5
a_0 for CPW section	0.0013
R_0 and γ_r	1.31Ω, 2.77/μm
L_0 and γ_l	20 pH, 0.38/μm
C_0 and γ_c	0.4fF, 0.98/μm
G_0 and γ_g	0.88mS, 35.7/μm
a_{00}, a_{01} and γ_{a0}	0.0013, 0.12, 0.46/μm
h_{01} and γ_{h0}	6.84, 0.55/μm

Table 4.3: Parameters of the electro-optic sampling structure and the equivalent circuit model.

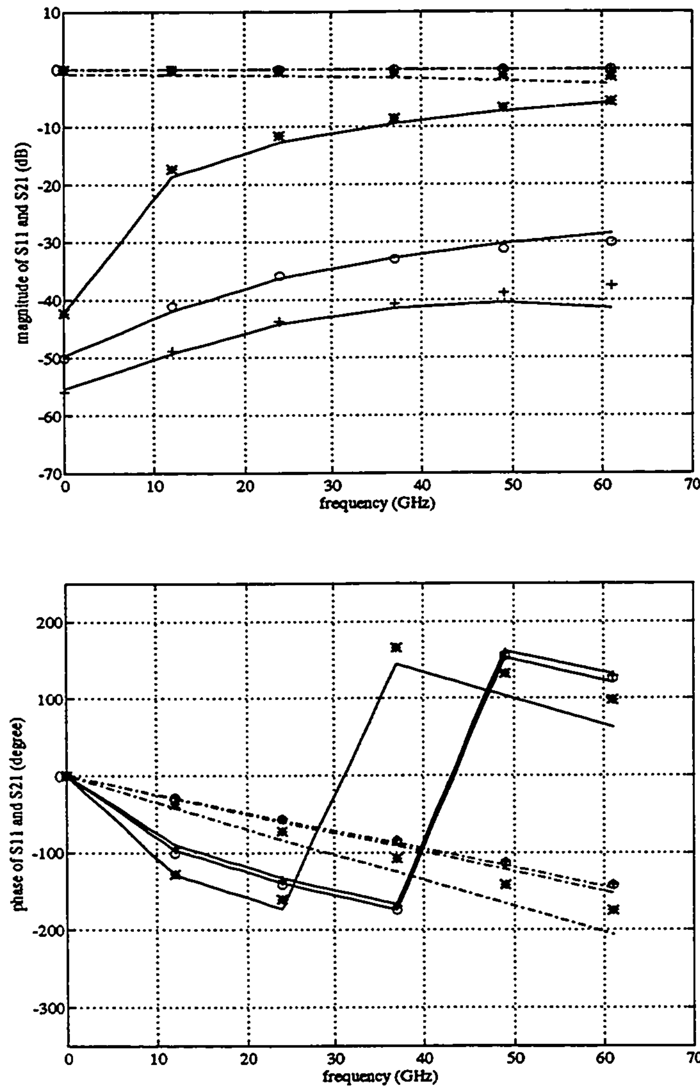

Figure 4.34: S-parameters calculated by the equivalent circuit model and by FD-TD simulation. (a) Magnitude of S11 and S21. (b) Phase of S11 and S21. Solid lines are for S11 and dashed lines for S21 calculated from the circuit model. *, and + are corresponding to S-parameters calculated from FD-TD simulation for hair = 0, 5, and 10fm, respectively.

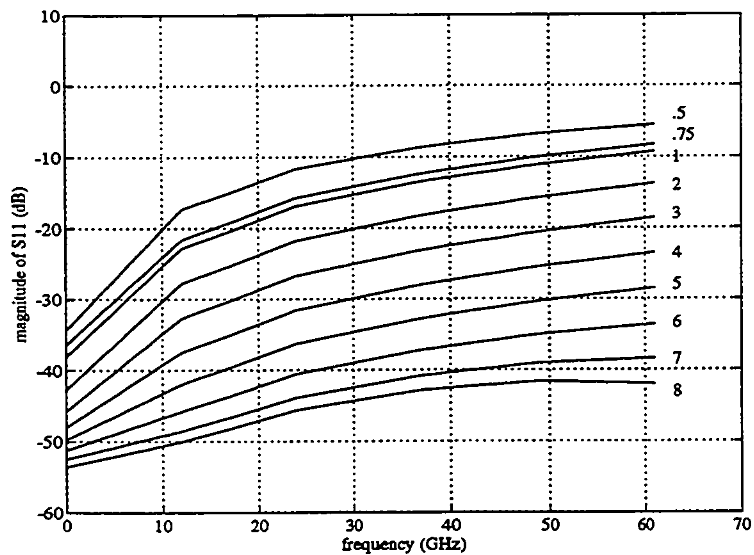

Figure 4.35: Calculated magnitude of S11 for different probe to CPW distances: 0.5, 0.75, 1, 2, 3, 4, 5, 6, 7, and 8 μm.

In conclusion of this section, an equivalent circuit model is developed for the first time for a CPW with the optical probe in external electro-optic sampling system. The model uses the ordinary CPW model, multi-layer dielectric CPW model, and the lumped element 2-port to simulate the effects induced by probing discontinuities. The geometry and the material properties have been taken into consideration in the model. The example has shown that the proposed equivalent circuit model can be very efficient and accurate in characterization of the invasiveness. The model can be used in the future development of fast and accurate calibration techniques in E-O sampling measurements. The presented approach can also be used for other test structures with different probe shapes and CPW geometries.

4.6 Measurements

The invasiveness of the optical probe may be experimentally determined by introducing a second probe on the transmission line between the electrical signal generation and measurement point. The time delay and the amplitude reduction introduced by the second probe are then used for invasiveness characterization. Special attention should be paid to measurement of the reflection magnitude and the transmission phase. They are more sensitive to the probing invasiveness. Note that the effects of unavoidable air-gap are not considered in the field simulations while the measurement implicitly includes their contribution. The air-gap may

substantially contribute to relatively large deviations between measured and simulated results when the probe is in contact with the device being tested [33, 34].

4.7 Conclusions

The invasiveness of $LiTaO_3$ and GaAs probes in the external E-O measurement configuration of Figure 4.15 has been simulated and compared quantitatively using a 0.6 ps Gaussian pulse signal on a coplanar waveguide. Results are based on the FD-TD method, which is used to calculate the full wave time domain field of the coplanar waveguide signal in and around the probe. The magnitude of S_{11} caused by the presence of a probe near the waveguide is taken as a quantitative measure of the probe invasiveness on the measured device. Contact probing with $LiTaO_3$ causes a S_{11} larger than -10 dB above 30 GHz, which is about 8 dB greater than that with GaAs up to 50 GHz. Under identical conditions, respective transmission delays of 1.8 ps and 0.6 ps are observed for $LiTaO_3$ and GaAs probes. Both probes, however, have significantly reduced invasiveness for probe distances larger than 3 μm. For a given wavelength of probing light, the electro-optic response of $LiTaO_3$ probes is twice that of GaAs probes for probe distances larger than 3 μm, and about 5 times more than GaAs on contact. The transparency of $LiTaO_3$ at shorter wavelengths, however, allows even larger responses with respect to GaAs. In conclusion, $LiTaO_3$ probes are generally preferred over GaAs in external electro-optic sampling for a given level of invasiveness. Further research in external probe design and sampling-beam delivery is required to determine the optimal measurement

configuration.

Chapter 5

Distortion of external electro-optic sampling

5.1 Introduction

As described in Chapter 2, field disturbances in external electro-optic sampling caused by the probe may be grouped into two categories. One is the invasiveness (Chapter 4) which is the influence on operation of the device being tested; The other is the distortion which is regarded as the distinctive field response in the optical probe-tip relative to the field response in the device being tested (See Figure 3.14). This chapter will focus on the distortion because it leads to a discrepancy of the field response of electro-optic sampling from the original field in the device being tested.

Field disturbances have been qualitatively observed in some of the previous

experiments [7, 16]. Yet they are defined as distortion for the first time by the research presented in this thesis [9], which is a measure of discrepancy between measured signal by the probe and actual signal in the device being tested.

In [7], a long, ringing tail in a E-O response to an electrical Gaussian pulse excitation in a coplanar strip line has been observed. It is considered to correspond to the probe thickness and the probe distance, defined as the distance from the probe tip facet to the device being tested. A simple transmission line model is used to characterize the time delay between reflections within the probe tip in E-O response [7]. The error may be caused by the reflections, which, however, cannot be evaluated using this simple treatment. Unfortunately, there is little research devoted to the distortion of external electro-optic sampling. This may be attributed to the following reasons. First, the current temporal resolution of the electro-optic sampling system is, in the order of $0.3ps$ [16], constrained by the speed of the instruments. Secondly, the overall accuracy of E-O measurement is also very limited, leading to the fact that most E-O sampling measurements have been done in relative terms [5, 16, 17]. Finally, until the work presented in this thesis is started [9, 10], there has been no comprehensive simulation model (*e.g.* three dimensional, time-domain, full-wave field model) for the probe tip in the external E-O sampling [9, 10]. In spite of those limitations, this measurement technique is intended to be an excellent candidate that can provide wide bandwidth, accurate signal reproduction and minimum invasiveness. To realize these features, not only the invasiveness, but also the distortion should be addressed quantitatively in

both theoretical and experimental ways. In order to quantitatively determine the distortion, a comprehensive theoretical model of the optical probe tip and the full wave field analysis of the field distribution in the probe tip are desirable, specially in time domain where the data are first taken in electro-optic sampling.

In this section, the field and the distortion of electro-optic response are addressed in detail using the full wave time domain FD-TD method. It is organized as follows: first, the field simulation results are presented to demonstrate the distortion in both time domain in terms of the waveform and frequency domain in terms of the S-parameters. Then, a system transfer function is defined and introduced to characterize the distortion caused by probe tips. It is followed by an analysis of the distortion at different sampling positions in the probe tip with regard to the different thickness of the probe, the different probe distances and the different materials. Based on these discussions, the optimum sampling technique is attempted in the analysis.

5.2 Distortion in the external electro-optic sampling

The distortion may be characterized in either time domain or frequency domain or both. When the optical and physics problems are addressed, the time domain specifications, such as full-width half-maximum (FWHM), the pulse rising and falling time, pulse shape and energy, are usually of interest. On the other hand, the

frequency domain information, such as the scattering parameters, the bandwidth, impedance and matching, is of greater interest to circuit and system engineers. In this chapter, the distortion of external E-O sampling is evaluated and discussed in both time and frequency domains. It should be pointed out that the information in the frequency domain is extracted from results of full-wave time domain field simulation.

5.2.1 Distortion in the time domain

Figure 5.36 shows the waveform comparison of the field at the position of the probe center with and without the probe when the $LiTaO_3$ probe distance is 5 μm. First, it can be seen that the quasi-TEM mode is no longer valid in the probe tip since the longitudinal component E_x, shown in dashed-dot line in the figure, is noticeably larger than the original CPW dominant component E_z, shown in solid line, in magnitude. The reason for this has been explained in Chapter 4. Secondly, a significant change in waveforms is observed when the probe is placed. The long ringing at the trailing side in the field response is apparently due to the multiple reflections between the probe facet and the interface with the fused Silica support. There are primarily two reflections: the one between the probe facet and the interface with fused silica, and the other between the probe leading and rear edges. By using a simple transmission line analysis, the time delay between the main pulse and the reflection may be given as

$$t_{thickness} \approx 2h_2 \frac{\sqrt{\epsilon_{r2}}}{c} \tag{5.116}$$

$$t_{width} \approx 2w_1 \frac{\sqrt{\epsilon_{r2}}}{c} \qquad (5.117)$$

where $t_{thickness}$ is associated with reflections between the probe facet and fused Silica support, and t_{width} the time delay of reflections between the probe leading and rear edges. h_2 and w_1 are respectively defined in Chapter 4 as the probe tip thickness and probe tip width. c is the speed of light and ϵ_{r2} is the dielectric constant of the $LiTaO_3$ probe, and then:

$$t_{thickness} \approx 0.874ps \qquad (5.118)$$

$$t_{width} \approx 8.74ps \qquad (5.119)$$

It can be confirmed from the Figure 5.36 that about every 9 ps after the main pulse, there is an approximate destructive interference between the reflected waves from the probe leading edge and from the rear edge. This reflection is also observed by Frankel [7].

The major ringing or oscillation developed at the trailing side of the pulse response in the probe tip is believed to have a period of t_{width} [7]. However, from Figure 5.36, the period of the oscillation seems to be $\sim 2t_{width}$. The time delay between each adjacent positive peak and negative peak is about t_{width}. The reason for this may be attributed to the influence of the CPW which exhibits capacitive loading effect on the probe tip. It equivalently extends the thickness of the probe tip to a degree which results in the discrepancy in oscillation period.

In order to investigate the influence of the fused Silica support on the field

distribution, a simulation is made on a hypothetical case where the $LiTaO_3$ probe tip is placed 5 μm above the CPW without fused silica support. Figure 5.37 shows the waveform comparison of the fields at the probe center with and without the fused Silica support. For either of the three electric field components, there is no noticeable difference in the main pulse. However, reflections from the interface with the support are found to be slightly smaller in magnitude and higher in oscillation frequency than reflections from the interface without the support.

From Figure 5.36 and Figure 5.37, it can also be realized that the temporal resolution has to be in the sub-picosecond range, so that these ringings or oscillations at the pulse trailing side can be observed experimentally. This may be the reason why there are only a few reports [7] on these phenomena.

Finally on a closer look of the Figure 5.36, a slight delay in response can be found as compared to the case without the probe. Thus, it may be concluded that there is a significant distortion of waveforms in probe tip in the time domain. Further work needs to be done on evaluation of the possible error caused by these distortions in the frequency domain.

5.2.2 Distortion in the frequency domain

In order to investigate the measurement error caused by the temporal waveform distortion, the information in the frequency domain is extracted by Furiour transform from the field simulation results in the time domain. The distortion, therefore,

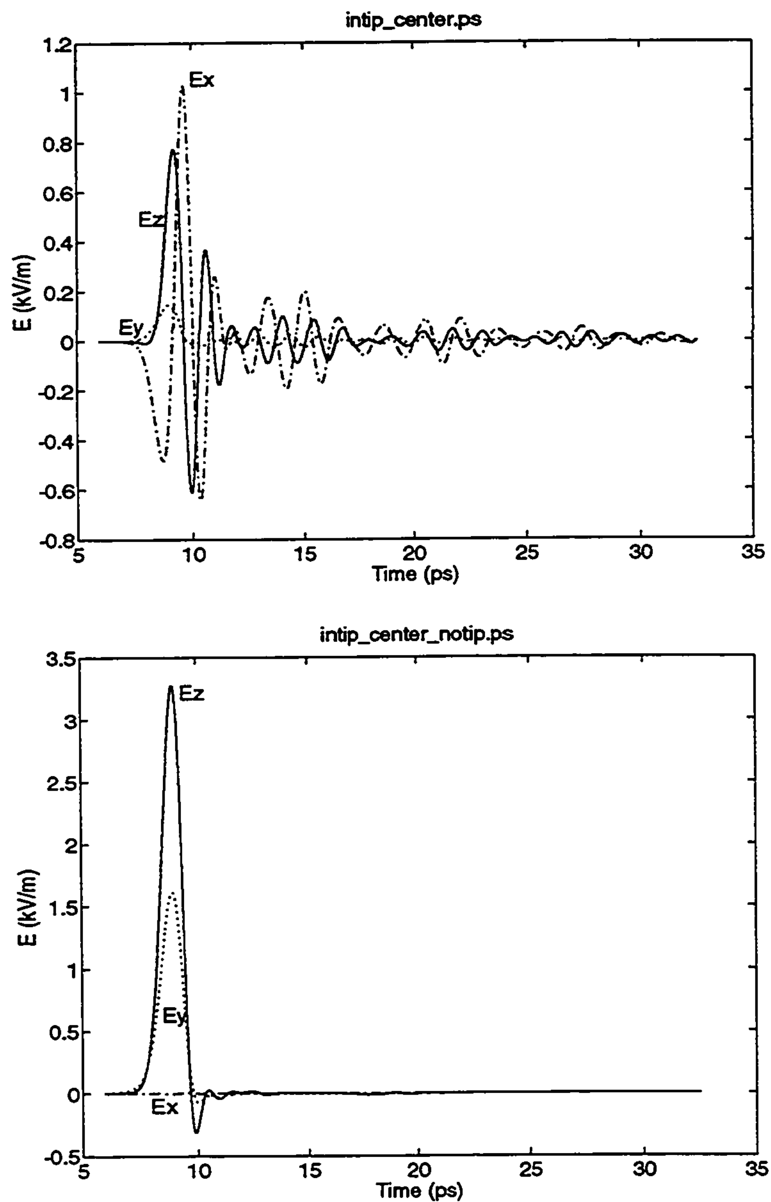

Figure 5.36: Waveform comparison of the fields at the position of the probe center with the probe (a) and without the probe (b). Quasi-TEM mode is no longer held in the probe tip since the waveforms are obviously distorted. A long tail ringing and a delay are observed. The probe distance is 5 μm.

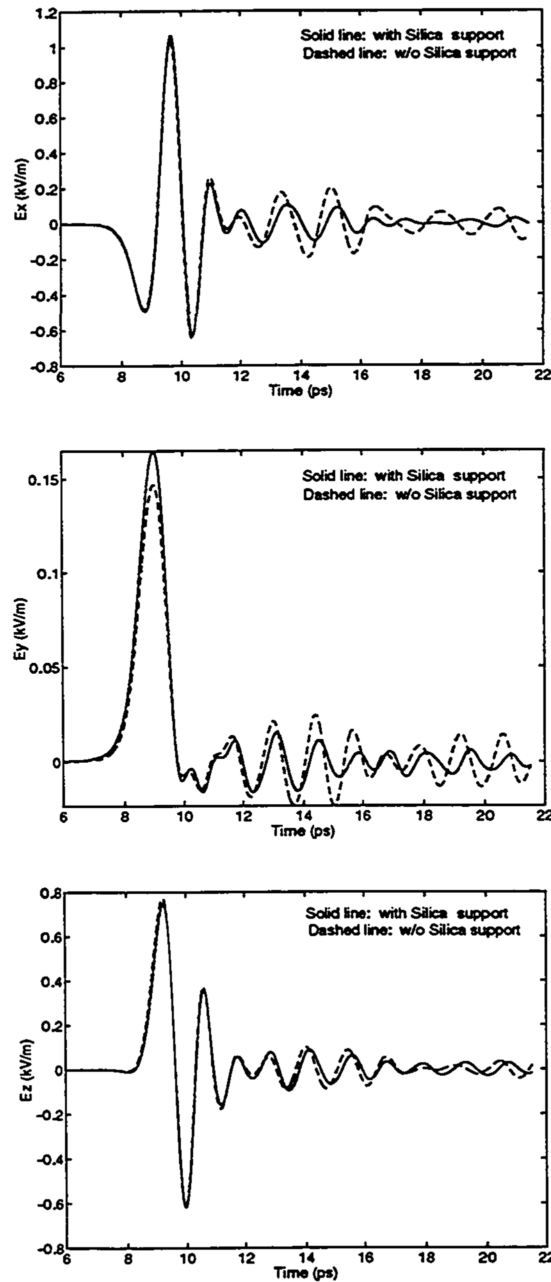

Figure 5.37: Waveform comparison of the fields at the probe center with and without the fused Silica support. The probe distance is 5 μm. E_x is the longitudinal component of the electric field; E_y one of the transverse component of the electric field; E_z the original dominant component of the electric field.

can be evaluated by characterizing the system transfer function in frequency domain. Departure of the response of this transfer function from the response in an ideal linear system defines the distortion in external electro-optic sampling.

System transfer function

In the external electro-optic sampling, the typical field energy coupled into the probe tip is very small, producing much smaller voltage through the probe compared to the half-wave voltage V_π, which is defined as the voltage needed to generate retardation of π in the system (Ref. Chapter 2 and Figure 2.4). The probe-beam intensity modulation is, therefore, small and almost linear with respect to the probed field intensity. An analysis of the linearity and the dynamic range of the probe shows that the probe is linear with less than 1% error for signals producing voltages $\leq$ 200 volts when the system is set at the quarter-wave bias (the linear region of the sinusoidal transmission) [57]. Thus, the external electro-optic sampling can be reasonably assumed to be a linear system.

The zero-state response of a linear system to input f(t) is given by its system transfer function [58], defined as the system response to an impulse excitation. As discussed previously, the E-O sampling system is a linear system since only linear E-O effects are involved. As shown in Figure 5.38, the system input is the electric field in the device being tested while the output is the optical response in E-O sampling. Notice that the electric field as the system input is defined at the input reference plane (Ref. Figure 4.16). The system distortion is characterized by the

transfer function.

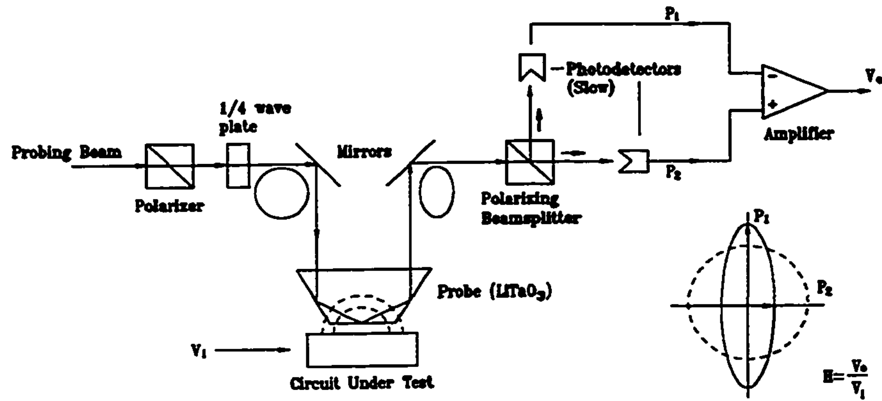

Figure 5.38: Optics for external electro-optic sampling system and definition of the system input and output.

To characterize the E-O sampling system transfer function, the full wave field analysis and the optical output calculation are made for a given electric input. Then the system transfer function H(ω) can be easily evaluated in the frequency domain by (5.120).

$$I_{all}(\omega) = E_{DUT}(\omega)H(\omega) \tag{5.120}$$

where $I_{all}(\omega)$ and $E_{DUT}(\omega)$ are respectively the Fourier transform of the optical time domain output i_{all} in external electro-optic sampling, and the time domain system electric field input e_{DUT}. Both e_{DUT} and i_{all} can be defined or determined practically by field simulation results or through E-O measurements.

In electro-optic sampling systems, it is desirable that the optical response, which is the system output, closely resembles the electric field, which is the system input. Distortion can occur in a linear system if $|H(\omega)|$ and/or the group delay are

not constant for all values of ω [58]. The group delay t_d, the time it takes for the wave energy to travel a unit distance, is defined as [58]

$$t_d = -\frac{d\phi}{d\omega} \tag{5.121}$$

It is obvious that ideally the transmission of a system is distortion-less if and only if both $|H(\omega)|$ and t_d are constant.

System transfer function for the external E-O sampling

Figure 5.39 shows the normalized system transfer function of the external E-O sampling for the $LiTaO_3$ probe thickness of 20μm when the probe distance is 5 μm. A deviation less than 1 dB in frequency response is observed below 200 GHz, which practically ensures the distortion-less measurement approximately up to 2.5 ps range. Two resonant-like peaks occur at 600 GHz and 800 GHz which may correspond to the probe thickness or the small oscillations in the time domain developed at the trailing side of the pulse response (See Figure 5.36 or Figure 5.37). Actually 10 dB difference in frequency response can be seen at 600 GHz in Figure 5.39. A sharp decrease in frequency response beyond 800 GHz suggests that a significant distortion in magnitude will be introduced when this probe is used for measurements where the pulse cycle involved is in the order of sub-picosecond. These resonance influences primarily determine the distortion in the external E-O sampling and are considered as the major limit of probes as far as the measurement accuracy is concerned. For example, the 3 dB frequency bandwidth of the probe

used in this study is found to be $\sim$ 315 GHz. Studies in this research show that the optical output can resemble the input signal in the form of an electric field when the 3 dB bandwidth in the frequency domain is equal to or wider than the 10 dB cutoff frequency in the spectrum of the input signal.

The phase information in Figure 5.39 is generated in such a way that it is kept to be continuous over the π borders. The group delay, shown in Figure 5.39 as well, is also calculated for extracting more information on transmission from the phase. Since the transfer function includes the CPW section separating the probe and the input reference plane, it is necessary to de-embed the contribution in both magnitude and phase of the transfer function in order to characterize the probe itself properly.

Figure 5.40 shows the normalized transfer function associated with the input port defined at the input reference plane and output port on the CPW right under the probe center. By comparison with Figure 5.39, the contribution of the CPW section which separates the probe and the input reference plane is obvious especially in terms of phase or group delay. In addition, it can be seen that the CPW is good for high speed transmission because its group delay is nearly a constant up to 800 GHz.

Properties of the electro-optic transducer, *i.e.* the probe itself, can be derived from Figure 5.39 and Figure 5.40 and the results are shown in Figure 5.41. Referring to the previous discussion on the ideal transmission system, it is concluded from this figure that the $LiTaO_3$ probe with thickness of 20 μm can

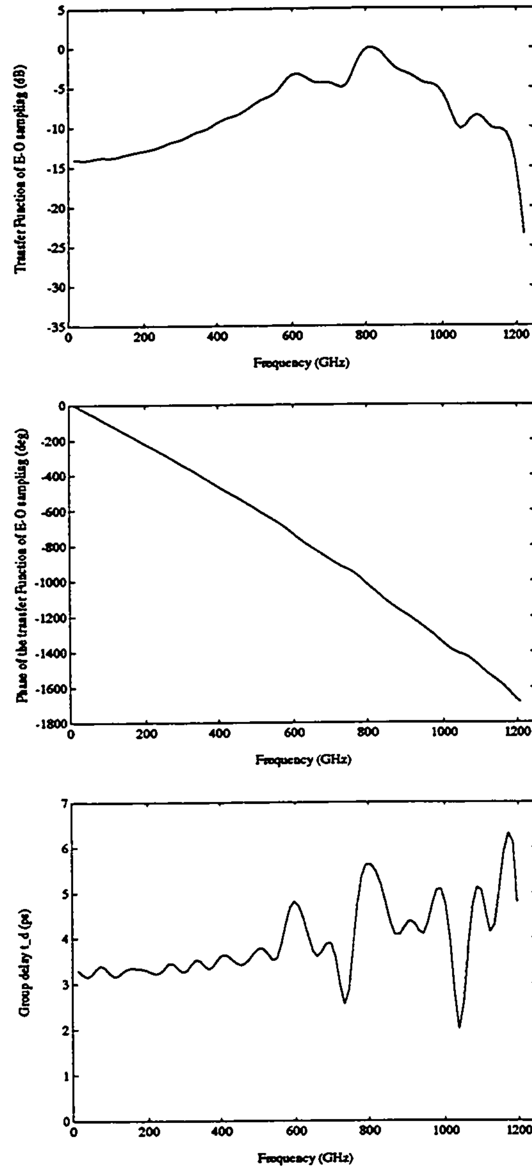

Figure 5.39: The system transfer function of the external E-O sampling for the $LiTaO_3$ probe thickness of 20μm when the probe distance is 5 μm. (a). Magnitude. (b). Phase. (c). Group delay. An approximate constant frequency response up to 200GHz, two resonant-like peaks at 600GHz and 800GHz, and a sharp decrease in magnitude beyond 800GHz can be observed.

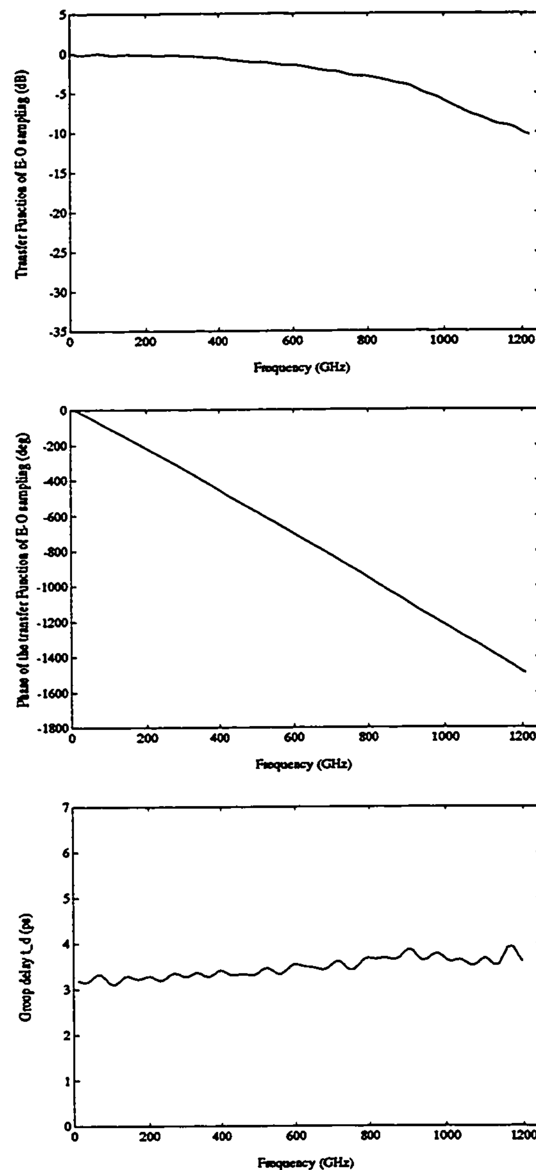

Figure 5.40: The system transfer function of the CPW from the input reference plane to the sampling position right under the center of the probe tip. The probe distance is 5 μm. (a). Magnitude. (b). Phase. (c). Group delay.

produce a quantitative measurement with a little effort (See Chapter 6) up to 310 GHz where the 3 dB response occurs. Although the magnitude has 5 dB difference at 400 GHz as compared to the response at DC, it may work well with reasonable accuracy since the phase is still a linear function of the frequency and the group delay is virtually a constant up to that frequency. However, there is an upper limit for this probe as clearly demonstrated in Figure 5.41. It can be seen that any frequency component higher than 500 GHz suffers not only the loss in sensitivity or/and the transmission linearity by more than 10 dB, but also significant dispersive distortion in phase or group delay although it may be calibrated to a better degree (See Chapter 6). In other words, the pulse, whose 10 dB cutoff point in its frequency spectrum is higher than 400 GHz, is not recommended to be tested using this probe.

Distortion of the external electro-optic sampling has been demonstrated throughout this section in both time domain and frequency domain. It has been shown that the distortion is highly dependent on thickness of the optical probe tip and the frequency range concerned. The modeling technique used in this research can be applied to any type of probes. Therefore, a theoretical limitation of probes can be evaluated as far as the speed of the device being tested and the E-O sampling system are concerned. For example, given a probe, its distortion should be fully characterized and properly calibrated out, especially in picosecond and sub-picosecond domains where the distortion is inevitably significant. The following sections are intended to further investigate quantitative dependencies of

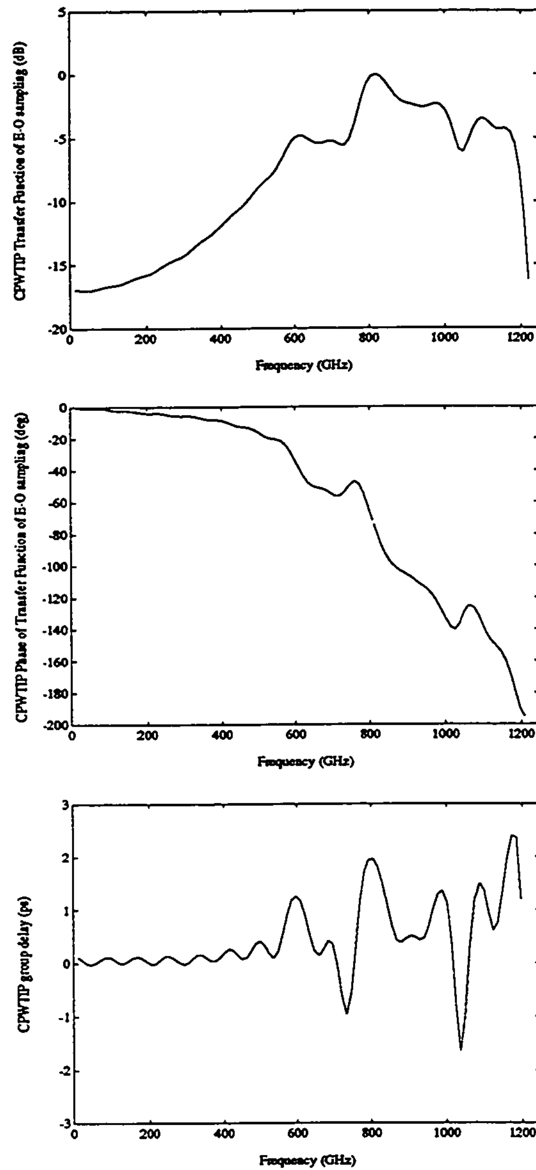

Figure 5.41: The transfer function of the $LiTaO_3$ probe itself defined from the CPW position under the center of the probe tip to the optical output. It is basically determined by the thickness of the probe tip, which is 20 μm in this analysis. The probe distance is 5 μm. (a). Magnitude. (b). Phase. (c). Group delay.

the distortion on probe materials and dimensions, and sampling positions in the probe tip.

5.3 Characterization of the probe distortion

5.3.1 Dependency on probe thickness

The thickness of the probe tip may play the most important role in its characterization. Experimentally in Frankel and Mourou's work [7, 16], it was observed that the probe geometries used for most experiments introduce significant errors. However, there is no analytical and comprehensive model for the probe tip until the research in this work. In the last section, the distortion generated in the probe tip has been related to the probe thickness based on the full wave modeling results. In order for the distortion to be understood in a detailed and systematic way, its dependency on the thickness of the probe tip needs to be investigated.

In the following studies, the time taken for a sampling beam to travel through the probe tip is considered in the field simulation and the optical output calculation (Refer to Chapter 3). Figure 5.42 shows the normalized temporal waveforms of the optical output using $LiTaO_3$ probe with a set of different probe tip thickness. It can be observed that waveform responses are different for different probe tip thickness. In addition, a closer look indicates that the wave in the probe shows no significant delay in transmission. To extract more information from these waveforms, performance in the frequency domain is obtained using Fourier

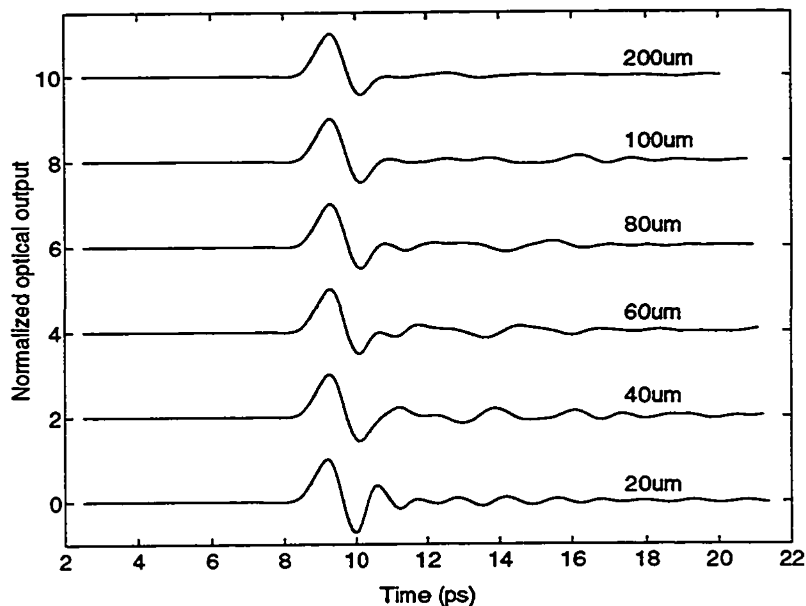

Figure 5.42: Normalized optical signal waveforms for different $LiTaO_3$ probe tip thickness

.

transform.

Figure 5.43 presents the magnitude of the probe tip transfer function in which the effect of the CPW section separating the probe and input reference plane has been taken out. The results for 20 μm thickness probe have been discussed in the last section. Apparently the slope of the frequency response is getting larger and larger with respect to the 20 μm case as the the thickness increases. This is attributed to the decreasing in resonance frequencies associated with the thickness of the probe tip. As a result, the bandwidth of the probe tip is, to a certain

degree, inversely proportional to its thickness. Notice that 100% transparency and reflection are assumed respectively at the top $LiTaO_3$ Silica support interface and the output facet of the probe. The frequency response of the probe may be different from that in Figure 5.43 if multiple reflections in the probe tip are considered. However, even with effects of the multiple reflections being taken into account, there is no significant impact on the bandwidth of the probe tip since the multiple reflections are second order effects compared to the effects determined by the thickness of the probe tip.

Generally the magnitude of a system is not as sensitive as its phase response. Figure 5.44 shows the probe phase response for a set of the different probe tip thickness. As mentioned previously, the phase response of an ideal transmission system is linear versus frequency. It can be seen that the thiner the probe tip thickness, the wider the linear phase response range. It is consistent with the conclusions of the experimental studies [4, 7]. To be more clear in characterizing these probes, the group delay associated with these phase responses is calculated and shown in Figure 5.45. The dependency of the probe bandwidth on the probe tip thickness is clearly demonstrated in this figure. Obviously the 20 μm probe tip in these probes offers the widest bandwidth in which the group delay is nearly a constant. However, several-picosecond delay in all these probes in the frequencies up to about 400 GHz can hardly be observed by most current electro-optic sampling systems due to the availability of the pulse width. That may explain why there are only a few reports published on signal distortion in picosecond and sub-picosecond

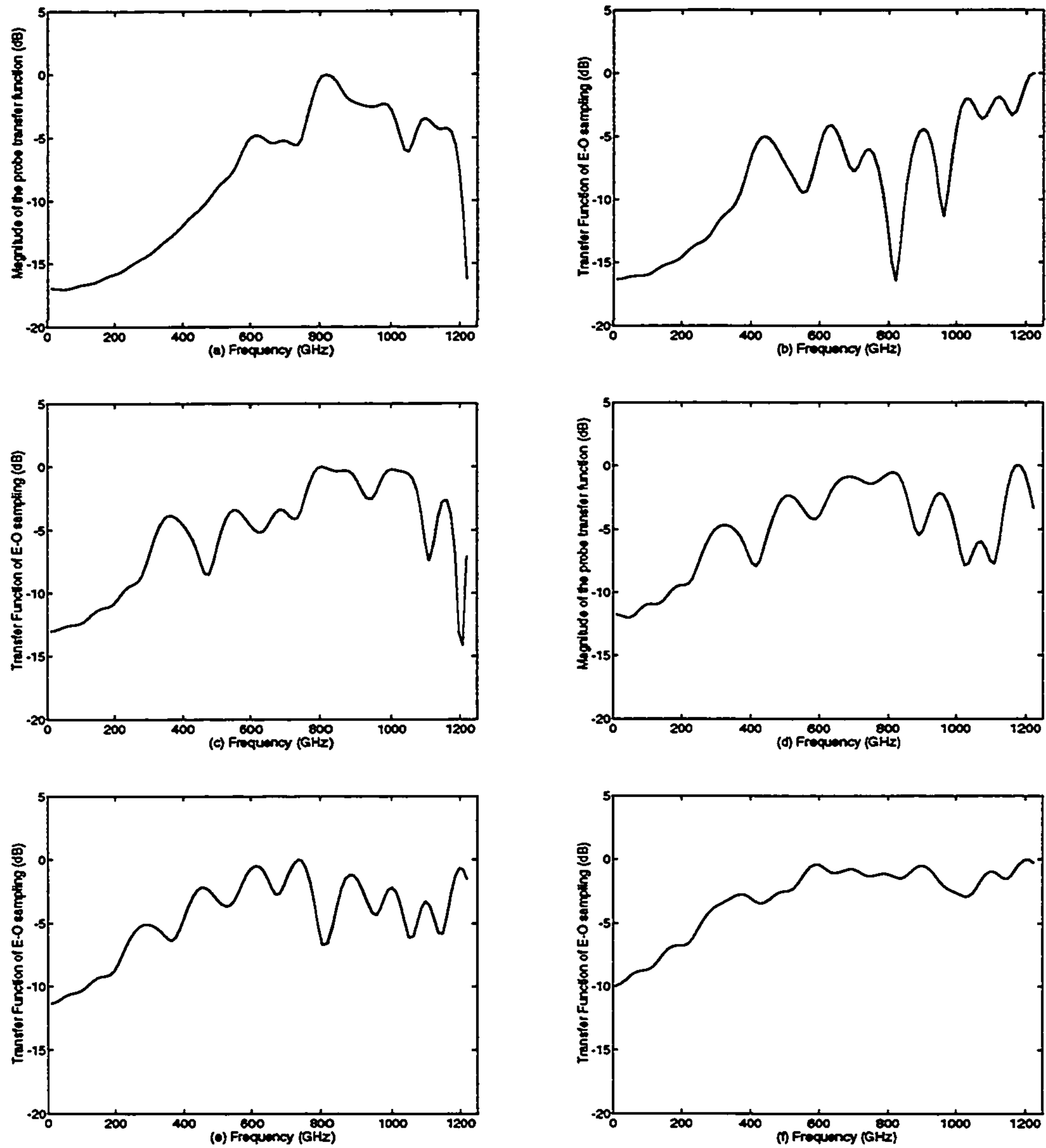

Figure 5.43: The magnitude of the system transfer functions of the external E-O sampling for the $LiTaO_3$ probe in different thickness (a) 20μm. (b) 40μm. (c) 60μm. (d) 80μm. (e) 100μm. (f) 200μm.

domains [4, 7].

For a better performance of the probe tip, a thiner probe tip is needed according to the previous analysis. On the other hand, less measurement sensitivity is expected for the thiner probe because of the shorter sampling path along which the overall optical signal is integrated in proportion to the electric field in the probe tip. The probe thickness, therefore, must be carefully chosen so that a trade-off can be achieved between the performance, determined primarily by the probe tip thickness, and the measurement sensitivity, governed again by the probe tip thickness when the probe distance is given. Fortunately the electric field is mostly confined in a very limited region near the probe facet. Consequently, the sensitivity is attributed dominantly to the field in that limited region. This result is illustrated clearly in Figure 5.46. A saturation-like phenomenon can be seen in relation of the optical signal intensity versus the probe tip thickness. It suggests that there is no need to infinitely increase probe tip thickness.

Clearly the full wave time domain simulation and transfer function approach have substantially pushed the research in calibration further forward towards the quantitative measurement. Up to this stage, it is possible to characterize the probe quantitatively and to consider compensation or calibration of the probe effect in electro-optic sampling. This can be done in terms of both the magnitude and the phase response in the frequency domain or the delay and distortion of the temporal pulse waveform through the transfer function of the probe.

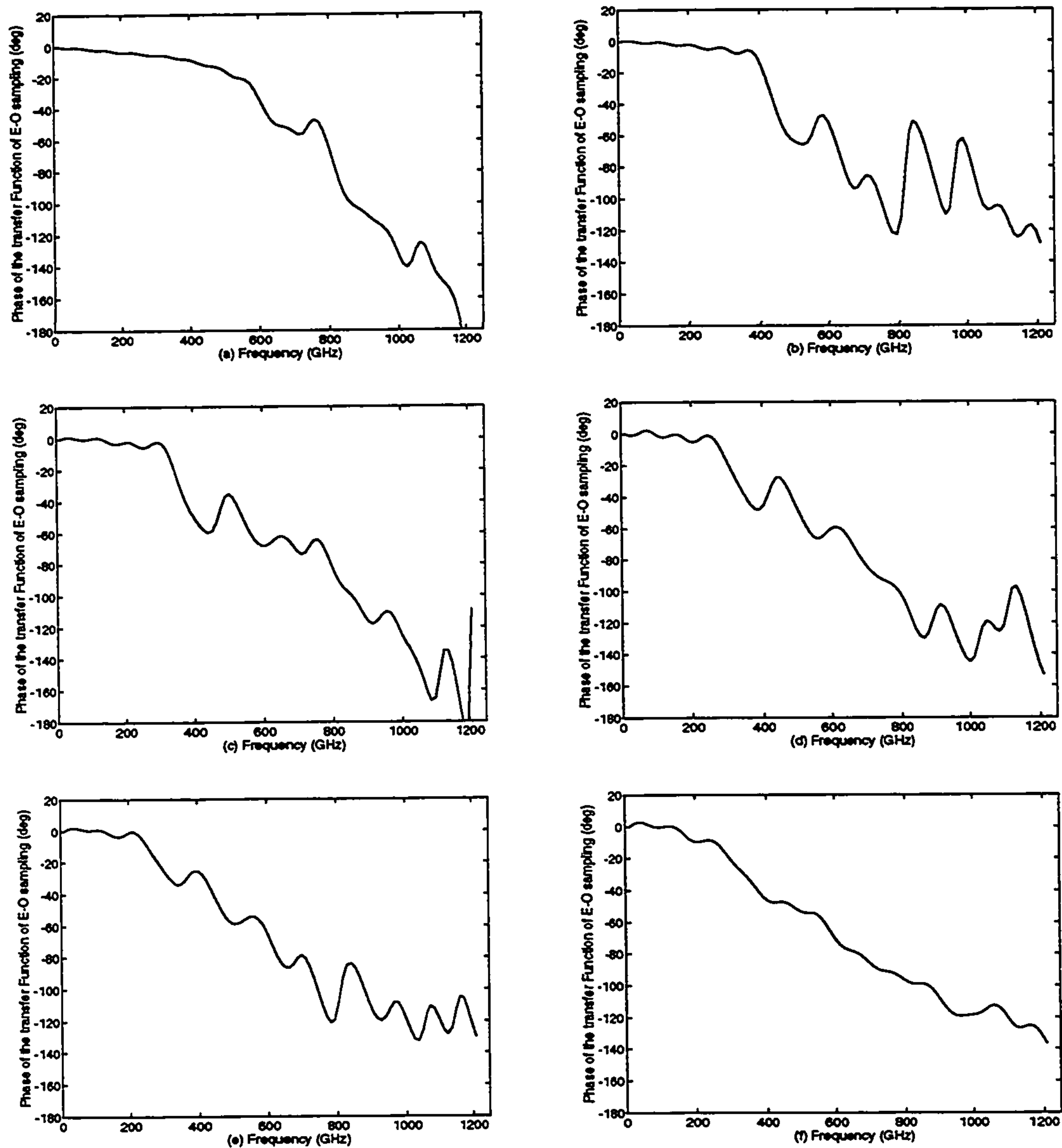

Figure 5.44: The phase of the system transfer functions of the external E-O sampling for the $LiTaO_3$ probe in different thickness (a) 20μm. (b) 40μm. (c) 60μm. (d) 80μm. (e) 100μm. (f) 200μm.

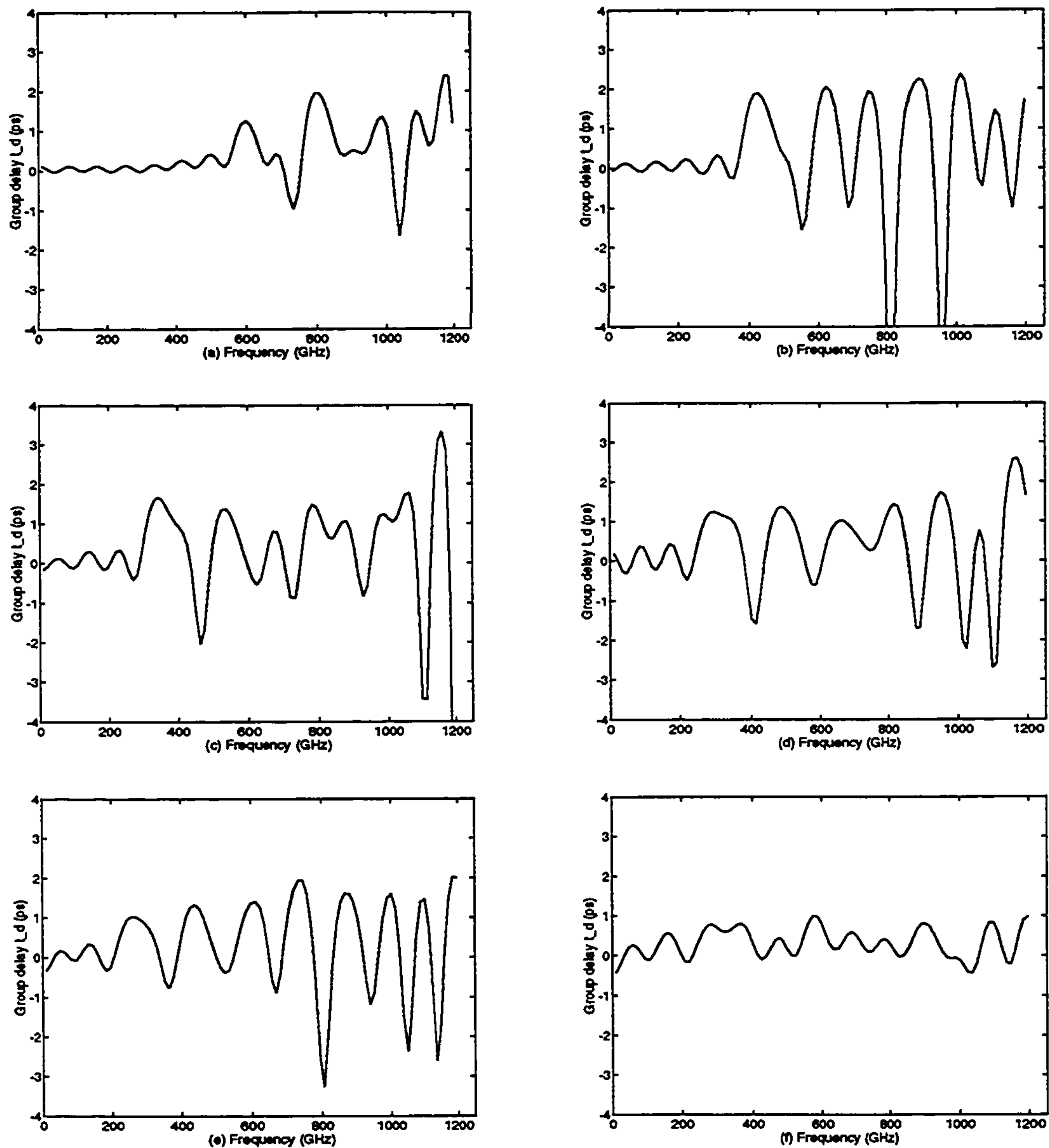

Figure 5.45: The group delay of the systems of the external E-O sampling for the $LiTaO_3$ probe in different thickness (a) 20μm. (b) 40μm. (c) 60μm. (d) 80μm. (e) 100μm. (f) 200μm.

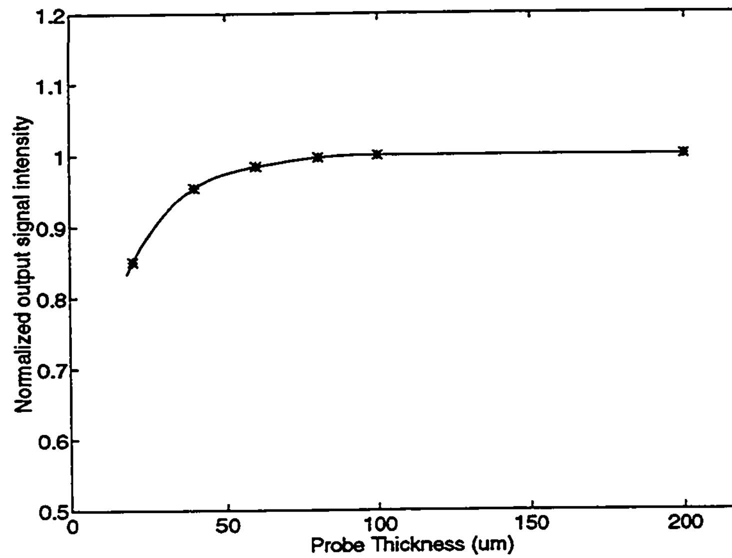

Figure 5.46: .
Normalized optical signal intensity *v.s.* the $LiTaO_3$ probe tip thickness. The signal intensity is attributed dominantly to the limited region near the probe facet since the field in the probe is mostly confined there.

5.3.2 Dependency on probe materials

Previously, probe material is chosen mainly according to the requirement of sensitivity and sampling geometry, *i.e.* transverse or longitudinal sampling. Yet, just recently the invasiveness and distortion of probing are taken into account in the choice [4, 7, 9, 10]. Several electro-optic materials have been considered for the external electro-optic sampling [2, 4, 7, 59]. Intuitively, the material with a lower dielectric constant shows smaller invasiveness. However, it seems to be true that the high dielectric material usually offers larger electro-optic coefficient, which in turn interprets higher E-O sampling sensitivity. Among the materials available for electro-optic sampling, $LiTaO_3$ and GaAs are most widely used.

Figure 5.47 shows the temporal waveforms of the optical signal outputs as the response to a Gaussian pulse propagating through the CPW when the electric-field is sampled at the center of $LiTaO_3$ and GaAs probes. The outputs are normalized to the maximum value of the signal from the $LiTaO_3$ probe. As mentioned in previous chapter, a significantly large waveform distortion occurs in $LiTaO_3$ probe although it produces about 3 times higher signal strength in the measurement compared to GaAs probe (Ref. section 4, Chapter 4). Since GaAs probe has much smaller dielectric constant in comparison to the $LiTaO_3$, the probing discontinuities, reflections and distortions in the probe are expectedly smaller. It can be seen that the GaAs probe is almost ideal in terms of fidelity of signal transmission. Notice that in Figure 5.47 the probe distance is 5 μm and probe thickness is 20 μm.

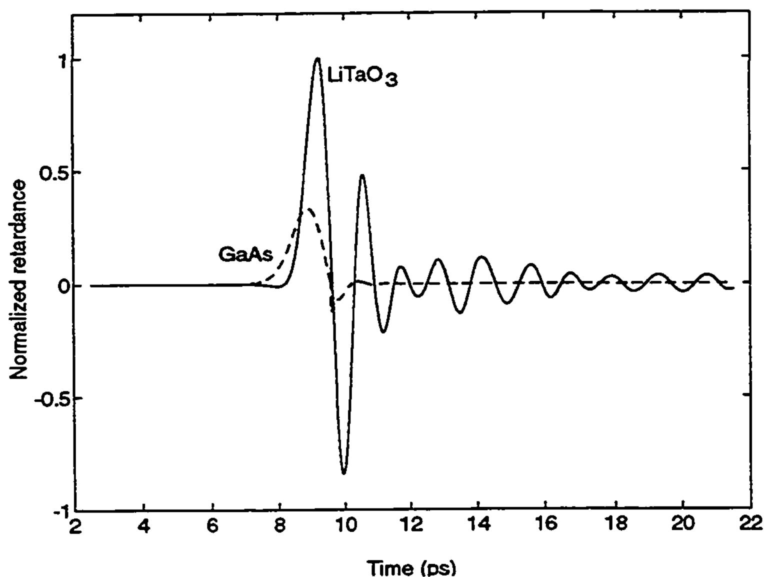

Figure 5.47: Distortion dependency on probe material while the field is sampled at the probe center. $LiTaO_3$ probe exhibits a significantly distortion and GaAs probe is nearly ideal in terms of the transmission. However, higher sensitivity is obtained using $LiTaO_3$ probe. The probe distance is 5 μm and probe thickness is 20 μm.

The transfer function in the frequency domain is usually used in system characterization. In this research report, a two-port system is defined in terms of the electrical *input* and the optical *output*. The input is the electric field on the CPW right under the sampling spot where the probing beam is focused in the probe tip, and the output is the sampling system output which is proportional to the electric field in the probe tip. The system transfer function, when the electric field is sampled at the probe center, is shown in Figure 5.48 for $LiTaO_3$ and GaAs probes. Again the results are normalized to the maximum value of the signal from $LiTaO_3$ probe for the sake of the comparison. Notice that both magnitude response and phase or group delay of the GaAs probe are an almost ideal linear response in a large bandwidth up to 900-1000 GHz. This can be seen more clearly from group delay results of the system (See Figure 5.45). Although the signal from the GaAs probe is 2$\sim$10 dB lower in intensity as compared to that from the $LiTaO_3$ probe, the demonstrated excellent performance up to terahertz frequency band shows a great potential in the quantitative measurement of picosecond and sub-picosecond signals.

5.3.3 Dependency on sampling positions

Previously there was no sampling field model available for an analysis of the measurement dependency on sampling positions. With the technique presented in this thesis, it can be conducted straightforwardly.

Figure 5.48 shows the optical output when the electric field is sampled at the

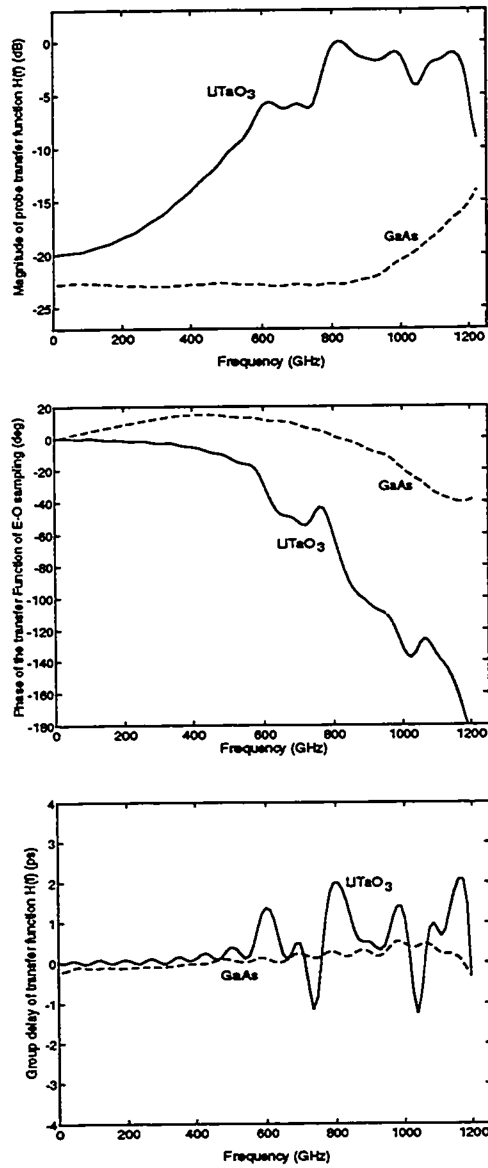

Figure 5.48: Distortion comparison in terms of transfer functions between $LiTaO_3$ and GaAs probes at the probe center. The probe distance is 5 μm.

probe center. Figure 5.49 gives temporal waveforms associated with the sampling position at the probe leading edge, where the sampling spot is only 13μm away from the probe leading edge. It is the same as sampling at the probe center that the GaAs probe produces less distortion than the $LiTaO_3$ probe. Oscillations with the $LiTaO_3$ probe after 14 ps are attributed to the reflections from the rear edge of the probe. To obtain information of the device being tested, these reflections may be subtracted from the overall output as long as the time interval is long enough between the main pulses and the reflections. From Figure 5.47 and Figure 5.49, it may suggest that less distortion can be produced if the electric field is sampled at the probe leading edge rather than at the probe center in the traditional way of sampling.

Figure 5.48 shows the frequency transfer function of two probes when sampling at the probe leading edge. Note that the results again are normalized to the maximum value of the signal from the $LiTaO_3$ probe when the electric field is sampled at the probe center. It means the signal level reference is same as the one used in Figure 5.48. By comparison of the results at the probe center and the leading edge, improvement in the terahertz frequency range is observed, which agrees with conclusion of the visual inspection in time domain from Figure 5.47 and Figure 5.49. It may indicate that sampling near the probe leading edge can result in less distortion than sampling at the probe center.

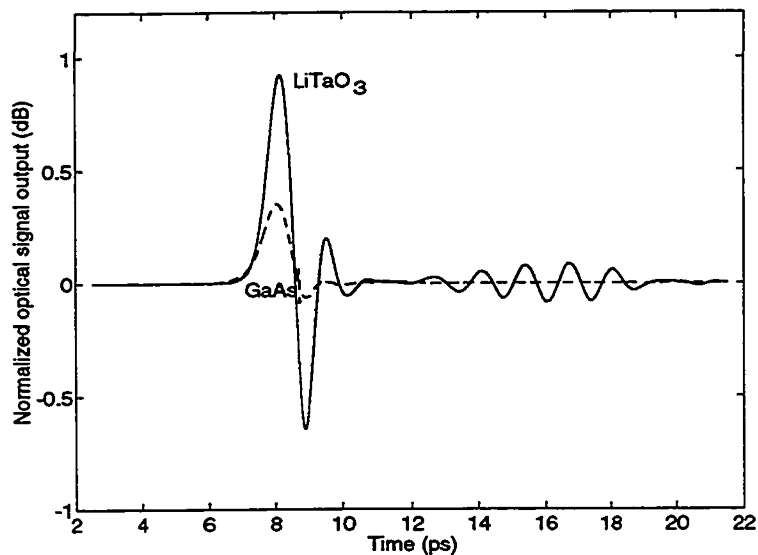

Figure 5.49: Distortion dependency on sampling positions. The waveforms are sampled at the probe leading edge. $LiTaO_3$ probe shows larger distortion and GaAs probe offers significantly lower distortion. However, larger electro-optic response is obtained using $LiTaO_3$ probe.

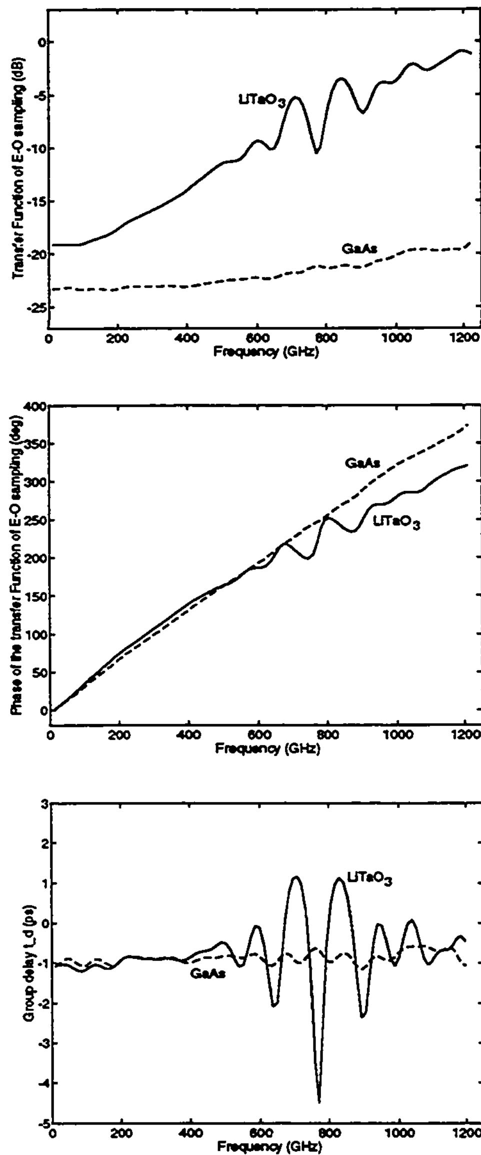

Figure 5.50: Distortion comparison in terms of transfer functions between $LiTaO_3$ and GaAs probes at the probe leading edge. The improvement in terahertz frequency range can be seen compared with the case when the electric field is sampled at the probe center.

5.4 Conclusions

A system transfer function has been defined and used to characterize the probe. It has been found that the thinner the probe, the less distortion and the sensitivity. Therefore, a tradeoff is desired. Fortunately, the research results show that simply increasing thickness of the probe in external E-O sampling can only improve sampling sensitivity by about 20% from $20\mu m$ to $60\mu m$ and almost nothing from $60\mu m$ to anywhere thicker.

The GaAs probe can ensure the measurement reliability up to picosecond and sub-picosecond domains. Its nearly linear frequency response, both in magnitude and phase, makes measurement calibration much easier and more straightforward. In contrast to GaAs probe, special care should be taken in applying $LiTaO_3$ probe to picosecond and sub-picosecond domain due to possible severe distortion. Further research is needed to calibrate out the distortion governed primarily by the probe thickness and its dielectric constant. However, $LiTaO_3$ probe can offer noticeably higher output intensity, especially at high frequency band. Unfortunately it is also the very situation where the most severe distortion occurs. For the widely used probe thickness of $20\mu m$, the distortion is insignificant up to 200GHz for $LiTaO_3$ probe and 600GHz for GaAs probe.

The research results also suggest that probing at leading edge of the probe offers less distortion in the measured signal.

Chapter 6

Calibration of the External Electro-Optic Sampling

6.1 Introduction

The external Electro-optic sampling shows promising results in its high frequency capability and noninvasive property in measurement at internal node on MMICs and other high speed devices [34, 60]. However, calibration of probe effects and quantitative measurements has received little attention. Consequently, most E-O sampling measurements have been done in relative terms [5, 16, 17].

The purpose of calibration of the E-O sampling is to relate the signal voltage or field on the device being tested to the change in polarization of the optical probing beam. Such calibration is to de-embed the invasiveness and distortion for accurate and reliable measurement. Consequently, it requires modeling of the

electric field in the sampling configuration and the resultant probe birefringence. This problem was raised several years ago [5], but the full wave field modeling in the probe and its vicinity is not yet available; neither is the evaluation of electro-optic effects manifested on the sampling beam, which takes the three dimensional field distribution into consideration.

A field-based calibration technique is proposed in this chapter for external E-O sampling by means of vector composition method and a system transfer function, which can be derived from the field simulation results and E-O response calculations reported in previous chapters. In this technique, it is possible to de-embed both the invasiveness and the distortion in external E-O sampling given the sampling configurations and dimensions. It moves E-O sampling further towards the quantitative measurement.

6.1.1 Optical excitation system

With regard to optical excitation system set-up, a reference calibration technique has been widely used to find the absolute magnitude of sampled signals [18], where a known signal is applied to the device being tested through a transmission line to define a standard measurement [16]. The absolute magnitudes of input and output electrical signals are then determined by referencing the measured signal levels to this standard measurement. This reference signal may be a 10 mV square wave signal at the frequency of several megahertz [18]. The D.C. signal is usually not used as the reference signal for the following two reasons. First, a several megahertz

modulation frequency is needed to avoid a large 1/f noise on the sampling signal receiving end. Secondly, the circuit being tested using on-chip photo-conductive switch as a signal generator has its own D.C. bias configuration, which may be different in D.C. signal response from circuit to circuit.

The reference technique implicitly assumes that the probe tip and other sampling components are ideal transducers which have constant amplitude and linear phase response over the entire frequency band of measurement. However, the transfer function of the probe tip as a transducer may be quite frequency dependent (Ref. Chapter 5). In other words, a standard measurement at several megahertz may not necessarily provide a good reference for sampled signals, especially when the transient response and the response at high frequency up to several hundred gigahertz are the concern in the measurement. In addition, the circuit being tested may have a frequency-dependent response to the test signal, which also could affect the measurement accuracy when this reference calibration technique is employed. More importantly, it has been observed that a very small change in the orientation of the probe and other optic devices can result in significant deviations from the optimized set-up. Unfortunately, it is inevitable in practical measurements. Whenever the probe tip or any other optic devices are moved, the test conditions in this standard measurement are very unlikely to remain unchanged. All these factors are the major cause for significant errors in the previous quantitative measurements.

6.1.2 Synchronous sampling system

In the synchronous sampling system as introduced previously in Chapter 2, the phase and amplitude of electrical signal are detected using the harmonic mixing technique [17]. The repetition rate of the laser is chosen so that one of its harmonic frequencies is close to the operating frequency of the circuit. The electro-optic effect mixes the laser harmonics with the signal frequency, producing a modulation at a different frequency which preserves the amplitude and phase of the original signal being tested. The frequency response of the circuit being tested is obtained by using different harmonics of the laser, and by varying its fundamental frequency so that the response between the original harmonics can be measured.

During the process of choosing different harmonics of laser pulses to drive the circuit being tested, changes are likely to occur in phase reference between the laser and the electrical signal source driving the circuit. To track these changes and to prevent them from affecting the measurements, Heutmaker *et al* reported a synchronization technique to generate a relative phase reference for measuring phase response [61]. The phase reference is obtained by mixing the signal driving the circuit with one of the harmonics of the laser pulses at a frequency close to the operating frequency of the circuit. The signal applied to the mixer may be respectively supplied by coupling of the electrical signal and the harmonics of laser pulses generated at the output of a photo-diode.

The phase reference signal is then directed to the lock-in amplifier to track

the changes of phase relationship between laser and the electrical signal source. It has been proven experimentally that Heutmaker's technique works well up to 15GHz [61] for phase reference. However, as compared with conventional electrical measurements, its amplitude response has a relatively poor accuracy. The reason again lies in difficulties of the probe orientation consistency relative to the electric field being tested when the probe is moved for measurement at different positions [14]. In addition, packaging of the device or circuit being tested in E-O sampling is typically different from that in conventional tests using network analyzer. This could be another cause for discrepancies in comparison of the data obtained by conventional network analyzer.

6.1.3 Field modeling

Perhaps in previous research on E-O sampling, the work of T. Nagatsuma *et al.* at *NTT LSI Laboratories* is the most similar to the work presented in this thesis [35]. A two dimensional static field model of an external electro-optic sampling has been used to analyze the sensitivity of the measurement system in [35], where a uniform field is assumed in the CPW propagation direction. Since the birefringent material of external probe has a large dielectric constant, the above assumption is questionable at least under the condition of ultrashort pulses which have rich components over the frequency range up to terahertz. The solution of such a problem demands a full-wave three dimensional field simulation and a transient analysis. In addition to the sensitivity of the system, the probing invasiveness has

also been investigated by T.Nagatsuma's group in terms of reflection coefficient derived from the quasi-static field model at low frequencies where the TEM mode propagation is assumed. On the other hand, at high frequencies as described in [35], a different approach has been used which is called the Bergeron method, a three dimensional lattice network modeling technique very similar to the TLM or the FD-TD method. However, what has been studied in [35] is only the invasiveness in terms of attenuation as function of the frequency.

By the time when the research reported in this thesis is initiated, the work of T. Nagatsuma's group was the first and the only one which adopted a full wave analysis and static field modeling for investigation of the external electro-optic sampling. However, the full wave modeling should effectively provide wideband results including the quasi-static response and the frequency response up to terahertz. There is no need to investigate the same problem using both the quasi-static field analysis at low frequencies and the full wave modeling at high frequencies. In addition, it is more efficient to evaluate the invasiveness using the same parameters over the entire frequency band. More importantly, the probing distortion can also be addressed in the full wave field modeling approach. Comprehensive understanding of the probing invasiveness and distortion logically leads to a calibration technique for quantitative measurements of external electro-optic sampling.

6.1.4 Recent experimental work

Recently experimental work [4, 7] and theoretical research [9, 10] have been dedicated to probing invasiveness and distortion, which are the two major issues in any calibration technique. Both Frankel at *University of Michigan* and Dykaar at *AT&T Bell laboratories* experimentally demonstrate that the measurement accuracy is primarily determined by the probe thickness [7] and its dielectric constant [4]. It is qualitatively in a good agreement with the research results of this thesis based on the theoretical research [9, 10, 11].

Frankel's recent work [8] may represent state-of-the-art achievements of the external electro-optic sampling. In his research, a small-signal characterization of high-speed semiconductor devices is in an excellent agreement with the results obtained by conventional network analyzer up to 40 GHz. However, in order to reach this agreement, the measured data in electro-optic sampling have been scaled by a constant. But an explanation of the scaling is absent in his initial report [8].

6.1.5 Proposed calibration techniques

The probing invasiveness and distortion have been addressed theoretically in this thesis and the related publications [9, 10, 11]. The results have been qualitatively supported by the experimental conclusions. Hence, calibration techniques are proposed which is based on the full wave field modeling results, reference calibration

method, other previous research and experimental efforts. The proposed calibration techniques attempt to address following problems.

1. **Scattering parameter measurements.** Experimental solutions are proposed respectively for both optical excitation setup and synchronous sampling system.

2. **Calibration of the waveform.** A new proposed technique based on the probe transfer function can de-embed the distortion from the measured waveform.

3. **Calibration of the measured scattering parameters.** A new proposed technique based on the full-wave field simulation results can de-embed the invasiveness from the measured waveform.

6.2 [S] measurements in the time domain

Scattering parameters, thereafter noted as [S] parameters, are among the most important parameters of the microwave and millimeter-wave devices. Almost all the linear circuit designs are made in the frequency domain by means of [S] parameters. This section starts with an introduction of a conceptually simple technique, in which a D.C. standard measurement is taken as a reference signal, and a pre-knowledge of the input signal and transmission line is required in data processing. It is followed by a recommendation of the measurement procedure of scattering parameters.

6.2.1 [S] derived from measurements in the time domain

Scattering parameters providing information in the frequency domain are obtained through the Fourier transform of the measured data in the electro-optic sampling.

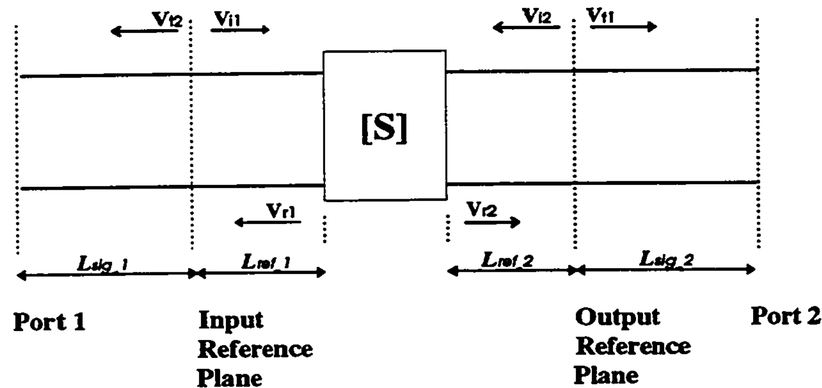

Figure 6.51: Position of the sampling spots, reference planes and device being tested.

In [S] measurements, input and output reference planes should be defined first. The probe is placed respectively at these two reference planes, sampling the corresponding fields $V_{i_1}(t)$, $V_{r_1}(t)$ and $V_{t_1}(t)$ as the responses to the excitation at the input port (*i.e.* port 1), and $V_{i_2}(t)$, $V_{r_2}(t)$ and $V_{t_2}(t)$ as the responses to the excitation at the output port (*i.e.* port 2). Subscripts i, r and t respectively represent incident, reflected and transmitted waves at the corresponding ports. Referring to Figure 6.51, $[S]_m$ may be defined as

$$S_{11_m}(f) = \frac{\mathcal{F}[V_{r_1}(t)]}{\mathcal{F}[V_{i_1}(t)]} \quad (6.122)$$

$$S_{22_m}(f) = \frac{\mathcal{F}[V_{r_2}(t)]}{\mathcal{F}[V_{i_2}(t)]} \quad (6.123)$$

$$S_{21_m}(f) = \frac{\mathcal{F}[V_{t_1}(t)]}{\mathcal{F}[V_{i_1}(t)]} \quad (6.124)$$

$$S_{12_m}(f) = \frac{\mathcal{F}[V_{t_2}(t)]}{\mathcal{F}[V_{i_2}(t)]} \quad (6.125)$$

where V_{r_1} and V_{i_1} are reflected and incident voltage waves at the input reference plane when the signal is applied at port 1.

V_{r_2} and V_{i_2} are the same at the output reference plane when the signal is applied at port 2.

V_{t_1} is the transmitted voltage wave at the output reference plane at port 2 when the signal is applied at port 1 while V_{t_2} is the same at the input reference plane at port 1 except when signal is applied at port 2.

Note that the obtained S-parameters are normalized. In general, [S] are always normalized to the characteristic impedance of the transmission line. If it is not the required standard one, for instance 50 Ω, an impedance transformation is made to normalize both the data and the subsequent [S] parameters to a standard impedance. It may be done by first converting the measured $[S]_m$ to $[Z]_m$ using following relationships [23].

$$Z_{11_m} = Z_0 \frac{(1 + S_{11_m})(1 - S_{22_m}) + S_{12_m}S_{21_m}}{(1 + S_{11_m})(1 - S_{22_m}) - S_{12_m}S_{21_m}} \quad (6.126)$$

$$Z_{22_m} = Z_0 \frac{(1 - S_{11_m})(1 + S_{22_m}) + S_{12_m} S_{21_m}}{(1 + S_{11_m})(1 - S_{22_m}) - S_{12_m} S_{21_m}} \quad (6.127)$$

$$Z_{21_m} = Z_0 \frac{2 S_{21_m}}{(1 + S_{11_m})(1 - S_{22_m}) - S_{12_m} S_{21_m}} \quad (6.128)$$

$$Z_{12_m} = Z_0 \frac{2 S_{12_m}}{(1 + S_{11_m})(1 - S_{22_m}) - S_{12_m} S_{21_m}} \quad (6.129)$$

where Z_0 is the characteristic impedance of the transmission line from which the data are measured in E-O sampling. Then, [Z] obtained from (6.126)-(6.129) are normalized to the required characteristic impedance Z_c by:

$$Z_{11} = \frac{Z_c}{Z_0} Z_{11_m} \quad (6.130)$$

$$Z_{22} = \frac{Z_c}{Z_0} Z_{22_m} \quad (6.131)$$

$$Z_{21} = \frac{Z_c}{Z_0} Z_{21_m} \quad (6.132)$$

$$Z_{12} = \frac{Z_c}{Z_0} Z_{12_m} \quad (6.133)$$

Finally, [S] normalized to Z_c can be derived by:

$$S_{11} = \frac{(Z_{11} - Z_c)(Z_{22} + Z_c) - Z_{12} Z_{21}}{\Delta Z} \quad (6.134)$$

$$S_{22} = \frac{(Z_{11} + Z_c)(Z_{22} - Z_c) - Z_{12} Z_{21}}{\Delta Z} \quad (6.135)$$

$$S_{21} = \frac{2 Z_{21}}{\Delta Z} \quad (6.136)$$

$$S_{12} = \frac{2 Z_{12}}{\Delta Z} \quad (6.137)$$

where $\Delta Z = (Z_{11} + Z_c)(Z_{22} + Z_c) - Z_{12} Z_{21}$.

From (6.122)-(6.125) and Figure 6.51, it can be concluded that two excitation arrangements and four measurements are required for [S] test. When an

incident pulse is applied at the input port, $V_{i_1}(t)$ and $V_{r_1}(t)$ can be measured for one test at the input port and $V_{t_2}(t)$ for another test at the output port. When an incident pulse is applied at the output port, $V_{i_2}(t)$ and $V_{r_2}(t)$ can be measured for one test at the output port and $V_{t_1}(t)$ for another test at the input port. Note that $V_{i_1}(t)$ and $V_{r_1}(t)$ can be measured in one test in E-O sampling; so can $V_{i_2}(t)$ and $V_{r_2}(t)$. This is the basic approach of [S] measurements.

6.2.2 Time window method

One of the major issues of [S] measurements in the above arrangement is to differentiate between the incident and reflected waves propagating in opposite directions. The identification process is commonly carried out with the help of a sampling at a single sampling position along a uniform transmission line that connects the device being tested to the signal generator. The overall length of the line is determined by what is required to locate the sampling position (*i.e.* reference plane) far enough from both the device being tested and the generator so that incident and reflected waves appear fully separated in time at the reference plane and therefore can be uniquely identified. This technique may be called the time window method by which the incident and reflected signals are separated in time if sampled at a single position.

Assuming that the incident pulse duration is t_{in} and the reflected pulse duration t_{ref}, the respective distances L_{ref} and L_{sig} from the probe sampling position to the device being tested and to the signal source should be determined

by (6.138) and (6.139). Referring to Figure 6.51, it can be seen that (6.138) and (6.139) ensure the minimum length of the transmission lines on both input and output ports so that the front wave of reflected signals arrives at reference planes after the end wave of incident signals passes.

$$L_{ref} \geq \frac{vt_{in}}{2} \quad (6.138)$$

$$L_{sig} \geq \frac{vt_{ref}}{2} \quad (6.139)$$

where v is the speed of electric field wave on the transmission line, which is

$$v = \frac{c}{\sqrt{\epsilon_{eff}}} \quad (6.140)$$

where c is the speed of light in free space and ϵ_{eff} the effective dielectric constant of the transmission line, typically ϵ_{eff} is a fraction of the material dielectric constant ϵ [19].

It is implicitly assumed in the time window method that individual signals, the incident and reflected waves in this case, constitute transients of limited duration. However, this may not be necessarily true especially when the signal source, a photo-conductive switch, is fabricated on a GaAs substrate whose carrier lifetime is in the order of 30 ps or longer [?]. In fact, the carrier lifetime of the substrate combined with the low frequency dispersion, attenuation effects, and the reflections from the the bottom of the substrate results in a trailing tail in both incident and reflected signals [8, 9, 16]. This trailing tail in the time domain may be as long as tens or even hundreds of picoseconds. From (6.138) and (6.139), it can

be seen that the transmission line required to separate the incident and reflected signals can be prohibitively lengthy. As a result, the responses of both incident and reflected pulses may be overlapped in the time domain. In order to solve this problem caused by the long trailing tail, a Gaussian pulse [16] is used to fit the incident pulse. This implies elimination of the trailing tail of the incident pulse. In other words, the trailing tail is artificially subtracted out from the measured data before data processing [8]. In this treatment, based on the priori-knowledge about the transmission line, pulses and the device being tested, some care should be taken to keep significant information while the trailing tail is eliminated.

6.3 [S] measurements in the frequency domain

S-parameters can also be measured directly in the frequency domain in electro-optic sampling when the sinusoidal electrical excitation setup is adopted (Refer to Chapter 2.2.2). In this case, the external probe in the E-O sampling system functions exactly the same way as the probe in slotted line used in the conventional technique of VSWR or/and S-parameters measurement. In both measurement techniques, the same approach is taken in the test of voltage standing wave ratio. In other words, measuring the voltage as a function of position with the optical probe permits calculation of the incident and reflected waves on the transmission lines connected to the device being tested. The network S-parameters can then be determined by the measured voltages as function of the positions. However, there are some particular problems involved in the electro-optic sampling, which

are absent in the conventional slotted line technique and will be addressed in the following sections.

6.3.1 Voltage standing wave ratio measurement

Principle

The conventional measurement method of voltage standing wave ratio is based on the assumption of a lossless transmission line. This method will be briefly reviewed in this section and further modified for lossy transmission line.

Figure 6.52 shows a lossless transmission line terminated in an arbitrary load impedance Z_L. In principle, the voltage as a function of the position along the transmission line and the distance of the first minimum voltage from the load can be measured and used to determine the load impedance Z_L [23].

Assume that an incident wave $V_{in}e^{-j\beta z}$ is generated from a source at $z < 0$. A reflected wave $V_{ref}e^{j\beta z}$ is generated due to the load Z_L. The total voltage due to the sum of the incident and reflected waves on the transmission line is

$$V(z) = V_{in}e^{-j\beta z} + V_{ref}e^{j\beta z} \tag{6.141}$$

where $\beta=\frac{2\pi}{\lambda}$ is the propagation constant, and z is the position along the transmission line or propagation direction.

The total voltage and current at the load Z_L are related [23] by the load

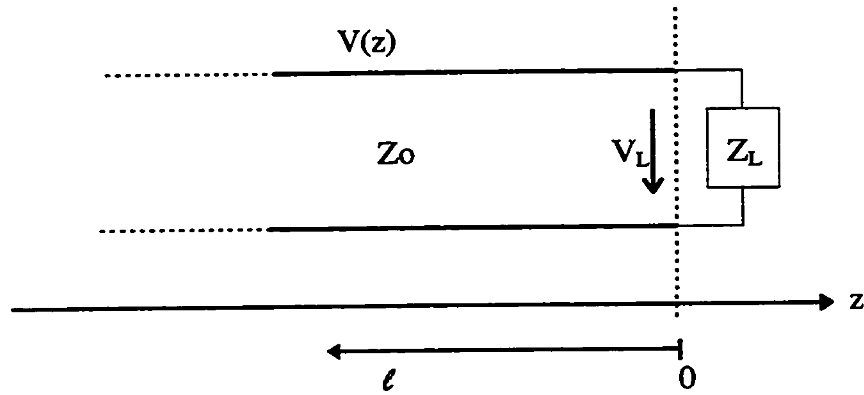

Figure 6.52: A transmission line terminated in a load impedance Z_L

impedance as

$$Z_L = \frac{V_{in} + V_{ref}}{V_{in} - V_{ref}} Z_0 \tag{6.142}$$

where Z_0 is the characteristic impedance of the transmission line.

The amplitude of the reflected voltage wave normalized to the amplitude of the incident voltage wave is known as the voltage reflection coefficient Γ:

$$\Gamma = \frac{V_{ref}}{V_{in}} \tag{6.143}$$

The total voltage on the line in (6.141) can then be written as

$$V(z) = V_{in}(e^{-j\beta z} + \Gamma e^{j\beta z}) \tag{6.144}$$

Thus from (6.144), it can be found that

$$|V(z)| = |V_{in}||1 + |\Gamma|e^{j(\theta - 2\beta\ell)}| \tag{6.145}$$

where ℓ=-z is the positive distance from the load at z=0, and θ is the phase of the reflection coefficient, *i.e.*

$$\Gamma = |\Gamma|e^{\theta} \tag{6.146}$$

It can be seen from (6.145) that the voltage magnitude varies with position $z = -\ell$ along the line. The maximum value V_{max} occurs when the phase term

$$e^{j(\theta - 2\beta\ell)} = 1 \tag{6.147}$$

and

$$|V_{max}| = |V_{in}|(1 + |\Gamma|) \tag{6.148}$$

The minimum value V_{min} occurs when the phase term

$$e^{j(\theta - 2\beta\ell)} = -1 \tag{6.149}$$

and

$$|V_{min}| = |V_{in}|(1 - |\Gamma|) \tag{6.150}$$

Therefore, as a measure of the mismatch of a line, the voltage standing wave ratio (VSWR) can be defined and calculated as

$$VSWR = \frac{V_{max}}{V_{min}} = \frac{1 + |\Gamma|}{1 - |\Gamma|} \tag{6.151}$$

Immediately, it can be shown that

$$|\Gamma| = \frac{VSWR - 1}{VSWR + 1} \tag{6.152}$$

Therefore, the magnitude of the reflection coefficient on the line can be experimentally found from the VSWR by (6.152). To find the phase angle θ in (6.146), it is necessary to know the propagation constant β and the distance between the load and the position of the first voltage minimum.

From (6.145), it can be seen that the distance ℓ_{m_m} between two successive voltage maxima or minima is

$$\ell_{m_m} = \frac{2\pi}{2\beta} = \frac{\lambda}{2} \tag{6.153}$$

where λ is the wavelength on the transmission line. This suggests that both the

propagation constant β and the effective dielectric constant ϵ_{eff} can be found by measuring the distance between two successive minima or maxima along the transmission line since

$$\lambda = \frac{\lambda_0}{\sqrt{\epsilon_{eff}}} \tag{6.154}$$

$$\beta = \frac{2\pi}{\lambda} \tag{6.155}$$

where λ_0 is the wavelength in free space.

In above measurement, the distance ℓ_{m_m} between successive minima or maxima has been found. In addition, the distance ℓ between any sampling position and impedance load position can also be measured. Assuming ℓ_{min} is the distance of the first voltage minimum from the impedance load, it may be found by

$$\ell_{min} = \ell - FIX_{int}\left(\frac{\ell}{\ell_{m_m}}\right)\ell_{m_m} \tag{6.156}$$

where $\text{FIX}_{int}(\text{X})$ rounds the elements of X to the nearest integers towards zero.

Now the phase angle of the reflection coefficient Γ can be readily determined by (6.149), (6.155) and (6.156) as

$$\theta = \pi + 2\beta\ell_{min} \tag{6.157}$$

Refering to (6.146), it can be seen that the propagation constant Γ is fully

determined by (6.152)–(6.157). Then two parameters VSWR and ℓ_{min} can be used to find the load impedance Z_L from Γ:

$$Z_L = Z_0 \frac{1+\Gamma}{1-\Gamma} \tag{6.158}$$

In addition, given the propagation constant β by (6.155), V_{in} and V_{ref} may be calculated from (6.141) by measuring the total voltage at two or more different positions along the transmission line.

Lossy transmission line

As demonstrated in the above derivations, the complex impedance load Z_L can be determined in principle by the measurement of a standing wave at two separate points along the transmission line for a given propagation constant β. In practice, the voltage as a function of the position is measured by sampling the field along a section of the transmission line. V_{in} and V_{ref} in (6.141) may be then extracted using an optimization algorithm to fit the equation (6.141) or, in other words, to match the measured data. When this approach is adopted, the propagation constant β can either be measured by the same approach to be introduced in the last section or considered as another variable and extracted together with V_{in} and V_{ref} in (6.141).

This optimization method is more efficient when the loss of the transmission line is taken into consideration. In this case, the propagation constant β is

substituted by the complex propagation constant γ

$$\gamma = \alpha + j\beta \tag{6.159}$$

where α stands for attenuation on the line. Accordingly, the equation (6.141) becomes

$$V(z) = V_{in} e^{-(\alpha+j\beta)z} + V_{ref} e^{(\alpha+j\beta)z} \tag{6.160}$$

where V(z) is the sampled signal, representing the field or voltage, along the transmission line. V_{in} and V_{ref} are corresponding respectively to the incident and reflected waves.

The optimization method can be applied to fit the measured V(z) to equation (6.160) and hence to find solutions for V_{in} and V_{ref}, α and β. The transmission line is then characterized using these parameters. The load impedance Z_L at z=0 can also be derived from (6.160) by following the same approach derived in the early part of this section.

S-parameter measurements

For a one-port transmission line, the voltage reflection coefficient Γ, or S_{11}, is simply the ratio of the reflected and incident voltages V_{in} and V_{ref} at the specified reference plane.

$$\Gamma = S_{11} = \frac{V_{ref}}{V_{in}} \tag{6.161}$$

Obviously given the (6.141) or (6.160) in case of lossy line, the V_{ref} and V_{in} at the specified reference plane can be found accordingly.

Two-port S-parameters may be measured by determining the incident and reflected wave V_{ref} and V_{in} on sections of transmission line connected to the input and output of the test circuit. The reflection coefficients S_{11} and S_{22} are easily characterized by the same approach used in one-port test. For the measurement of transmission parameters, the voltage as a function of the position is measured at port 2 when the electrical excitation signal is applied at port 1 for S_{21}; same measurement is made at port 1 when excited at port 2 for S_{12}.

Again given the voltage as a function of the position (6.141) or (6.160) at port 1 and port 2 associated with the excitation at port 1 and port 2 respectively, the incident, reflected and transmitted waves at the input and output reference planes can be determined from (6.141) or (6.160). Thus the two-port S-parameters are readily determined by (6.122)-(6.125).

Note that the obtained S-parameters are normalized to the characteristic impedance of the transmission line along which the test is made, and the input and output reference planes are defined. When the required characteristic impedance is different from that of the transmission line, the transform can be straightforwardly made through (6.126)-(6.137).

In conclusion, electro-optic sampling provides an efficient means to virtually avoid complex de-embedding of test fixtures required by conventional network analyzers. Furthermore, it results in a relatively simple treatment in the design of test fixture or test circuit which otherwise requires special care to minimize the impact of numerous discontinuities. However, the procedure of measuring [S] parameters in the frequency domain using the sinusoidal electrical excitation is relatively complicated due to the fact that the measurement should be conducted for each single frequency of interest.

Measurement procedure

S-parameters at a given frequency are measured as follows.

1. A drive signal is applied to the input port.

2. The probe is scanned along a section of the transmission line connected with the device being tested at the input port for V_{in} and V_{ref}, and along that at output port for V_t if it is two-port measurement.

3. The voltage as a function of the position is measured through scanning. Note that whenever the probe is moved in relation to the device and other optics, the scaling factor should be tested using a standard known signal and recorded for post data processing.

4. At both port 1 and port 2, find β, V_{in} and V_{ref} in (6.141). In case of lossy line, α in (6.160) should be added. Either the analytical approach in (6.141)-(6.157) or the optimization fitting technique can be used for the parameters extraction.

5. V_{in_1} and V_{ref_1} as well as V_{t_1} in the case of two-port measurement at input and output reference planes are calculated from (6.141) or (6.160).

6. S_{11} and S_{21} are derived from (6.134) and (6.136).

7. In the case of two-port measurement, the above procedure is repeated except when the drive signal is applied at the output port.

8. V_{in_2} and V_{ref_2} as well as V_{t_2} can be obtained in a similar fashion from (6.141) or (6.160). Hence, S_{22} and S_{12} are derived from (6.135) and (6.137).

Number of sampling points and length of the transmission line

For the analytical approach based on (6.141)-(6.157), only two independent measurements are needed when β is given. If β is not readily available, the field should be sampled along at least a section of half wavelength transmission line to find the ℓ_{min}. When the optimization fitting technique is used for parameters extraction, as few as three or four measurements are enough in principle to extract parameters. However, more measurements over about $\frac{\lambda}{8}$ length of transmission line are recommended to ensure a unique and reliable voltage measurement.

6.4 Waveform calibration of external E-O sampling

In previous sections, techniques of the S-parameter measurements in the time domain and the frequency domain have been discussed generally. However, the distortion primarily determined by the probe thickness and probing dielectric discontinuities may introduce a significant error in measurement results, especially in sub-picosecond range (See Chapter 5). This section discusses how to de-embed the distortion based on the probe transfer function defined in Chapter 5.

6.4.1 Discussion of the probe transfer function

As defined in Chapter 5, the probe transfer function H(ω) is the ratio of frequency transform of the retardance Γ(t) imposed on the sampling beam over frequency transform of the electric field E_{cpw}(t) under the sampling spot on the transmission line being tested. It may be denoted as

$$H(\omega) = \frac{\mathcal{F}[\Gamma(t)]}{\mathcal{F}[E_{cpw}(t)]} \tag{6.162}$$

where the radian frequency $\omega = 2\pi f$. Probe transfer function is artificially defined for probe characterization and calculated according to the numerical experiment results. It can be used based on the following facts.

1. **Retardance** Γ is a measure of the electro-optic response as a function of the electric field in the probe. It can be directly related to the field or voltage in

the device being tested and detected through a beam-splitter and a pair of the photo detectors which convert the retardance to the voltage output. Since the electro-optic response is extremely small ($\Gamma \ll 1$) in most application situations and the probing beam is biased optically for maximum sensitivity and linearity, it can be assumed that signal output voltage from the photo detectors is linearly proportional to the retardance Γ by a ratio of the photo diodes' efficiency.

2. **Electric field E_{cpw}** under the sampling spot on the transmission line with no probe above the CPW is chosen as the input of the probe transfer function. As a matter of fact, retardance of the sampling beam is attributed to electric fields throughout the probing area rather than the field at a single point. That is why group delay of the probe transfer function could be a slightly negative value in some situations. However, E_{cpw} is reasonably defined as a reference to characterize the probe transfer function in any case.

6.4.2 Waveform calibration

One of the important applications of the probe transfer function is to correct the waveform distortion in electro-optic sampling. As mentioned previously, the waveform sampled could be distorted from the waveform in the device being tested, especially when circuit or device speed is in sub-picosecond domain or terahertz range.

As discussed in previous chapters, invasiveness and distortion are the two major causes responsible for discrepancies between the signal to be measured and the sampled signal. The probe transfer function is defined and evaluated in such a way that it can be directly used for de-embedding the probing invasiveness and distortion from sampled signal based on the full wave field modeling and the electro-optic response calculations in the vicinity of and inside the probe.

First, the probe transfer function can be found through a numerical field measurement (See Chapter 5). It is primarily determined by the probe thickness and dielectric electro-optic material. The probing invasiveness and distortion associated with sampled signal are then de-embedded to find the electric field on the transmission line by means of the probe transfer function. It can be formulized as:

$$\mathcal{F}[E_{cpw}(t)] = \frac{\mathcal{F}[\Gamma(t)]}{H(\omega)} \tag{6.163}$$

As mentioned previously, the retardance Γ(t) is linearly proportional to the signal voltage output from the photo diodes. In addition, the probe transfer function H(ω) is a normalized ratio of the probing beam retardance Γ(t) over the electric field E_{cpw} in the device being tested. E_{cpw}(t) found by (6.163) is, therefore, a function in a relative unit associated with the normalized probe transfer function H(ω). This is the basic principle of the waveform calibration using the proposed de-embedding technique.

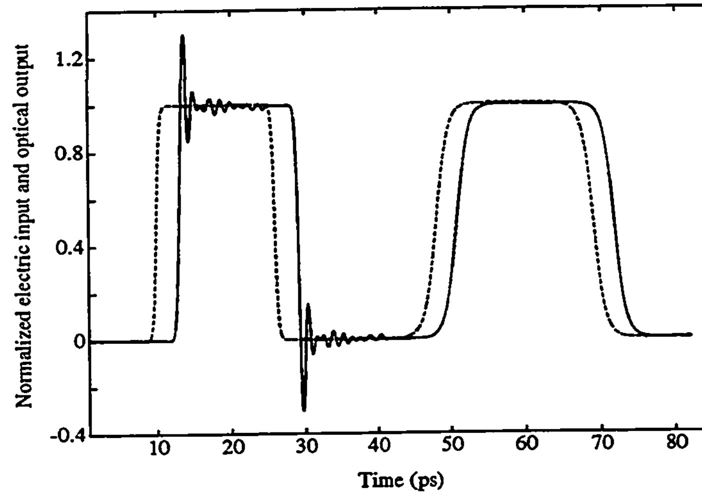

Figure 6.53: Comparison of a square wave signal propagating on the CPW and its E-O sampling output response. Solid line: E-O sampling output; Dashed line: electric input signal to the CPW. The E-O sampling output shows ringing tails at rising and falling edges of the first square while it exhibits distortion-less response to the second square. This is due to the fact that the first square of the input has relatively large frequency components beyond 200GHz, where the frequency response of the probe changes quickly. A time delay in the optical output relative to the electric input is also observed.

To demonstrate waveform calibration by means of the probe transfer function, a square wave signal is applied to the CPW. The corresponding optical output can be predicted using the probe transfer function. Both the input square wave signal and the corresponding sampling output signal, *i.e.* the retardance in electro-optic sampling, are shown in Figure 6.53. The E-O sampling output shows ringing tails at rising and falling edges of the response of the first square while it exhibits a distortion-less response to the second square. This is attributed to the fact that the frequency bandwidth of the second square in the electric input is limited to about 100GHz, which is well within the flat characteristic region of the probe.

As far as calibration is concerned, a simulation has been made for verifying the proposed calibration technique. It is known that the electric field in the device being tested is the response to be determined by the measured optical output. With respect to the E-O sampling system, it can be treated as an input of the system while the optical response of the sampling beam is the output of the system. In the simulation, a known 1.0 ps Gaussian pulse is launched down to the CPW. The optical output in the external E-O sampling is found in the FD-TD field simulation incorporated with E-O effect calculation. Using the obtained probe transfer function, the electric field on the CPW can be then determined by (6.163).

Figure 6.4.2 shows an FD-TD simulated electric field under the sampling spot, which is the field response to the input signal that is a 1.0 ps Gaussian pulse. It also shows the corresponding sampling signal output, which is found in the E-O response calculation using electro-optic tensor, and the de-embeded electric field on

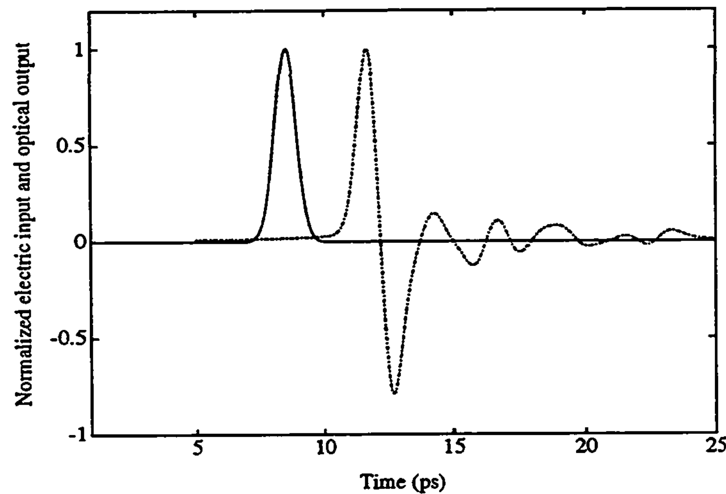

Figure 6.54: Comparison between the electric input obtained by the proposed calibration technique and the actual electric input. The optical output obtained by field and E-O effect simulation is also shown in this figure. Solid line: calculated electric input; Dashed line: the actual electric input; Dashdot line: the corresponding uncorrected E-O system output. Solid line and dashed line almost coincide with each other. It shows excellent agreement between the calculated and the actual input signals. The ringing in the optical output is the sampling distortion to high frequency components.

the CPW calculated by the proposed calibration method. The excellent agreement of the response on the CPW between original field and de-embedded one confirms the validity of the calibration method.

The waveform calibration is necessary when the signal is in the terahertz frequency range or picosecond domain. Decision can be made according to the user's requirements based on the probe transfer function which indicates the linear response limit of the probe. It has been demonstrated that probing distortion can be easily de-embeded. Incorporated with the technique to determine the scaling factor and research results of invasiveness, a field-based calibration technique is developed to de-embed probing invasiveness or perturbation to the operation of the device being tested.

6.5 Calibration of S-parameter measurements

With fundamental studies on invasiveness and distortion by means of the full wave field modeling, the probing distortion has been corrected through the probe transfer function. A field-based calibration technique can be directly derived from the field modeling results which quantitatively evaluate the probe invasiveness in the electro-optic sampling.

Previously, techniques of S-parameter measurements have been reviewed in both time sampling mode (*i.e.* optical excitation) and synchronous sampling mode (*i.e.* electrical excitation). In this section, the measured S-parameters using these

techniques are assumed to be calibrated for de-embedding invasiveness.

6.5.1 Calibration of the reflection coefficient

It is understood that the reflected wave V_{ref} is attributed by the reflections from the device being tested as well as less significant reflections due to the probing effects. Figure 6.55 shows the vector voltage combination of the reflected wave from the device being tested $\vec{V}_{ref_dev}$ and the reflected wave from the probe $\vec{V}_{ref_prb}$ as well as the superposition result $\vec{V}_{ref_m}$ which is the measured value previously used in the S-parameters calculation.

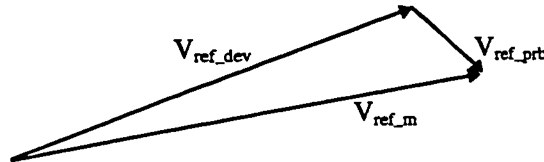

Figure 6.55: reflected waves combinations

Since S-parameters are defined in the frequency domain, the calibration technique is accordingly introduced to process the frequency domain parameters although it is derived from the field modeling results in the time domain.

Refering to Figure 6.55, assume the measured reflection coefficient is Γ_m and the reflection coefficient of the device being tested Γ. Both are complex values, representing vectors. Thus,

$$\begin{aligned}\Gamma_m &= \frac{\vec{V}_{ref_dev} + \vec{V}_{ref_prb}}{\vec{V}_{in}} \\ &= \Gamma + \frac{\vec{V}_{ref_prb}}{\vec{V}_{in}}\end{aligned} \tag{6.164}$$

where $\vec{V}_{in}$ is the vector voltage of the incident wave. In fact, the second term $\frac{\vec{V}_{ref_prb}}{\vec{V}_{in}}$ is the reflection coefficient, noted as a complex value Γ_{prb} thereafter, due to the probe itself. It has been found from the field modeling results in Chapter 4, where it is used to characterize the probing invasiveness. Therefore, the reflection coefficient Γ can be obtained from (6.164) as

$$\Gamma = \Gamma_m - \Gamma_{prb} \tag{6.165}$$

In measurement calibration, Γ can be either S_{11} or S_{22} as well as other reflection coefficients. Refering to Figure 4.25 and Figure 4.26 in Chapter 4, it suggests that when the probe distance is just about 1 μm, the probe reflection coefficient Γ_{prb} is less than -20 dB, which is usually negligible as compared to the reflection coefficient Γ of most devices being tested. If this is the case,

$$\Gamma \approx \Gamma_m \tag{6.166}$$

The error introduced in Γ by this approximation is determined by the magnitude and phase angle of the Γ_{prb}. The following paragraph presents results of the worse-case studies. It can be seen from Figure 6.55 that the worse case for

magnitude occurs when the phases of Γ and Γ_{prb} are either in or out of phase. The corresponding magnitude relative error $\delta(|\Gamma|)$ is

$$\delta(|\Gamma|) = \frac{|\Gamma_{prb}|}{|\Gamma|} \tag{6.167}$$

Similarly the worse case for phase happens if Γ is perpendicular to Γ_{prb}. The corresponding phase relative error $\delta(< \Gamma)$ is

$$\delta(\angle\Gamma) = \frac{\arctan(\frac{|\Gamma_{prb}|}{|\Gamma|})}{\angle\Gamma} \tag{6.168}$$

Error estimation can then be evaluated by (6.167) and (6.168) where Γ_{prb} is derived from full wave field modeling results and Γ is the reflection coefficient of the device being tested. In error analysis, Γ_m is usually taken as a good approximation of Γ if it is not available, provided $\Gamma \gg \Gamma_{prb}$.

When the probe is in contact with the device being tested, Γ_{prb} becomes so significant that it cannot be ignored anymore. From Figure 4.25 and Figure 4.26, Γ_{prb} for $LiTaO_3$ probes can be as large as -10 dB for frequencies above 30 GHz. In this situation, the calibration using (6.165) is necessary to ensure accuracy of the measurement.

Note that the reference planes defined for Γ and Γ_m are implicitly ensured to be the same. However, the reference plane defined for Γ_{prb} may not be necessarily the same as the one used for Γ or Γ_m. In the case concerned in this thesis, Γ_{prb} is

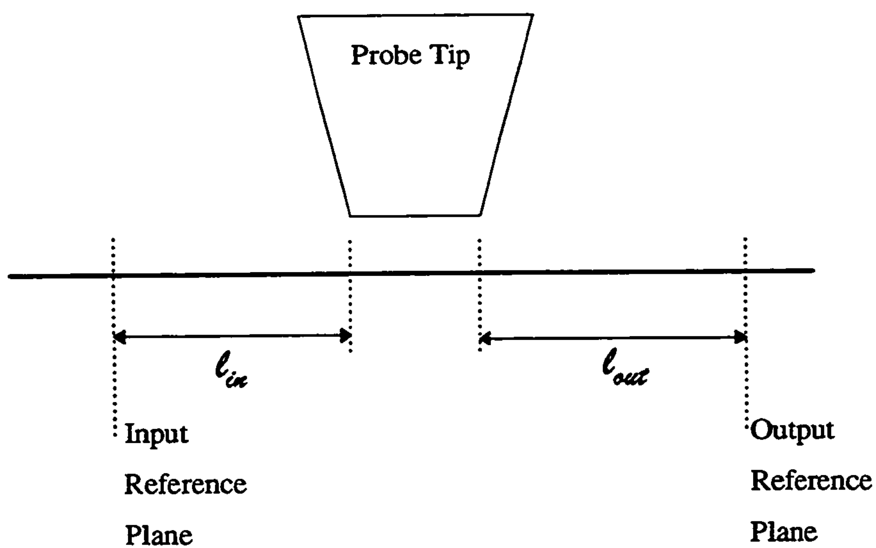

Figure 6.56: Reference planes defined for Γ or Γ_m and Γ_{prb}

calculated at the leading and rear edges of the probe, where Γ_{prb} reference planes are defined by ℓ_{in} and ℓ_{out} as shown in Figure 6.56. ℓ_{in} and ℓ_{out} are the respective distances from the input reference plane to the probe leading edge, and from the output reference plane to the probe rear edge. Both are 275.5 μm in the simulation (Refer to Chapter 2). Generally the reference planes defined for Γ_{prb} are moved to be aligned with the reference planes defined for Γ or Γ_m to keep the reference planes identical for the convenience of the data processing such as the one using (6.165).

As shown in Figure 6.56, the distances between the reference planes associated with Γ and Γ_{prb} are denoted as ℓ_{in} at the input and ℓ_{out} at the output. Thus (6.165) becomes

$$\Gamma = \Gamma_m - \Gamma_{prb} e^{2(\alpha+j\beta)\ell_{io}} \qquad (6.169)$$

where subscript io=in for input port, io=out for output port, α and β can be found using the techniques discussed in previous sections of this chapter. It is implicitly assumed that reference planes defined for Γ_{prb} are always within the reference planes defined for Γ. If not, ℓ_{in} and ℓ_{out} in (6.169) could be negative.

6.5.2 Calibration of the transmission coefficient

The probing effect on the transmission of the CPW has been presented in Chapter 4, where the comparison is conducted between transmission coefficients with and

without the probe. The results provide the transmitted voltage wave without the probe $\vec{V}_t$ (*i.e.* the transmitted voltage wave of the device being tested, which is desired after calibration), the transmitted voltage wave with the probe $\vec{V}_{t_m}$ (*i.e.* the measured transmitted voltage in E-O sampling), and the difference between them $\Delta\vec{V}_t$.

$$\Delta\vec{V}_t = \vec{V}_{t_m} - \vec{V}_t \tag{6.170}$$

$\Delta\vec{V}_t$ is considered as measure of the direct contribution from the probe itself to the measured transmitted voltage wave $\vec{V}_m$. Refering to Figure 6.57 and assuming the incident voltage wave at the excitation port is $\vec{V}_{in}$, the measured transmission coefficient $\vec{T}_m$ is

$$\begin{aligned} \vec{T}_m &= \frac{\vec{V}_m}{\vec{V}_{in}} \\ &= \frac{\vec{V}_t + \Delta\vec{V}_t}{\vec{V}_{in}} \\ &= \vec{T} + \frac{\Delta\vec{V}_t}{\vec{V}_{in}} \\ &= \vec{T} + \Delta\vec{T} \end{aligned} \tag{6.171}$$

where $\vec{T}$ is the desired transmission coefficient of the device being tested, $\Delta\vec{V}_t$ and $\vec{V}_{in}$ or $\Delta\vec{T}$ or $\frac{\Delta\vec{V}_t}{\vec{V}_{in}}$ are available or derivable from the field modeling results in Chapter 4. $\Delta\vec{T}$ is measure of the direct contribution from the probe itself to the measured transmission coefficient $\vec{T}_m$.

In measurement calibration, $\vec{T}$ can be either S_{21} or S_{12} as well as other transmission coefficients. Refering to Figure 4.27 and Figure 4.28 in Chapter 4, it suggests that probing invasive effects on measured transmission coefficient $\vec{T}_m$ are usually negligible (*i.e.* $|\Delta\vec{V}_t| \ll |\vec{V}_{in}|$ or $|\Delta T— \ll |T|)$ as long as the probe is not in contact with the device being tested. Therefore

$$\vec{T} \approx \vec{T}_m \tag{6.172}$$

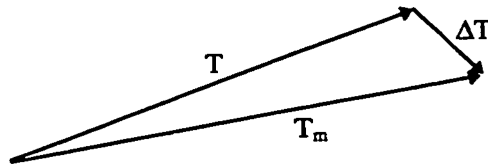

Figure 6.57: Transmission coefficient combination

The error introduced in the transmission coefficient $\vec{T}$ by this approximation is determined by a similar analysis used in reflection coefficient error evaluation. The errors generated in the worst cases are presented in the following. It can be seen from Figure 6.57 that the worst case for magnitude occurs when the phases of $\vec{T}$ and $\Delta\vec{T}$ are either in or out of phase. The corresponding magnitude relative error $\delta(|T|)$ is

$$\delta(|\vec{T}|) = \frac{|\Delta\vec{T}|}{|\vec{T}|} \tag{6.173}$$

Similarly the worst case for phase happens if $\vec{T}$ is perpendicular to $\Delta\vec{T}$. The corresponding phase relative error $\delta(\angle T)$ is

$$\delta(\angle\vec{T}) = \frac{\arctan(\frac{|\Delta\vec{T}|}{|\vec{T}|})}{\angle\vec{T}} \tag{6.174}$$

The error estimation can then be evaluated by (6.173) and (6.174) where $\Delta\vec{T}$ can be obtained from full wave field modeling results, and $\vec{T}$ is the transmission coefficient of the device being tested. In the error analysis, $\vec{T}_m$ is usually taken as a good approximation of $\vec{T}$ if it is not available, provided $|\vec{T}| \gg |\Delta\vec{T}|$ which is usually true (Refer to Chapter 4).

When the probe is in contact with the device being tested, $\Delta\vec{T}$ becomes so significant that it cannot be ignored. Refering to Figure 4.27 and Figure 4.28 in Chapter 4, $|\Delta\vec{T}|$ for $LiTaO_3$ probes can be as large as -1 dB in magnitude and 30° in phase beyond 50 GHz, provided the input and output reference planes are the same as those used for Γ_{prb} calculation (See Figure 6.56). Thus, calibration is necessary in this situation using (6.171).

Again the reference planes defined for $\vec{T}$ and $\vec{T}_m$ are implicitly assumed to be the same. However, the reference plane defined for $\Delta\vec{T}$ may not be necessarily the same as the one used for $\vec{T}$ or $\vec{T}_m$. Following the same approach and the same notations in the previous section on reflection coefficient, the reference planes defined for $\Delta\vec{T}$ are moved to be aligned with the reference planes defined for $\vec{T}$ or $\vec{T}_m$ to keep the reference planes identical for the convenience of the data processing.

Thus (6.171) becomes

$$\vec{T} = \vec{T}_m - \Delta\vec{T}e^{(\alpha+j\beta)(\ell_{in}+\ell_{out})} \tag{6.175}$$

Again it is implicitly assumed that reference planes defined for $\Delta\vec{T}$ are always within the reference planes defined for $\vec{T}$. If not, ℓ_{in} and ℓ_{out} in (6.175) could be negative.

6.6 Conclusions

In this Chapter, a brief review has been given to previous related work on calibration of E-O sampling. Derived from the full wave field modeling results and other research activities, S-parameter measurement procedures have been proposed respectively for both time domain approach (*i.e.* using optical excitation) and frequency domain approach (*i.e.* using synchronous excitation). It is followed by analysis of several technical aspects and criteria regarding the test set up and implementation.

In addition, a temporal waveform calibration technique has been proposed and demonstrated using the probe transfer function. Finally, calibration of the S-parameters measurement has been investigated and a practical approach proposed with the error analysis. The overall work conducted in this Chapter will lead the research and experimental work on E-O sampling further towards quantitative measurement.

Chapter 7

Conclusions

This thesis has contributed to engineering science by applying, for the first time, the full wave time domain field modeling technique (FD-TD method) to the simulation of electro-optic sampling systems. This technique by its nature can be appropriately used to simulate electro-optic sampling system. It enables us to investigate the physics of the system both qualitatively and quantitatively. The results which have been reported in this thesis and the results which will be developed by other researchers for their specific needs on the same platform will provide necessary information for engineers to properly design probes and system set-up in order to achieve optimized electro-optic sampling solutions.

On the full wave time domain field simulation platform built up for this research, many important issues on electro-optic sampling, such as invasiveness, distortion, sensitivity, probing efficiency, calibration and measurement error analysis, have been investigated and evaluated in a systematic way. This platform is

possibly the most efficient analytical tool for electro-optic sampling studies since the early eighties even though research efforts in this field have become more and more active.

This thesis together with other related papers published by the author and the research group in McMaster University has unveiled, for the first time, many insights of the external electro-optic sampling system.

This thesis has examined the invasiveness of the external electro-optic sampling system quantitatively. Previously the invasiveness has been widely assumed to be negligible for the sampling systems or studied under the static field conditions. In this thesis, however, it has been investigated systematically first in time domain as it is seen by sampling systems. Then results are interpreted in the frequency domain as they are usually presented. It has been shown that external probes do not exhibit significant invasiveness up to 100GHz if they are removed from contact by a finite distance, *e.g.* $> 2\mu m$ which depends on dimensions of the device being tested. The results also confirm that GaAs probes offer less invasiveness than $LiTaO_3$ probes while the latter provide higher sampling sensitivity. In general, for a given level of invasiveness, $LiTaO_3$ probes are preferred over GaAs because of the transparency of $LiTaO_3$ at shorter wavelengths where higher electro-optic effects will be achieved.

This thesis has suggested the distortion in electro-optic sampling results. Similar qualitative and quantitative analyzes have been made to understand the physics of the distortion and the limitation generated to the sampling systems. For

the widely used $LiTaO_3$ probe tip of 20 μm thickness, a distortion of the measured signal has been predicted beyond 600GHz. This finding has been supported later on by several independent experimental results [62]. As matter of fact, the distortion can only be ignored without much error in measured results when frequency of interests is less than 100GHz. In the thesis, the distortion has been studied from several different aspects. It shows that the distortion is primarily determined by probes' thickness. Again, a compromise should be made between less distortion of the signal and higher sensitivity of the system. In addition to the probe thickness, the research results also suggest other factors which could affect the distortion. They are probe materials, other probe physical dimensions, probing respective positions in relation to probe itself and device being tested.

This thesis has also shown how full wave time domain field simulation results can be incorporated into electro-optic tensor to generate a complete system simulation from the electro-magnetic field in the device being tested to the electro-optic modulation effects in the probe tip. This is the first demonstration that the entire electro-optic sampling system can be simulated on the same platform.

This thesis has proposed field based calibration techniques for waveform measurement in time domain and vector measurement such as S-parameters in frequency domain. The concept of the probe transfer function has been suggested for the first time to de-embed both invasiveness and distortion impact on the measured data. It is developed based on the full wave field and electro-optic effect simulation results, which in turn can improve efficiency of research on electro-optic

sampling probes, such as the operational and frequency limit of any given probe. It has been found that each specific probe has an intrinsic transfer function primarily determined by the probe dimensions and the space between the probe face and the device being tested. Given the probe transfer function, it can be easily determined whether calibration is necessary for either invasiveness or distortion or both under specific signal and measurement conditions.

Again for the widely used $LiTaO_3$ probe tip of 20 μm thickness, there is no need for any distortion calibration up to near 100GHz. For GaAs probe with the same physical dimensions, however, this nearly distortion free frequency band can go up to 800GHz, which corresponds to a picosecond pulse.

The research conducted in this thesis can be straightforwardly extended to direct and hybrid E-O sampling problems. Further research and development will lead this field based calibration technique in electro-optic sampling to more general devices such as MMICs and more complex circuit board.

Based on what has been developed in this thesis, researchers can investigate almost any aspect of electro-optic sampling systems not only experimentally as it has been for years, but also theoretically as it is required for any developed engineering science.

Bibliography

[1] Amnon Yariv and Pochi Yeh. *Optical Waves in Crystals.* John Wiley & Sons, Inc., New York, N.Y. ISBN 0-471-09142-1.

[2] M. Shinagawa and T. Nagatsuma. Electro-optic sampling using an external GaAs probe tip. *Electron. Lett.,* vol.26, pages 1341–1343, Aug. 1990.

[3] M.S. Heutmaker, G.T. Harvey, D.G. Cruickshank, and P.E. Bechtold. Electrooptic sampling of silicon integrated circuits using a GaAs probe tip. In *Digest of 17 Int. Conf. Quantum Electron IQEC 90*, pages 50,52–53, 1990.

[4] D.R. Dykaar, R.F. Kopf, U.D. Keil, E.J. Laskowski, and G.J. Zydzik. Electro-optic sampling using an aluminum gallium arsenide probe. *Appl. Phys. Lett.,* vol.62, pages 1733–1735, Apr. 1993.

[5] J.M. Wiesenfeld. Electro-optic sampling of high-speed devices and integrated circuits. *IBM J. Res. Develop.,* vol.34, pages 141–161, 1990.

[6] K.W. Forsyth. *Analysis of high speed GaAs ICs with electro-optic probes*, volume 795 of *Characterization of very high speed semiconductor devices & integrated circuits*, pages 317–338. SPIE, 1987.

[7] M. Y. Frankel, J. F. Whitaker, G. A. Mourou, and A. Valdmanis. Experimental characterization of external electrooptic probes. *IEEE Microwave & Guided Wave Lett.,* vol.1, pages 60–62, March 1991.

[8] M.Y. Frankel, J.F. Whitaker, G.A. Mourou, and J.A. Valdmanis. Ultrahigh-bandwidth vector network analyzer based on external electro-optic sampling. *Solid-State Electronics,* vol.35.

[9] D. Conn, X. Wu, J. Song, and K. Nickerson. A full wave simulation of disturbances in picosecond signals by electro-optic probing. In *1992 IEEE MTT-S Int. Microwave Symp. Dig.*, pages 665–668, Albuquerque, New Mexico, 1992.

[10] X. Wu, J. Song, K. Nickerson, and D. Conn. Invasiveness of $LiTaO_3$ and GaAs probes in external electro-optic sampling. *IEEE/OSA J. Lightwave Tech.,* vol.11, pages 448–454, Mar. 1993.

[11] X. Wu, D. Conn, J. Song, and K. Nickerson. Calibration of external electro-optic sampling using field simulation and system transfer function analysis. In *1993 IEEE MTT-S Int. Microwave Symp. Dig.*, pages 221–224, Atlanta, Georgia, June 1993.

[12] X. Wu, D. Conn, and K. Nickerson. Signal distortion in $LiTaO_3$ and GaAs electro-optic sampling probes. *Research report*, 1993.

[13] Guo-Chun Liang, Yao-Wu Liu, and Kenneth K.Mei. Full-wave analysis of coplanar waveguide and slotline using the time-domain finite-difference method. *IEEE Trans. Microwave Theory Tech.,* vol.37, pages 1949–1957, Dec. 1989.

[14] O. Hollricher, F. Ruders, and C. Buchal. The dependence of the electro-optic effect on electric field distribution an dlight beam propagation direction. *Journal of Applied Phys.,* vol.76.

[15] David Conn, (Howard) X. Wu, and Minya Zhang. Full wave electromagnetic simulation of electro-optic high-speed probes. *Optical and Quantum Electronics*, 1996. invited paper, to be published.

[16] S.Gupta, J.F.Whitaker, and G.A.Mourou. Subpicosecond pulse propagation on coplanar waveguides: experiment and simulation. *IEEE Microwave and Guided Wave Letters,* vol.1, pages 161–163, Jan. 1991.

[17] Kurt J. Weingarten, Mark J. W. Rodwell, and David M. Bloom. Picosecond optical sampling of GaAs integrated circuits. *IEEE J. of Quantum Electronics,* vol.QE-24, pages 198–220, Feb. 1988.

[18] D.E. Cooper and S.C. Moss. Picosecond optoelectronic measurement of the high-frequency scattering parameters of a GaAs FET. *IEEE J. Quantum Electron.,* vol.QE-22, pages 94–100, Jan. 1986.

[19] X Wu, D. Conn, J. Song, and K. Nickerson. Faster finite-difference time-domain method using moving spatial boundaries. *Electron. Lett.,* vol.28, pages 2229–2231, Nov. 1992.

[20] X. Wu, D. Conn, J. Song, and K. Nickerson. Using adaptive spatial domain with the finite-difference time-domain method. In *IEEE AP Int. Symp., URSI Meeting and EMP Meeting Joint Symposia*, page 49, July, 18-25 1992.

[21] P.R. Smith, D.H. Auston, and W.M. Augustyniak. Measurement of GaAs field-effect transistor electronic impulse response by picosecond optical electronics. *Appl. Phys. Lett.,* vol.39, pages 739–741, Jan. 1981.

[22] M. Shinagawa and T. Nagatsuma. An automated electro-optic probing system for ultra-high-speed IC's. *IEEE Transactions on Instrumentation an Measurement,* vol.43, pages 843–847, Dec. 1994.

[23] David M. Pozar. *Microwave Engineering.* Addison-Wesley Publishing Company, Inc., 1990. ISBN 0-201-50418-9.

[24] J. A. Valdmanis, G. Mourou, and C.W. Gabel. Picosecond electrooptic sampling system. *Appl. Phys. Lett.,* vol.41, pages 211–212, ? 1982.

[25] B.H. Kolner and D.M. Bloom. Electro-optic sampling with picosecond resolution. *Electron. Lett.,* vol.19, pages 574–575, July 1983.

[26] J. A. Valdmanis, G. A. Mourou, and C.W. Gabel. Subpicosecond electrical sampling. *IEEE J. Quantum Electron.,* vol.QE-19, pages 664–667, Apr. 1983.

[27] G. A. Mourou and K. E. Meyer. Subpicosecond electro-optic sampling using coplanar strip transmission lines. *Appl. Phys. Lett.,* vol.45, pages 492–494, Sept. 1984.

[28] J.M. Chwalek and D.R. Dykaar. A mixer based electro-optic sampling system for submillivolt signal detection. *Rev. Scientific Instr.,* vol.61, pages 1273–1276, April 1990.

[29] D. Le Quang, D. Erasme, and B. Huyart. Fabry-Perot enhanced real-time electro-optic probing of MMICs. *Electron. Lett.,* vol.29, pages 498–499, March 1993.

[30] D.E. Cooper. *Picosecond optoelectronics diagnostics of field effect transistors*, volume 21 of *Springer Series in Electrophysics*, page 54. Springer-Verlag, New York, 1985.

[31] J.A. Valdmanis. Eletro-optic measurement techniques for picosecond materials, devices, and integrated circuits. In R.B. Marcus, editor, *Measurement of High-Speed Signals in Solid State Devices*, pages 136–219. Academic, San Diego, CA, 1990.

[32] M. Shinagawa and T. Nagatsuma. A subpicosecond external electro-optic prober using laser diodes. In *Proc. Int. Test Conf.*, pages 1035–1039, Washington DC, 1990.

[33] W. Mertin, C. Roths, F. Taenzler, and E. Kubalek. Probe tip invasiveness at indirect electro-optic sampling of MMIC. In *1993 IEEE MTT-S Int. Microwave Symp. Dig.*, pages 1351–1354, Atlanta, GA, 1993.

[34] M.Y. Frankel, J.F. Whitaker, and G.A. Mourou. Optoelectronic transient characterization of ultrafast devices. *IEEE J. Quantum Electron.,* vol.QE-28, pages 2313–2324, Oct. 1992.

[35] T.Nagatsuma, T.Shibata, E.Sano, and A.Iwata. Subpicosecond sampling using a noncontact electro-optic probe. *J.Appl. Phys.,* vol.66, pages 4001–4009, Nov. 1989.

[36] B. McCartin, K.R. Umashankar, and T.G. Jurgens. Three dimensional finite difference frequency domain scattering computation using the control region approximation. *IEEE Trans. Magnetics,* vol.25, pages 3092–3094, July 1989.

[37] Morgan M. and K.K. Mei. Finite element computation of scattering by inhomogeneous penetrable bodies of revolution. *IEEE Trans. Antennas Propagat.,* vol.AP-36, pages 1096–1105, Aug. 1988.

[38] R.F. Harrington. *Field computation by moment methods.* The Macmillan Company, New York, 1968. ISBN.

[39] W. Gellert, S. Gottald, M.Hellwich, H.Kastner, and H. Kustner, editors. *Concise Encyclopedia of Mathematics.* Van Nostrand Reinhold, New York, second edition edition, 1989. ISBN 0-442-20590-2.

[40] K.S. Yee. Numerical solution of initial boundary value problems involving Maxwell's equations in isotropic media. *IEEE Trans. Antennas Propagat.*, vol.AP-14, pages 302–307, May 1966.

[41] X. Zhang and K.K. Mei. Time domain finite difference approach for the calculation of microstrip open-circuit end effect. *IEEE Trans. Microwave Theory Tech.*, vol.MTT-36, pages 1775–1787, Dec. 1988.

[42] G. Mur. The modeling of singularities in the finite-difference approximation of the time-domain electromagnetic field equations. *IEEE Trans. Microwave Theory Tech.*, vol.29, pages 1073–1077, Oct. 1981.

[43] B. Engquist and A. Majda. Absorbing boundary conditions for the numerical simulation of waves. *Mathematics of Computation*, vol.31, pages 629–651, July 1977.

[44] Svetlana S. Zivanovic, Kane S. Yee, and Kenneth K. Mei. A subgridding method for the time-domain finite-difference method to solve Maxwell's equations. *IEEE Trans. Microwave Theory Tech.*, vol.MTT-39, pages 471–479, March 1991.

[45] C. H. Chan, L. Li, J. T. Elson, and L. Tsang. A conformal finite-difference time-domain approach for monte carlo simulations of random rough surface scattering. In *Digest of URSI Radio Science Meeting*, page 13, Chicago, USA, July 20-24 1992.

[46] David B. Shorthouse and C. J. Railton. The incorporation of static field solutions into the finite difference time domain algorithm. *IEEE Trans. Microwave Theory Tech.,* vol.MTT-40, pages 986–994, May 1992.

[47] C. J. Railton, D. B. Shorthouse, and J. P. McGeehan. Modeling of narrow microstrip lines using finite difference time domain method. *Electron. Lett.,* vol.28, pages 1168–1170, June 1992.

[48] W. Sui, D.A. Christensen, and C.H. Durney. Extending the two-dimensional FDTD method to hybrid electromagnetic systems with active and passive lumped elements. *IEEE Trans. Microwave Theory Tech.,* vol.MTT-40, pages 724–730, Apr. 1992.

[49] Amnon Yariv. *Optical Electronics.* Saunders College Publishing, A Division of Holf, Rinehart and Winston, Inc., fourth edition 1991 edition. ISBN 0-03-047444-2.

[50] J.A. Valdmanis, G. Mourou, and C.W. Gabel. Picosecond electro-optic sampling system. *Appl. Phys. Lett.,* vol.41, pages 211–212, Aug. 1982.

[51] D. M. Sheen, S. M. Ali, M. D. Abouzahra, and J. A. Kong. Application of the three-dimensional finite-difference time-domain method to the analysis of planar microstrip circuits. *IEEE Trans. Microwave Theory Tech.,* vol.MTT-38, pages 849–857, July 1990.

[52] J.A. Valdmanis and S.S. Pei. *A non-contact electro-optic prober for high speed integrated circuits*, pages 4–10. Picosecond electronics and optoelectronics II. Springer-Verlag, New York, 1987.

[53] M.Y. Frankel, S. Gupta, J.A. Valdmanis, and G.A. Mourou. Terahertz attenuation and dispersion characteristics of coplanar transmission lines. *IEEE Trans. Microwave Theory Tech.,* vol.MTT-39, pages 910–915, June 1991.

[54] S.S. Bedair and I. Wolff. Fast, accurate and simple approximate analytic formulas for calculating the parameters of supported coplanar waveguides for (M)MIC's. *IEEE Trans. Microwave Theory Tech.,* vol.MTT-40, pages 41–48, Jan. 1992.

[55] G. Hasnain, A. Dienes, and J.R. Winnery. Dispersion of picosecond pulses in coplanar transmission lines. *IEEE Trans. Microwave Theory Tech.,* vol.MTT-34, pages 738–741, ? 1986.

[56] EESof Inc., Westlake Village, CA 91362. *Touchstone/Libra User's Manual.*

[57] B.H. Kolner and D.M. Bloom. Electrooptic sampling in GaAs integrated circuits. *IEEE J. Quantum Electron.,* vol.QE-22, pages 79–93, Jan. 1986.

[58] B.P. Lathi. *Signals, systems, and controls.* Intext Educational Publishers, 1974. ISBN 0-7002-2431-9.

[59] T. Nagatsuma, M. Yaita, M. Shinagawa, M. Amano, and Y. Shuto. Organic patch sensor for electrooptic measurement of electrical signals in integrated circuits. *Electron. Lett.*, vol.27, pages 932–934, May 1991.

[60] Mitsuru Shinagawa and Tadao Nagatsuma. An automated optical on-wafer probing system for ultra-high-speed ICs. In *1992 Int. Test Conf. Proceedings*, pages 834–839, Baltimore, MD, USA, 1992.

[61] M.S. Heutmaker, G.T. Harvey, T.B. Cook, and J.S. Perino. Measurement of phase and amplitude response of a GaAs MMIC by electro-optic sampling. In *1991 IEEE MTT-S Int. Microwave Symp. Dig.*, pages 1133–1135, Boston, MA, 1991.

[62] O. Hollricher, F. Ruders, and C. Buchal. Generation of guided polaritons in electro-optic $LiTaO_3$ probes. *Journal of Applied Phys.*, vol.77.

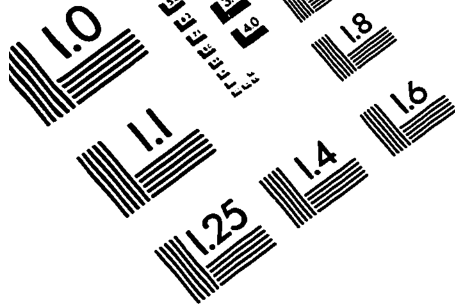

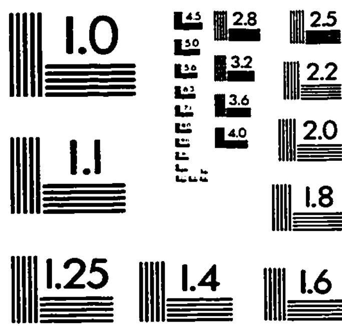

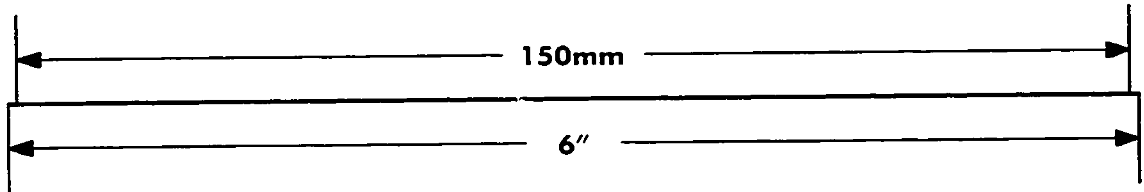

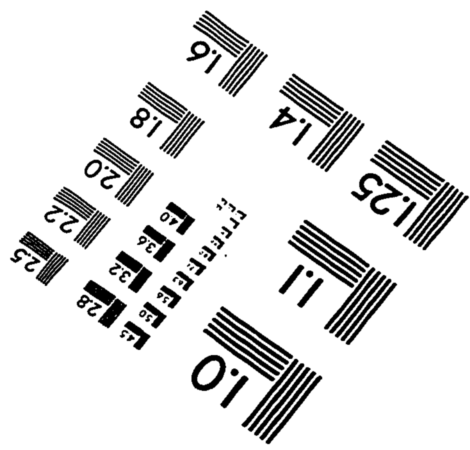

APPLIED IMAGE . Inc
1653 East Main Street
Rochester, NY 14609 USA
Phone: 716/482-0300
Fax: 716/288-5989

© 1993, Applied Image, Inc., All Rights Reserved